POLITECNICO DI TORINO

Master's Degree in Aerospace Engineering

Master's Degree Thesis

Detailed Modeling of Cork-Phenolic Ablators in Preparation to the Post-Flight Analysis of the QARMAN Re-Entry CubeSat

Supervisors
Prof. Domenic D'Ambrosio
Prof. Thierry Magin
Advisors
Dr. Alessandro Turchi
Dr. Pierre Schrooyen

Candidate
Claudio Miccoli

Anno accademico 2019-2020

Alla mia famiglia e a tutti coloro che
continuano a credere in me, ogni giorno.
A chi mi è stato di ispirazione
e a chi lo sarà in futuro.

Abstract

The ever-growing challenges in the field of space flight have been pushing the scientific community to search for innovative solutions. Considering that aerospace applications have a strong impact on several fields, a curious change in trend has recently started. Space, so far inaccessible to most and reserved for government space agencies, is now capturing the attention of industrial companies, accelerating technical progress. The design of high-performance spacecraft, capable of operating in extreme environments, is thereby of primary interest. Among the most challenging tasks, atmospheric entry and thermal protection issues deserve a specific mention in this regard, requiring the development of special heat shields. Ablative materials are largely used to this end. In particular, a class of low-density, charring and cork-based ablators has been recently developed. In fact, the excellent properties of cork make it one of the best solutions available for these purposes.

This master thesis project was carried out at the von Karman Institute (VKI) for Fluid Dynamics, in Belgium, in collaboration with Cenaero. It deals with the analysis of the Cork P50, equipped on the Qarman Re-entry CubeSat developed for ESA at VKI, as a scientific demonstrator for Aerothermodynamic Research. Lifted off to the ISS in December 2019, the re-entry of Qarman is expected for August 2020 and the data collected during its re-entry will then be used for validation purposes. The ability to model and predict the atypical behaviour of the new cork-based materials is considered a critical research topic. Therefore, this work is motivated by the need to develop a numerical model able to respond to this demand, in preparation to the post-flight analysis of Qarman. The study is focused on the main thermal response phenomena of the cork P50: pyrolysis and swelling.

Pyrolysis and more generally ablation were analyzed by means of the multi-physics CFD code Argo, developed at Cenaero. Based on a unified flow-material solver, the Volume Averaged Navier-Stokes equations were numerically solved to describe the interaction between a multi-species high-enthalpy flow and a reactive porous medium, by means of a high-order Discontinuous Galerkin Method. Specifically, an accurate method to compute the pyrolysis production rate was implemented. While the chemical composition of pyrolysis gases has been so far pre-fixed, a routine calling the VKI Mutation++ library was added, in order to compute the composition at equilibrium. A series of simulations was performed, getting good results and highlighting the effect of the elemental composition of pyrolysis gases, that should be estimated experimentally.

The modeling of swelling was the most ambitious task, requiring the development of a physical model accounting for this phenomenon, for the purpose of a future implementation within Argo. A 1D model was proposed, mainly based on an a priori assumption on the swelling velocity and the resolution of a nonlinear convection equation, by means of a Finite Difference Method. Once developed, the model was successfully tested through a Matlab code, showing that the approach is very promising and thus opening the way to further developments.

Acknowledgements

Everyone knows what a master thesis represents, but I would like to explain what this work means to me. It is the very first step to assert myself and take my place in the world. I cannot see the finish line, but I can trust my feelings and passions. Looking back over these years, naturally I cannot help extending my acknowledgements to all the people who contributed in some way, supporting me. First, I would like to express my gratitude to my supervisor Professor Domenic D'Ambrosio, for the consideration he showed to me and his advices in reviewing this work. I am equally grateful to Professor Thierry Magin for giving me the opportunity to carry out this research project at the von Karman Institute and for his precious suggestions in preparing my final defence.

Then, I would also like to thank immensely my advisors Alessandro and Pierre, for teaching, supporting and driving me throughout the entire experience. I really learned a lot and I owe it all to you two. Another special thanks goes to David Henneaux, who was essential for the success of this work and he has always cared about helping and encouraging me. Finally, I want to thank all the people I spent the most time with: Alessandro P., Antonio, Marco, Andrea, Giada, Manuela, Simone, Miguel and my flatmates. We shared dinners, nights, trips and all the time at VKI, so thank you.

But let's step back to... Italy. Questo lavoro rappresenta indubbiamente la fine di un percorso importante. Studiare al Politecnico di Torino è stato stimolante, gratificante e (da non credere) persino massacrante. Ma ciò che conta davvero è che mi ha aiutato a scoprire lati di me che, forse, difficilmente avrei conosciuto. Naturalmente, è stato un viaggio personale ma segnato da incontri con tante persone che meritano la mia riconoscenza. Innanzitutto, sento di dover ringraziare quei professori che sono riusciti a trasmettere la loro passione, valorizzando fortemente la mia esperienza universitaria e rappresentando un'importante fonte d'ispirazione; perciò un sentito grazie va al Prof. D'Ambrosio e al Prof. Iuso che non solo, inconsapevolmente o meno, mi hanno stimolato continuamente durante le loro lezioni, ma hanno dimostrato di credere in me, supportandomi anche nella ricerca di opportunità esterne.

Non posso non pensare poi alle interminabili ore di lezione e di studio condivise con i miei colleghi e amici: Marco, Luca, Nico, Matteo, Mattia e tutti gli altri. Avete reso tutto molto più divertente, ma anche più facile... o almeno ci avete provato! Un forte grazie va anche ai ragazzi del team EoliTO, che per me ha segnato *la* svolta. Ed ora passiamo ai ringraziamenti speciali. La mia permanenza a Torino si conclude (o si interrompe?) qui, ma ho avuto la fortuna di aver trascorso questi anni con alcuni dei miei amici storici. Tutto è iniziato con Paolo e Giulia, con cui ho affrontato i primi ottimi pranzi alla mensa del Politecnico; non è durata tanto e, con il tempo, mentre loro imparavano a cucinare io imparavo a sopravvivere. E che dire di Tony e Francesca? Sempre presenti, o meglio, spiriti infestanti, pronti a turbare i miei weekend a Torino. Altri personaggi degni di nota sono le napoletane, Giovanna e Gloria, con la loro sempre sobria e asfissiante personalità. Come dimenticare poi gli tutti appuntamenti in palestra con Benedetta, Gloria e Cosimo? Facile, saranno stati due o tre... Ovviamente non posso non menzionare anche Luca, Piergiuseppe, Marco, Andrea Manelli, Pasqua e, per concludere in bellezza, Daniele Piscozzo, sempre pronto ad aspettarci in Puglia. Insomma, non il migliore dei gruppi (di certo non per colpa mia), ma pur sempre un gruppo.

Infine, un sentito ringraziamento alla mia famiglia, che mi ha reso una persona migliore: semplicemente mio padre Giancarlo, mia madre Lorena, mio fratello Fabio, mia nonna Elena e mia nonna Pierina, che mi guarda da lassù. Per gli anni passati e per quelli che verranno: *grazie*.

Claudio

Contents

List of Figures

List of Tables

Nomenclature

Acronyms

BDS	Backward Difference Scheme
CDS	Central Difference Scheme
CFD	Computational Fluid Dynamics
CGFEM	Continuous Galerkin Finite Element Method
CMA	Aerotherm Charring Material Thermal Response and Ablation
DGM	Discontinuous Galerkin Method
DOF	Degrees of Freedom
FDM	Finite Difference Method
FDS	Forward Difference Scheme
FEM	Finite Element Method
FIAT	Fully Implicit Ablation and Thermal-response
FVM	Finite Volume Method
ODE	Ordinary Differential Equation
PDE	Partial Differential Equation
REV	Representative Elementary Volume
TGA	Thermogravimetric analysis
TITAN	Two-dimensional Implicit Thermal-response and AblatioN
TPM	Thermal Protection Material
TPS	Thermal Protection System
VKI	von Karman Institute

Chapter 1

Introduction

The 20th century was marked by great achievements in history of space exploration, ever since the earlier aerospace pioneers began to pursue the dream of leaving Earth to discover space. This is the era of the *Space Race*, two words coined to indicate the strong competition between the United States and the Soviet Union to achieve the primacy in the field of spaceflight. The rocket V-2/WAC Corporal was the first man-made object reaching high altitudes and high velocities, more than Mach 5 [1]. It was the 24th February of 1949 and the race for hypersonic vehicles supremacy had just begun.

In 1957, the Soviet satellite Sputnik I was launched in space and, in 1961, the Vostok I allowed the cosmonaut Yuri Gagarin to become the first man to fly in space, to orbit the earth and live, for the first time in the history, the experience of an atmospheric re-entry, at more than Mach 25. This was the stepping stone for manned hypersonic flight, followed by two American missions, the suborbital flight of Alan B. Shepard (Freedom 7) and the propulsive flight of Robert White on the X-15.

The first re-entry capsules were thus developed; Vostok I, Mercury, Gemini and Apollo are words written in history of manned capsule-based spaceflight and all of these missions were driven by the same concept: space exploration depends on the ability to allow humans to reach new horizons, but also to design vehicles capable of bringing them back safely.

1.1 Atmospheric re-entry physics

A spacecraft returning from the Moon and re-entering the Earth's atmosphere is exposed to extreme physical conditions. Considering the future plans of space exploration, this is why the issue of thermal protection in the framework of re-entry Aerothermodynamics is of such great interest. A re-entry capsule is essentially a braking device: it develops a strong aerodynamic drag, transferring its high kinetic energy to the surrounding gases. The blunt shape of a re-entry vehicle is related to the fact that in the high-speed flight a different kind of aerodynamics is involved. This is the *hypersonic aerodynamics* or, in other terms, the regime of hyper-velocity flight.

A hypersonic flow can be defined as a flow regime in which some particular physical phenomena become important. The governing parameter is the Mach number so that,

Figure 1.1: Illustration of the SpaceX's Dragon capsule during the atmospheric re-entry.

generally, the flowfield around a capsule begins to exhibit the characteristics of a high-speed flow when the Mach number becomes greater than 4 or 5. When a blunt body enters the atmosphere of a planet, a strong detached shock wave, a *bow shock*, appears in front of the vehicle. The strong interaction between these two systems leads the viscous dissipation to convert the large kinetic energy lost by the vehicle in internal energy of the surrounding gas [1]. The shock layer is dominated by *high-temperature flows*, so that the gas temperature behind the nearly normal shock wave in the nose region can reach extraordinary values, exciting the internal vibrational energy and causing chemical reactions of dissociation or, at higher temperatures, ionization too. In fact, thermochemical phenomena are related to the excitation of the thermal degrees of freedom. According to quantum mechanics, as the gas temperature is increased, even more energetic molecular collisions will lead to the population of higher energy levels. Considering the air internal energy, air at low temperatures ($T < 1000$ K) has only translational and rotational energies. At about $T = 800$ K, the excitation of vibrational energy leads the specific heats (c_p, c_v and therefore $\gamma = c_p/c_v$) to become function of temperature [1]. For a 5-species air chemistry model, temperatures above 2000 K cause O_2 dissociation and, at higher temperature, N_2 and NO dissociations too:

$$
\begin{aligned}
\mathrm{O_2 + M} &\rightleftharpoons \mathrm{2O + M} \\
\mathrm{N_2 + M} &\rightleftharpoons \mathrm{2N + M} \\
\mathrm{NO + M} &\rightleftharpoons \mathrm{N + O + M}
\end{aligned}
$$

where M is the generic third body. Moreover, the dissociated species can recombine with each others through exchange reactions, such as:

$$
\begin{aligned}
\mathrm{NO + O} &\rightleftharpoons \mathrm{N + O_2} \\
\mathrm{N_2 + O} &\rightleftharpoons \mathrm{N + NO}
\end{aligned}
$$

Finally, for temperatures above 9000 K, the excitation of electronic energy takes place and atomic ionization occurs ($O \rightarrow O^+ + e^-$, $N \rightarrow N^+ + e^-$), so that a (at least) 7-species air chemistry model is required to describe air mixture. Therefore, air becomes a partially ionized plasma [1], that is able to absorb radio-frequency radiation, causing a communication black-out during part of the re-entry phase [2].

During re-entry, each particle moving through the flow field meet continuously different thermodynamic conditions. Hence, if the excitation of vibrational energy and chemical reactions have not enough time to take place, it is not possible to reach the equilibrium conditions and such a flow is a *non-equilibrium flow*. The Damköhler number (Da) is the governing non-dimensional parameter, since it compares the characteristic time of fluid dynamics with the one of thermochemistry: $\mathrm{Da} = 0$ indicates a frozen flow, while if $\mathrm{Da} \rightarrow \infty$ we have an equilibrium flow. Except in one limited region in which it is reasonable to assume the local thermochemical equilibrium, re-entry flows are typically in non-equilibrium conditions, because the shock layer is characterized by chemical reactions not as quick as fluid dynamics. For this reason, they require a more complicated analysis, since the fluid dynamics partial-differential equations must be coupled with other differential equations describing the chemical composition as function of temperature and pressure (as in an equilibrium flow) but also of time.

Another fundamental characteristic of the hypersonic regime is related to the high altitudes in which a re-entry vehicle has to operate. In such an extreme environment, a *low-density flow* is involved. Specifically, the degree of rarefaction of a gas can be described in terms of Knudsen number (Kn) [3]. This governing non-dimensional parameter compares the local *mean free path* to a characteristic dimension of the body, so that three different flow regimes can be identified: at very high altitudes (above 100 km), the gases are extremely rarefied. This is the *free-molecular flow* ($\mathrm{Kn} > 100$) in which, since the molecules are very far apart, the collision probability is very low and only the molecules-surface interaction is not negligible. For $0.01 < \mathrm{Kn} < 100$ a *transitional regime* can be found, in which the molecules-molecules interaction begins to be important. Finally, at lower altitudes ($\mathrm{Kn} < 0.01$) the *continuum regime* can be identified. From a numerical point of view, in the first two regimes the Navier-Stokes equations model is not appropriate to describe the flow, whilst a Direct Simulation Monte Carlo (DSMC) could be required.

In light of the multidisciplinary nature of this field, which involves not only aerodynamics, but also thermodynamics and chemistry, the term *Aerothermochemistry* was coined by Theodore von Kármán in the 1950s to describe the study of hypersonic high-temperature flows [4],[5].

1.1.1 Aerodynamic heating and thermal protection issues

For the reasons described above, it is paramount to thermally protect spacecraft against the high heating loads, by means of appropriate shapes and materials. Heat transfer between hot gases and the surface of a hypersonic vehicle is known as *aerodynamic heating*. This is due to a convective heating, q_C, and a radiative heating, q_R ([1], [6]), as sketched in Figure 1.3.

The *convective heating* is composed of a conduction component and a diffusion one. The former is related to the energy transfer operated by the thermal conductivity (driven

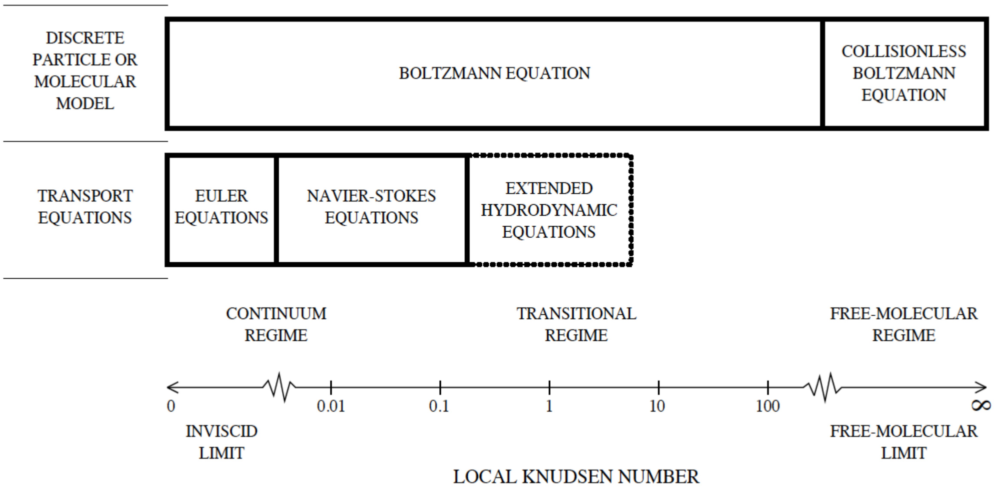

Figure 1.2: Flow regimes during the atmospheric re-entry and applicability of the various equations models (from [3],[7]).

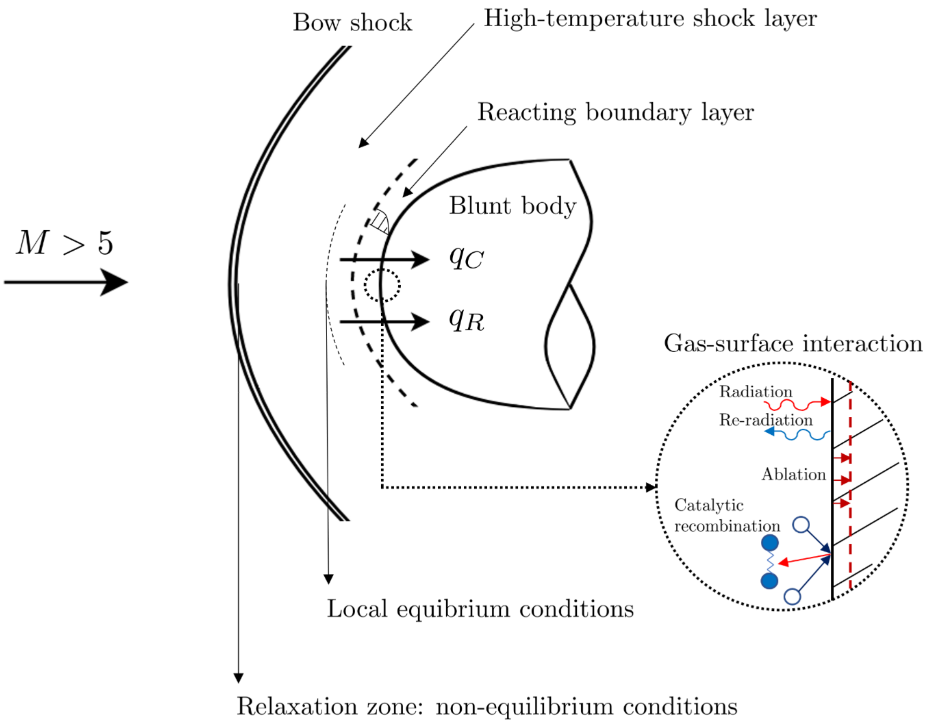

Figure 1.3: Main physical phenomena in a hypersonic high-temperature flow.

by thermal gradients), as in an ordinary non-reacting gas, while the latter is due to atomic recombination [8]: for a hot gas undergoing chemical reactions, energy is transported by diffusion of chemical species too (driven by mass fraction gradients) and, when atoms diffuse near the wall, they recombine through exothermic reactions, so that the atomic heat of formation can increase the surface temperature. The conduction component is proportional to the inverse of the curvature radius of the nose vehicle ($q_w \propto 1/\sqrt{R}$, [1]) and it is for this reason that the atmospheric re-entry requires a blunt shape. Instead, the diffusion component can be decreased by means of a non-catalytic surface, in order to avoid the recombination of the atoms diffusing near the wall. Moreover, the convective heating is also reduced in the presence of surface blowing due to ablation [2].

The *radiative heating* is caused by the impact, on the surface material, of the photons emitted by the hot gas particles ([6],[2]). It is proportional to the shock layer thickness and, as a result, at the stagnation point it is proportional to the nose radius [9]. In particular, if temperature reaches about 10000 K, the radiative heat flux becomes an important heating component, due to ionized gases.

Aerodynamic heating issues are partially solved by using blunt shapes (Figure 1.4), since the heat transfer due to the shock-wave compression and generated outside the boundary layer can be more easily removed than the one due to viscous dissipation arising inside the boundary layer, especially if it is a turbulent boundary layer and the shock wave is detached from the body surface. In fact, unlike an oblique shock wave, the temperature rise related to a bow shock takes place in a region further away from the wall. In other words, aerodynamic heating is lower if a greater fraction of heat is generated by the shock wave and a smaller one is due to the viscous dissipation [10]. However, considering the high temperatures inside the shock layer, the blunt shape cannot be the only means of thermal protection. Instead, the use of an appropriate Thermal Protection Material (TPM) is needed, that is the so called *heat shield*.

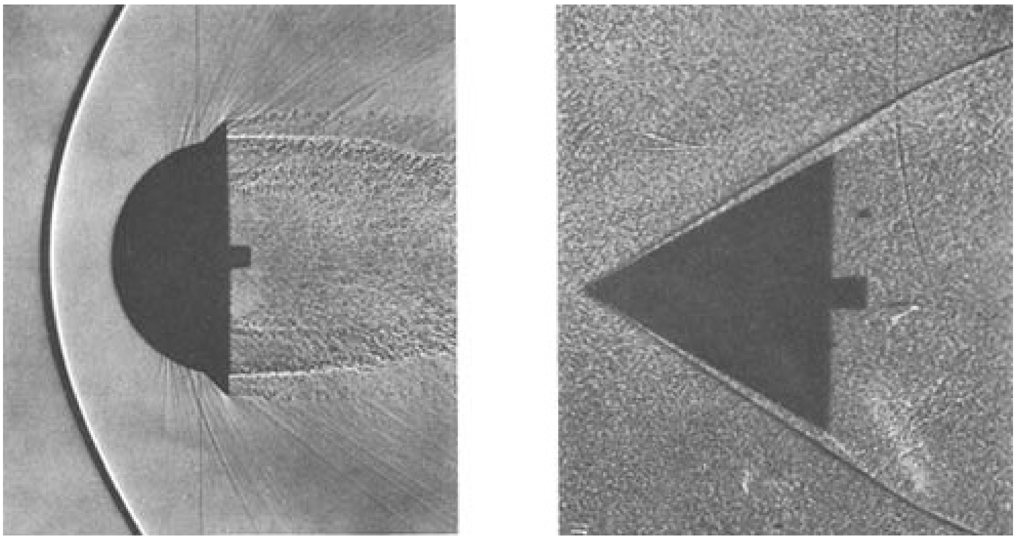

Figure 1.4: Bow shock generated by a blunt body and oblique shock produced by a sharp nose. Credits: [10].

1.2 Thermal protection systems

During planetary re-entry, the severe heat load on the surface material requires the use of a special thermal protection system (TPS), in order to let the flight vehicle to sustain itself in the environment for a given period of time [5]. So far, several types of TPSs have been developed and a classification can be based on their reusability.

Among the *reusable* TPSs, it is possible to distinguish the passive and the active ones. The former are mainly radiative TPSs exploiting both re-radiation to reject high temperatures and low thermal conductivity to prevent heat penetration, and they are also coated to limit catalytic reactions and increase emissivity; they are designed for low heat flux trajectories and a renowned example is the Space Shuttle Orbiter, equipped with a radiative heat shield [11]. The latter make use of active cooling systems such as heat pipes and active transpiration but, due to their complexity, they are rarely used [12]. Although the reusable TPSs are still of great interest, they are not considered in this work.

The *non-reusable* TPSs are typically semi-passive systems which combine re-radiation, ablation and pyrolysis to shield the vehicle. When the reusability criterion is not required, they are largely used since they are able to dissipate high heat fluxes by mass removal [12]. For instance, the Apollo capsule was equipped with a high-density ablative heat shield. However, since a TPS may constitute the $20 \div 30\%$ of the total weight during re-entry [8], the strong mass efficiency requirements led to the development of a new class of low-density and porous ablators [11], such as the *Phenolic Impregnated Carbon Ablator* (PICA), used as TPM for the Stardust or Mars Science Laboratory (MSL) missions and for the SpaceX Dragon capsule [13]. In particular, PICA is classified as a carbon-phenolic material, since it is equipped with carbon fibers providing structural strength and it is impregnated with a phenolic resin that, at high temperatures, pyrolyses producing a gas. Another modern material is the cork-phenolic TPM, such as the Amorim's P50, successfully used for the Intermediate Experimental Vehicle (IXV) project and for the QARMAN CubeSat. The cork-based materials can count on the properties of cork, such as its elasticity, flexibility, compressibility and low conductivity, as well as on the percolation of the gas enclosed in its cells [14].

Both PICA and P50 belong to a special class of ablative heat shields, the so-called *charring ablators*, which are the object of study in this work. Specifically, the interaction between the hot gases and the material will be investigated and, due to the complexity of the phenomenology at the interface between these two regions, a deeper explanation is needed.

1.2.1 Gas-surface interaction

When the surface of a hypersonic vehicle meets the thermo-chemically reacting gas within the shock layer, convection and radiation of this high-enthalpy flow can heat the surface material up to 3000 K in the most severe cases, as shown in Figure 1.5. Hence, the idea behind the design of a TPS is to give rise to physical-chemical phenomena capable of absorbing part of the heat. In space physics, the energy absorption by removal of material is known as *ablation* [12]. Therefore, an ablative TPS can be defined as a material able to undergo a degradation, in order to dissipate part of the thermal energy and preserve the structural integrity. Moreover, ablation products increase the thickness of the boundary layer, limiting the convective heat flux at the surface material and changing the velocity profile [8].

Ablation is mainly characterized by chemical reactions (oxidation, nitridation) and phase changes (melting, vaporization, sublimation). The former are typically heterogeneous reactions occurring when the hot material reacts with oxygen and nitrogen from the air. These reactions must be carefully considered, as they have an exothermic nature, so they add energy. For instance, oxidation lets the surface of a carbon-based material to be attacked by oxygen, so that the production of a gas (CO or CO_2) is accompanied by heat release. Similarly, nitridation involves the production of CN. On the contrary, phase changes are endothermic processes, therefore they have a positive cooling effect since they can absorb a large amount of energy [12]. The removal of solid mass may also be caused by aerodynamic shear stresses [16]; this ablation mechanism, due to the thermomechanical erosion of the surface material, is known as spallation and, since it causes a mass loss involving a minimal energy absorption, it is an undesirable phenomenon which may lead to a thermostructural failure [12]. Moreover, the mass removal operated by spallation may be not uniform, so that an irregular surface may be produced, locally characterized by a high curvature radius and this, in turn, may contribute to accelerate the local mass removal.

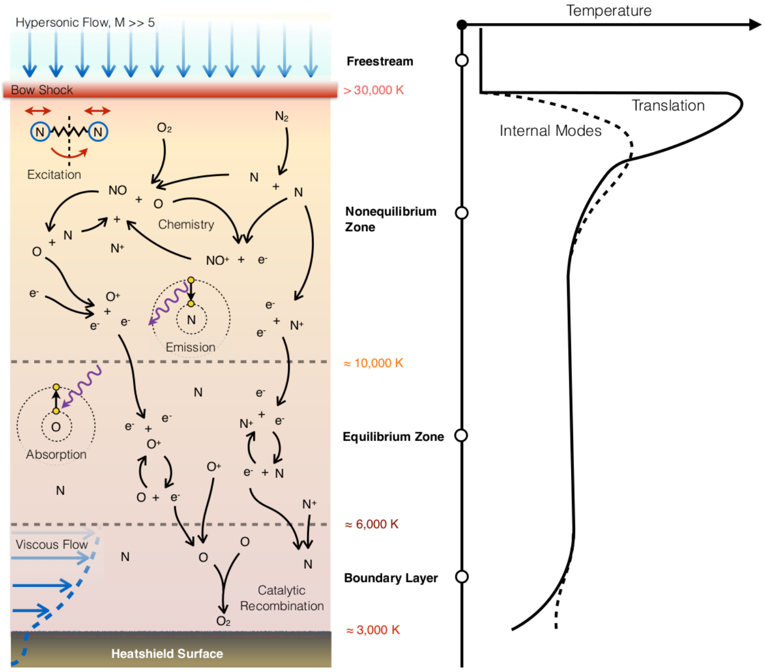

Figure 1.5: Evolution of the flow field between the bow shock and the material surface. Credits: [15].

A special consideration should be done for charring ablators, which are able to pyrolyse undergoing a thermochemical decomposition reaction. Pyrolysis is a thermal process capable of degrading the material and generating volatile compounds. It occurs when organic matter is heated above its decomposition temperature, in a low-oxygen atmosphere. A schematic description of a carbon-phenolic material response is illustrated in Figure 1.6, while Figure 1.7 shows the thermal decomposition of PICA through Scanning Electron Microscope (SEM) images. During heating, when the virgin material reaches a high enough temperature (about 400 K), the resin begins to thermally decompose by means of endothermic reactions, giving rise to the production of the pyrolysis gases. While temperature is increased, pressure rises too causing the percolation of the gases: they slowly move through the pore network of the medium, until they enter the boundary layer. The so-called *blowing* of the pyrolysis gases generates a thermal barrier in front of the heat shield, since they are at a lower temperature than the boundary layer. Moreover, these gases may locally change the radiation, conduction and convection properties of the flow, increasing the cooling effect [17]. Most resins contain carbon, hydrogen and oxygen elements and, eventually, residual compounds from the manufacturing process [17]. Therefore, as the resin pyrolyses, it also leaves a carbonaceous residue called *char* coating the carbon fibers. Whilst the pyrolysis layer represents the material region in which the degradation takes place, the char layer constitutes the area for which the decomposition has been completed. Other solid carbon can be deposited when the pyrolysis gases flow through the char layer (coking), so that a material density increase can be detected [18]. The high emissivity of the char improves the re-radiation capability of the material and, coating the carbon fibers, it also reinforces their structure [17]. Finally, the char can be removed thermally (sublimation), mechanically (spallation) and, considering its high carbon content, it can undergo oxidation too [16].

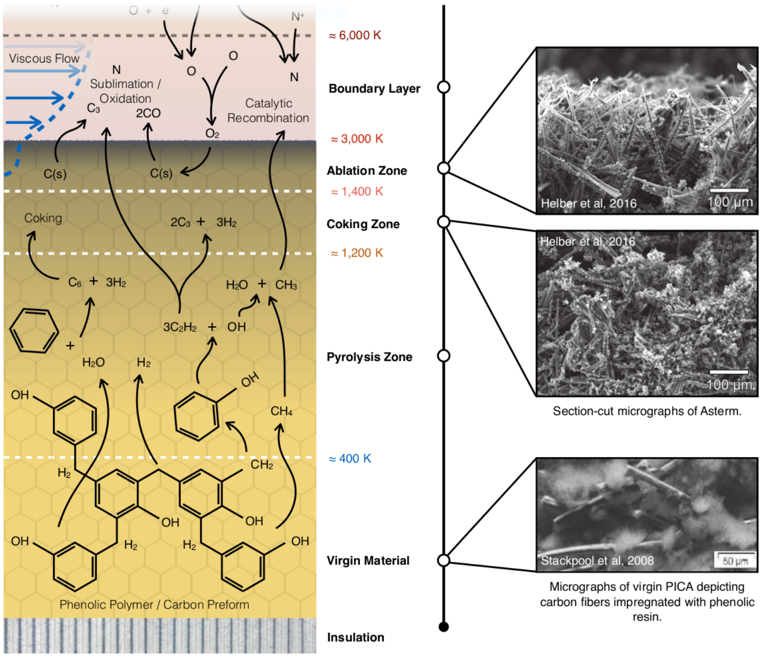

Figure 1.6: Material response of a charring carbon-phenolic ablator. Credits: [15].

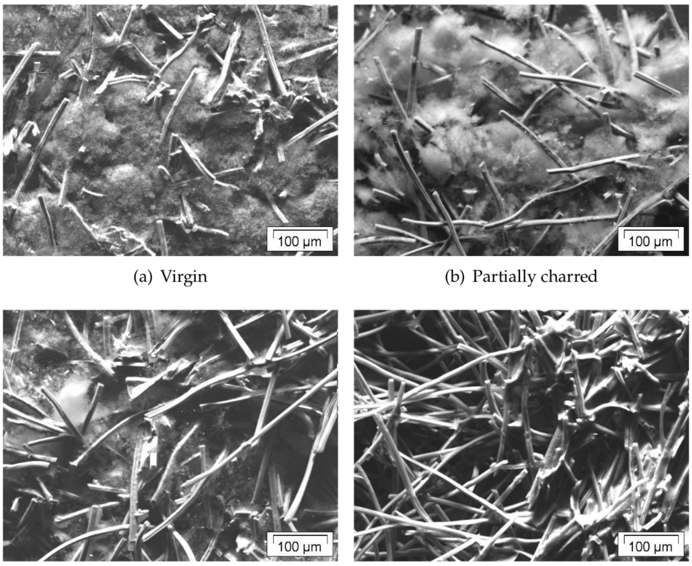

(a) Virgin (b) Partially charred (c) Charred (d) Ablated

Figure 1.7: Micrographs of PICA during thermal degradation. Picture taken from [11].

A final observation concerns the flow regime, which characterizes the ablation as a surface or volume phenomenon [11]. According to Lachaud et al. [19], the ablation of dense materials is usually described in terms of surface recession as the mass loss occurs superficially. In porous media (such as P50 and PICA), depending on physical conditions, surface ablation may be not enough accurate, as ablation may be a volume phenomenon: oxidation, sublimation and spallation may occur inside the pores. This characteristic behaviour depends on the depth of diffusion driven by heterogeneous reactions. Diffusion is the physical mechanism allowing the gaseous species to come into contact with the solid ones, so that a heterogeneous reaction may occur. In particular, a competition between diffusion and chemical kinetics is established. If the diffusion velocity is very high, the oxidant has enough time to go deep into the material and the recession occurs from the inside (volume ablation). Therefore, the amount of chemical products is limited by chemical kinetics and this is why it is referred to reaction limited ablation regime. Instead, a diffusion limited process takes place when the oxidation is very quick and the consumption of the oxidant occurs at the external surface (surface ablation) [19]. A comparison between volume and surface ablation of a carbon preform is shown in Figure 1.8.

1.3 QARMAN re-entry CubeSat

The *QubeSat for Aerothermodynamic Research and Measurements on AblatioN* (QARMAN), is an Atmospheric Entry Demonstrator designed and manufactured for the European Space Agency (ESA) by the von Karman Institute (VKI) for Fluid Dynamics. The main

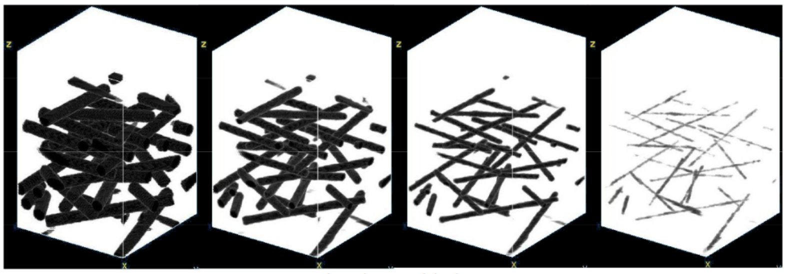

a) Volume ablation

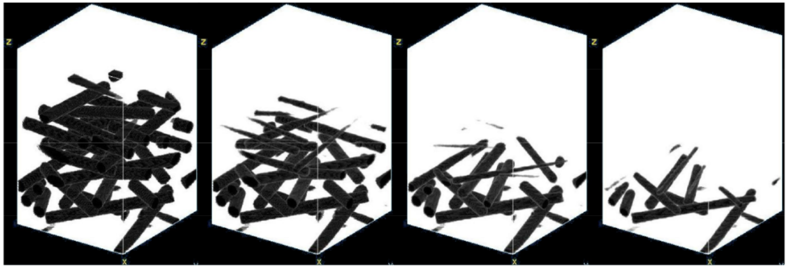

b) Surface ablation

Figure 1.8: Comparison between volume and surface ablation of a carbon preform. Figure modified from [19].

task of this project is to prove the potentiality of a CubeSat nano-satellite to collect significant scientific data during orbit and atmospheric re-entry, which will be performed at Mach 27. Equipped with a Cork P50 heat shield, Qarman will test in flight environment the thermal protection capabilities of the new cork-based ablative TPMs, providing a precious contribution to aerothermodynamic research field.

Qarman is a three-unit standard CubeSat (Figure 1.9), with dimensions $34 \times 10 \times 10$ cm and a total mass of 4 kg [7]. While its blunt nose is covered with cork, the titanium side walls are protected by a ceramic material, the silicon carbide (SiC). These two TPSs constitute the payload itself because they will be object of study during the in-flight experiments [20]. Several temperature and pressure probes and one emission spectrometer are contained inside. Furthermore, the Aerodynamic Stability and De-orbiting Device (AeroSDS) will be used to stabilize and de-orbit the spacecraft; this is a passive attitude stabilization system, made up of SiC deployable panels equipped with solar cells.

The mission profile of Qarman is shown in Figure 1.11. It was lifted-off from Cape Canaveral to the International Space Station (ISS) on the 5th of December 2019, by a Falcon 9 lift launch vehicle after it was integrated into the SpaceX's Dragon capsule. Then, it was deployed in orbit from ISS on the 19th of February 2020, starting its mission. It will orbit around Earth for few months and, finally, the atmospheric re-entry is estimated for the end of August 2020 when, at the end of the black-out period, the scientific data will be transmitted via the IRIDIUM constellation, right before the crash of the vehicle. Once the mission has been successfully accomplished, the measurement data gathered during re-entry will be used to better characterize the ablation processes and validate the numerical tools for hypersonic flow simulations.

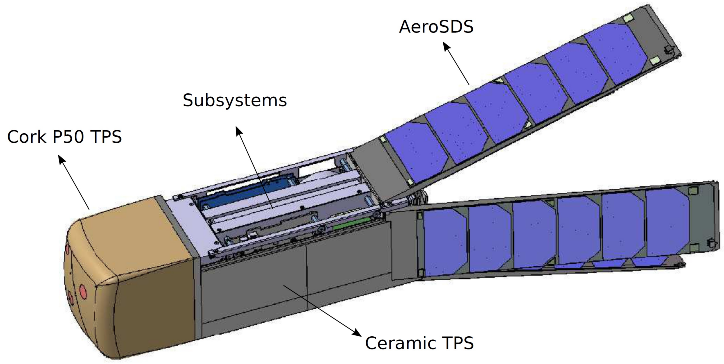

Figure 1.9: QARMAN CubeSat with side panels deployed. Figure taken from [7].

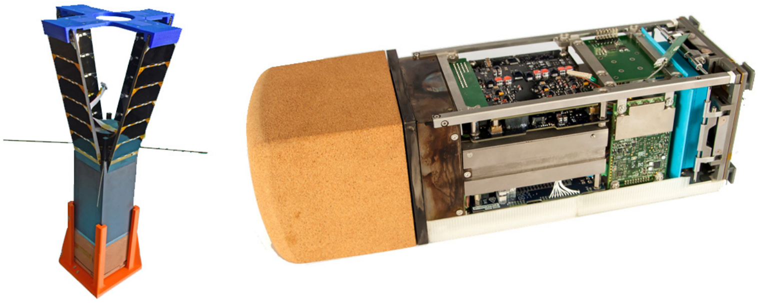

Figure 1.10: Pictures of QARMAN CubeSat. The Cork P50 is used to cover the nose of the vehicle.

1.4 State of the art

In this section, the results of the experiments conducted in the last years about the TPS of QARMAN will be shortly discussed, as well as the available numerical tools chosen for the simulation of its atmospheric re-entry.

1.4.1 Experimental campaigns

The first QARMAN experiments have been performed by Sakraker [7] in the VKI Plasmatron facility (Figure 1.12), an inductively-coupled plasma (ICP) wind tunnel capable of generating a jet of plasma. This high-enthalpy flow is produced by heating a gas to temperatures up to 10000 K, in order to study the thermochemistry of materials. The results of this experimental campaign were very significant, since they remarked the swelling behaviour of the Cork P50. This is a feature of cork-based TPMs, for which specific and complete numerical models do not exist yet. The large amount of numerical approaches developed in the last years were indeed concentrated on the ablation of PICA-like materials but, since carbon-phenolic materials do not undergo swelling, most of modern ablation numerical models are not able to predict this complex behaviour [7]. Therefore, the modeling of swelling is one of the main objectives of this work.

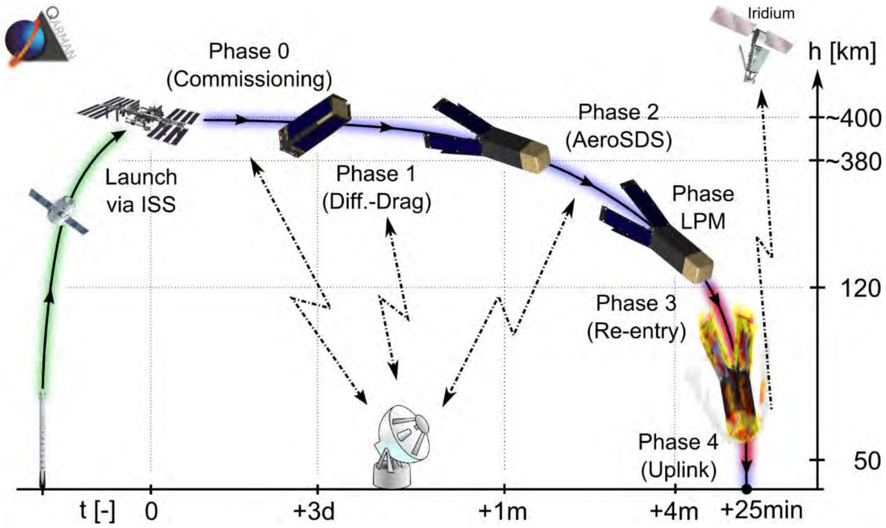

Figure 1.11: Mission profile of the QARMAN CubeSat.

In addition to the test in Plasmatron, Sakraker [7] also conducted a thermogravimetric analysis (TGA) to study the thermal decomposition of the Cork P50, in order to fit an Arrhenius law describing the pyrolysis reactions.

Figure 1.12: QARMAN sample during (left) and after (right) the test in Plasmatron. Figure modified from [7].

A further test of the full scale CubeSat has been performed at Centro Italiano Ricerche Aerospaziali (CIRA) in the arc-jet SCIROCCO facility (Figure 1.13), in order to verify the structural integrity and to get useful data for validation purposes [21].

1.4.2 Numerical tools

Considering the exceptionality of in-flight experiments and the complexity of reproducing in a ground facility the atmospheric re-entry conditions, numerical simulations represent an essential and powerful solution. The first analyses and computational procedures for the simulation of charring ablative materials (CMA) were developed in the 1960s,

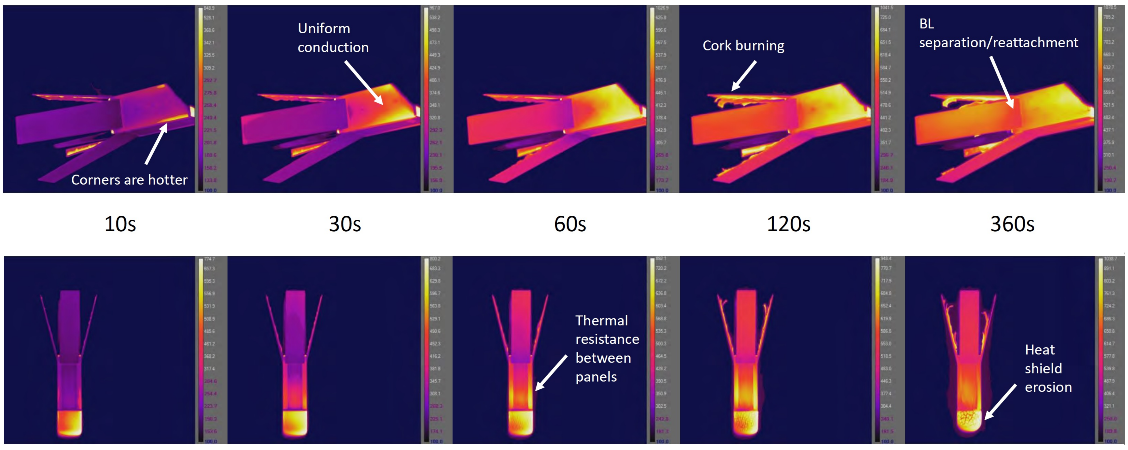

Figure 1.13: Qarman CubeSat during the test in SCIROCCO facility. Credits: [21].

through a series of NASA technical reports [22], [23], [24], [25], [26], [18], providing solutions to couple the charring ablator response with a chemically reacting boundary layer. In the 1970s, these studies were continued with the contribution of Clark [27]. In the 1990s, the FIAT (*Fully Implicit Ablation and Thermal-response*) numerical tool was developed at NASA Ames Research Center [28], in order to perform one-dimensional analysis of ablation and as sizing tool for TPMs. The capabilities of FIAT were also improved over the years [29], [30], [31]. In the 2000s, the TITAN (*Two-dimensional Implicit Thermal-response and AblatioN*) [32], [33] and the 3dFIAT codes [34], [35] were developed to extend the ablation simulations to two-dimensions and three-dimensions, respectively. These numerical tools can simulate several physical phenomena within the TPS material: the heat conduction, thermal decomposition, quasi-steady pyrolysis gas flow, and surface ablation [36]. However, treating ablation as a surface phenomenon is a questionable assumption if applied to low-density materials, in which the internal mass removal allowed by the porous structure should be strongly considered too. Even today, most of the modern codes still dissociate the material response from the flow field and the interaction between these two environments is studied coupling two distinct solvers [37]. Specifically, according to Turchi et al. [37] and Schrooyen [11], four numerical approaches can be identified:

1. *Material solver*: the heat conduction inside the material is computed and simplified boundary conditions are applied at the gas-surface interface, by means of mass and energy balance at wall [9]. For instance, the code developed by Lachaud et al. [38] belongs to this category.

2. *Flow field solver*: a CFD simulation is performed to solve the external fluid region and an ablation boundary condition is used to treat the surface ablation. In addition to the computation of the Navier-Stokes equations, the ablation products are injected in the flow field [39]. An example is given by Nompelis et al. [40].

3. *Loosely coupled*: the first two approaches are combined together, by means of a

coupling method between the material response code and the CFD solver, as done by Martin et al. [41].

4. *Fully coupled*: a unified strategy is used to solve both the flow field and the material response within the same computational domain [11].

A comprehensive outline of the different numerical approaches is shown in Figure 1.14. The fully coupled methods represent the most modern solution and they are very promising for the simulation of highly porous ablative materials, because they allow to take into account the volume ablation phenomenon. For this thesis, particularly worthy of note is the work of Schrooyen [11], who developed a continuum approach capable of treating the macroscopic flow through the porous medium. Specifically, the theory of volume averaging is applied to the Navier-Stokes equations, in order to describe the gradual transition from the pure fluid region to the porous material. Then, this *Unified Approach* has been implemented within the multi-physics CFD code Argo, developed at Cenaero. This numerical tool has been first used for the ablation simulation of a carbon preform material [42], [43]. Later, Coheur et al. [13] added a module for pyrolysis, in order to simulate a charring carbon-phenolic TPM and replicate the TACOT (*Theoretical Ablative Composite for Open Testing*) experiment [44], [45], [46].

This is the background in which the current work has to be set and the motivation behind it is to further enhance the capability of Argo, in order to offer an increasingly attractive numerical tool capable of solving complex physical problems. For instance, a new method of computing the pyrolysis gas should be developed, since its chemical composition has been treated as known and constant so far. A further goal is to extend the capability of this computational tool to the treatment of cork-phenolic TPMs, such as the Cork P50. For this reason, an additional modeling effort is required, because the cork-based materials are noted to swell. Martinez [47] has already conducted a literature review of swelling for porous materials and performed some numerical tests in Matlab, showing the necessity to develop a physical model ensuring the solid mass conservation. These aspects represent the starting point of this thesis and they will be theoretically and numerically investigated and then supported through test cases and simulations.

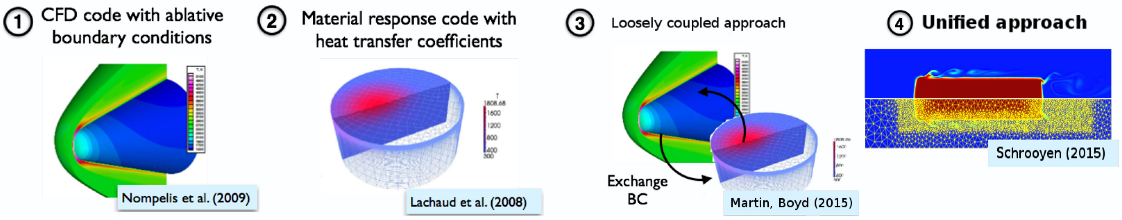

Figure 1.14: Numerical approaches for the study of ablative materials. Credits: [13].

1.5 Objectives

This work aims to explore and provide new and improved methodologies for modeling and simulation of cork-phenolic thermal protection materials. In fact, the excellent thermal and mechanical properties of cork make it one of the best available solutions for the heat shield of re-entry vehicles, such as the QARMAN CubeSat. Hence, two main objectives will be pursued in this work, differentiated according to the two physical phenomena to be studied:

1. **Pyrolysis**: this work aims first to propose a method to compute the chemical composition of pyrolysis gases, rather than fixing it for the whole simulation. A simplified method to assess the elemental composition of pyrolysis gases will be investigated and a function calling the VKI library MUTATION++ will be implemented within the multi-physics CFD code ARGO, in order to compute the species mass fractions of the pyrolysis gas at equilibrium. It should be noted that this accurate approach is not necessarily applicable only to cork-phenolic TPMs, but to carbon-phenolic ones too.

2. **Swelling**: the second task is to develop a physical model accounting for swelling of porous cork-based TPMs. Once a model is devised, it will be implemented in a MATLAB code in order to be numerically tested. If the results fulfill the expectations, the aim for the future is to implement this physical model within ARGO, in order to perform a complete simulation of a cork-phenolic ablator.

A road map describing the work flow is shown in Figure 1.15.

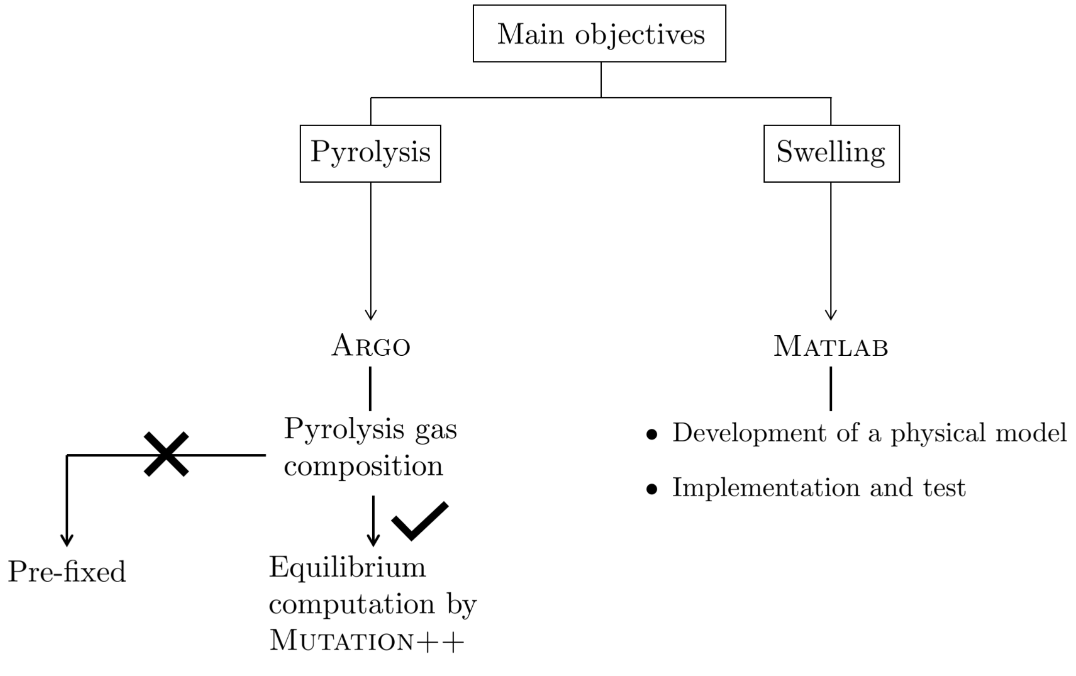

Figure 1.15: Road map describing the work flow.

Chapter 2

Thermochemical behaviour of cork-based materials

Cork is extracted from the bark of the Cork Oak tree (*Quercus Suber L.*) [14]. Silva et al. [48] define cork as a homogeneous tissue made up of thin-walled cells, arranged in a honeycomb structure, as shown in Figure 2.1. Thanks to its mechanical properties, cork is often used in building [49] and, recently, it is also receiving increasing attention in Aerospace industry for its great thermal properties, as evidenced by those TPS applications in which it has been successfully used. In fact, its low conductivity and low density reduce the amount of heat transferred by conduction.

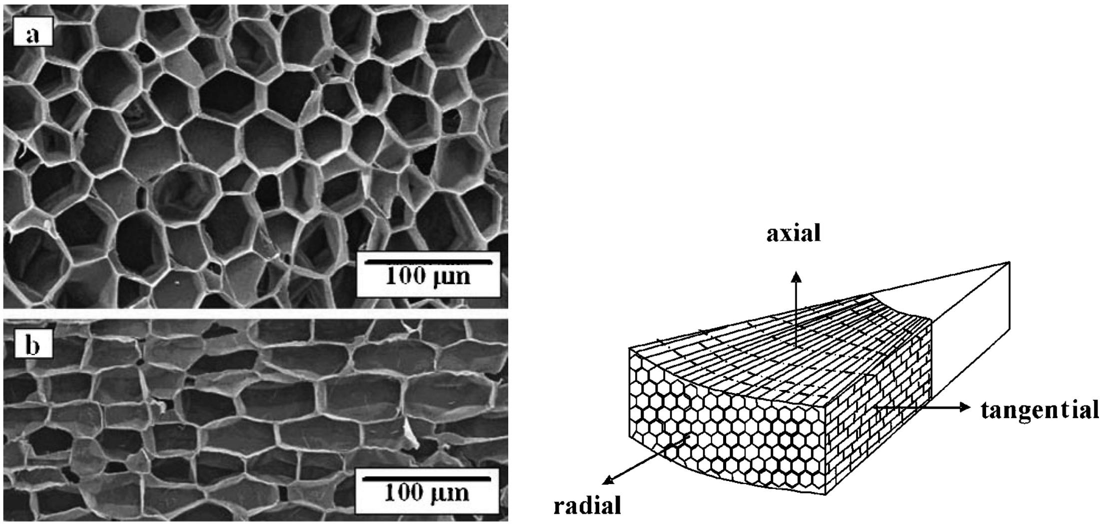

Figure 2.1: On the left, micrographs of cork. (a): radial section; (b): tangential section. On the right, representation of the arrangement of the cells. Credits: [48].

In modern ablative TPMs, cork is often combined with a charring resin, in order to enhance the pyrolyzing capabilities of the material. For instance, the Cork P50 used as TPM of QARMAN CubeSat is an agglomerate of cork granules, bound together by a phenolic resin; the latter constitutes the filling matrix, while cork acts as a rigid precursor, as well as the carbon fibers in PICA. However, while in carbon-phenolic TPMs the resin is the only charring component, in cork-phenolic materials cork undergoes pyrolysis too (Figure 2.2).

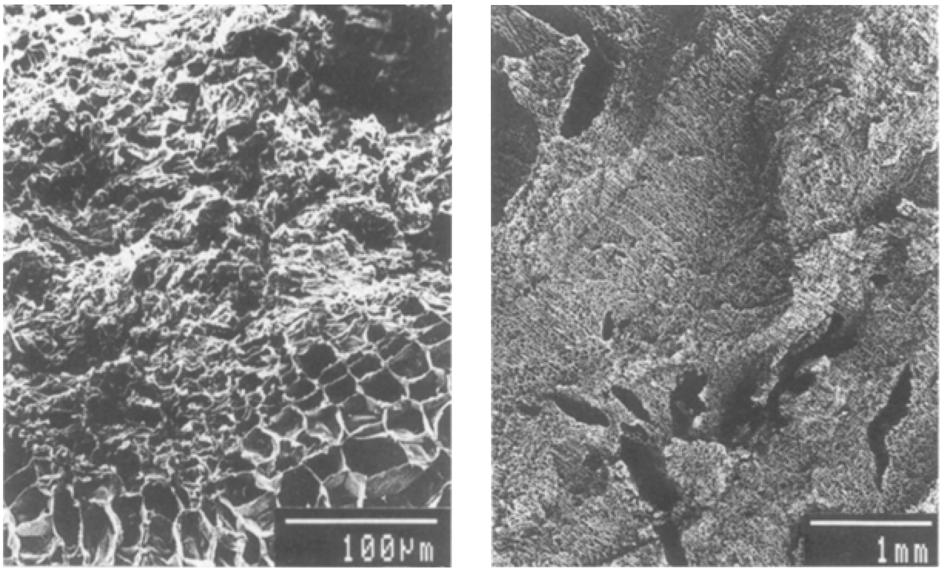

Figure 2.2: Cork heated at 620 K. On the left, a charred zone can be observed at the top. On the right, a picture showing the cracked structure of charred cork. Credits: [49].

A large number of studies is available in literature about the thermochemical degradation of cork, but pyrolysis is not its only characteristic phenomenon; as previously mentioned, cork is indeed a swelling material. Since understanding these phenomena is essential to improve numerical models and to make the right assumptions about the material behaviour, they will be briefly examined in the following sections.

2.1 Pyrolysis

The thermal behaviour of the Cork P50 has been previously investigated at VKI, through a series of experiments. A thermogravimetric analysis (TGA) was performed by Sakraker [7] to study the pyrolysis mechanisms. Two cork P50 samples were heated at rate of 10 K/min using Argon, in order to avoid oxidation and nitridation reactions. The TGA analysis evidenced that the material starts to decompose at 430 K, while at 780 K the samples are totally charred. Furthermore, a mass loss of 24.5% has been observed.

Sakraker [7] also conducted other experiments in the VKI Plasmatron facility, as shown in Figure 2.3: once the sample is fully charred, the typical black and cracked surface can be observed. A similar test was performed by Asma et al. [50] and thermocouples measured a relatively low temperature inside the sample. Moreover, both pyrolysis and char ablation exhibited an almost uniform behaviour (Figure 2.4). Finally, a very interesting result is related to the mass loss: the removal of solid mass caused by pyrolysis reactions was much higher than the one due to ablation. This makes understanding the

Figure 2.3: On the top: surface of the cork P50 from virgin (left) to fully charred (right), after a test in Plasmatron. On the bottom: section of the charred sample. Pictures taken from [7].

pyrolysis mechanism a crucial point, because it provides the main contribution in terms of cooling effect during atmospheric re-entry.

Figure 2.4: Back view of fully charred cork P50, after a test in Plasmatron. Picture taken from [50].

These data are precious for numerical simulations too. However, before embarking on the discussion about pyrolysis modeling, it is important to put in evidence the main physical aspects related to the degradation of cork-phenolic materials. When subjected to heat, the Cork P50 undergoes thermochemical decomposition of both cork and phenolic resin. Considering the high level of void fraction, products of pyrolysis are able to percolate through the pores, by means of diffusion and convection mechanisms, so that an outgassing phenomenon can be observed at the interface between the solid and the chemically reacting boundary layer. During their transport, under specific thermochemical conditions, the pyrolysis gas species may react with each other or with the external hot gases. Hence, the chemical composition of pyrolysis gases is expected to change. In other words, the hypothesis of thermochemical non-equilibrium should be extended to pyrolysis gases. This further problem points out the criticality of knowing the chemical composition of the pyrolysis products, so that simplified assumptions are usually required.

2.1.1 Typical modeling assumptions

In modeling the pyrolysis gases, the assumption of thermochemical equilibrium at the local temperature and pressure is typically done in material response codes, as asserted by Rabinovitch et al. [17], even though this hypothesis sometimes is responsible for exothermic behaviour [38]. The assumption of equilibrium chemistry for pyrolysis gases simplifies the computation and it is not so unreasonable, considering that the flow through the pores is relatively slow, but even so, the elemental composition of pyrolysis gas is nonetheless needed. Most resins contain carbon, hydrogen and oxygen elements and, eventually, residual compounds from the manufacturing process. The same elements (C:H:O) are also present in the pyrolysis gas mixture but, due to the charring phenomenon, its elemental composition is significantly different from the one of the virgin material and it is an additional unknown [17]. Moreover, although the elemental composition of pyrolysis gases is often assumed to be constant in most of numerical models, it is actually a function of temperature, pressure and heating rate [38]. In particular, Rabinovitch et al. [17] showed how mixture enthalpy is sensitive to the variation of the elemental composition and the chemical species considered, as well as to the consideration of a finite-rate chemistry, instead of equilibrium.

2.2 Swelling

The cork-phenolic P50 has an atypical behaviour because most of the modern ablative TPMs, like PICA, don't exhibit a swelling behaviour [7]. During atmospheric re-entry, high temperatures let the cork achieve a proper viscoelastic state, so that it becomes sufficiently flexible to expand under the pressure of the pyrolysis gases trapped inside the pores [51]. Figure 2.5 shows the response of a cork sample heated at 570 K. In addition to the thermal expansion of the cells, the walls stretch and their thickness decreases and, once pyrolysis is over, the honeycomb structure is totally demolished. [49].

Sakraker [7] measured the swelling-recession profiles (Figure 2.6) of a P50 sample in Plasmatron, by means of a high speed camera. The material exhibited a thermal expansion (green line) in the first 24.85 seconds, while the recession (blue line) stopped after 99.85 seconds. Furthermore, Figure 2.7 shows how the swelling duration and thickness depend also on the chamber pressure and the heat fluxes generated by the plasma torch.

The experimental campaigns conducted on cork have therefore highlighted a peculiar thermal response mechanism, so it should be taken into account in the numerical simulations of cork-based TPMs, in order to get more realistic predictions. Actually, before diving into modeling matters, a literature review is needed to seek possible solutions.

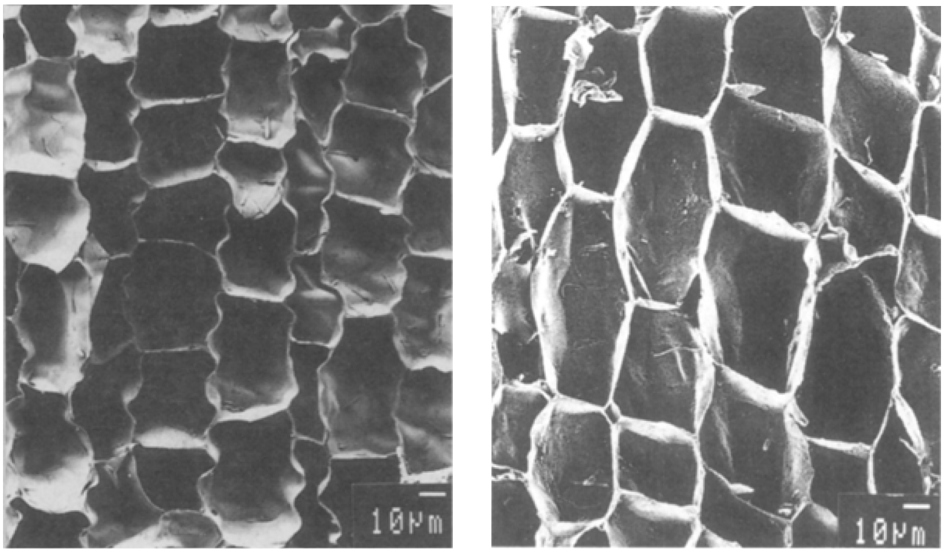

Figure 2.5: SEM images of the radial section of virgin cork (left) and response of the sample treated at 570 K, showing the expansion of the cells (right). Pictures taken from [49].

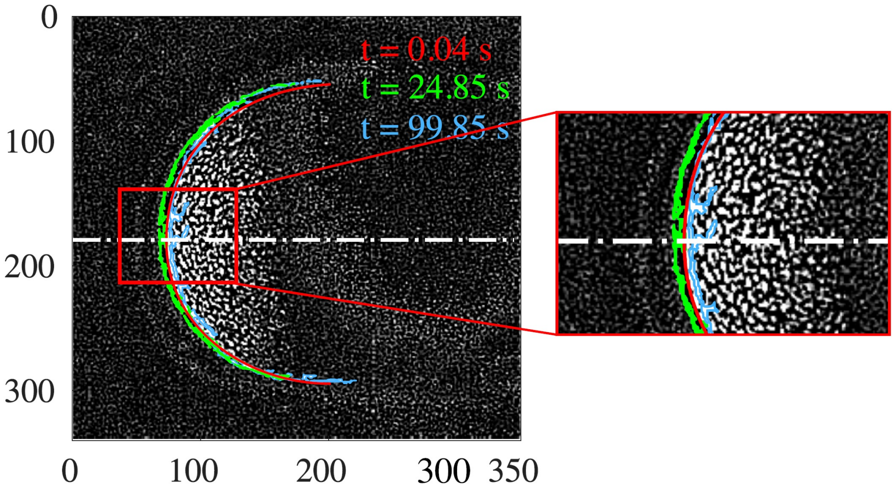

Figure 2.6: Picture captured by a high speed camera showing the swelling-recession profiles of a P50 sample in Plasmatron. Credits: [7].

2.2.1 Available modeling solutions

Martinez [47] carried out a first literature review concerning the modeling of swelling materials. A large part of the references is based on previous studies about pyrolysis of wood and intumescent systems, such as propellants and fire-retardants. In this work, these and other interesting approaches have been explored, and a short revision will be proposed in the following.

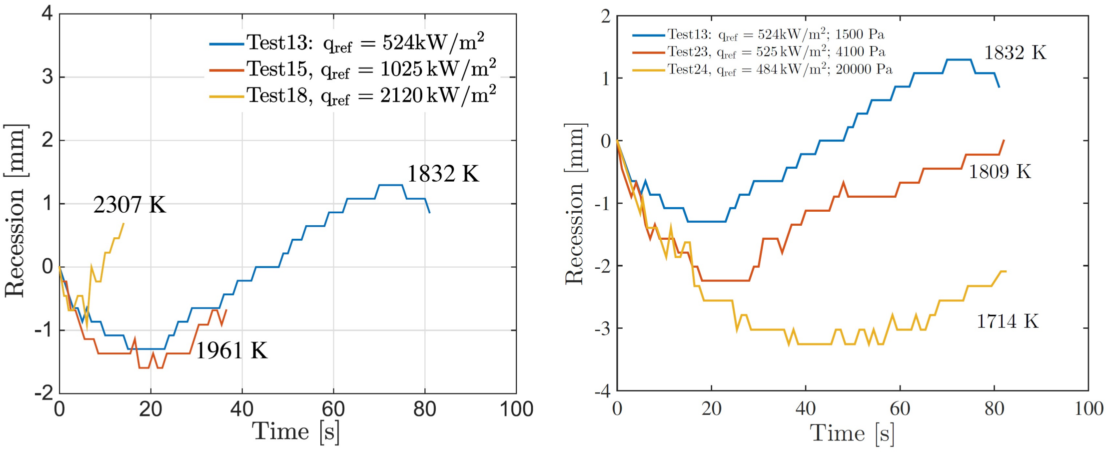

Figure 2.7: Effect of different heat loads and pressure on the swelling/recession profile. Plots taken from [7].

A mechanics approach

A first approach is the one proposed by Kuborn et al. [52], based on the shrinkage phenomenon of wood during drying and pyrolysis. This is also the method that Martinez [47] has found most promising. The initial premise of the authors is based on a physical observation: the shrinkage of wood during pyrolysis cannot be treated without taking into account its mechanics. Therefore, wood is treated as a deformable body, assuming that its structure and its mechanical properties strongly affect its response during the thermal decomposition. Concerning the structure, wood is an orthotropic material, because of the presence of three orthogonal symmetry planes, as illustrated in Figure 2.8. Therefore, the properties of wood change along three directions. Knowing that pyrolysis leads to

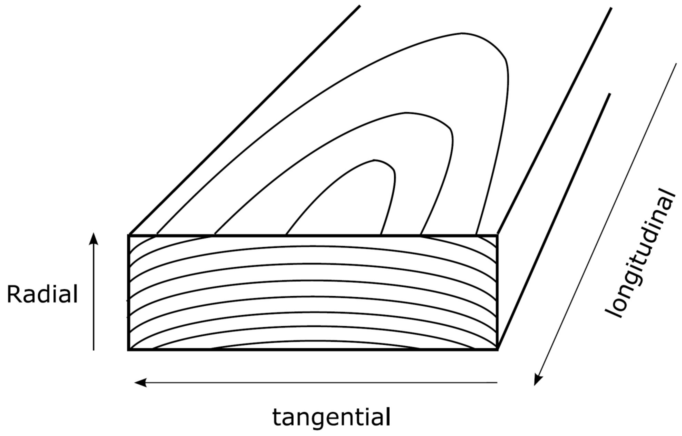

Figure 2.8: Orthotropic structure of wood. The presence of three mutually perpendicular axes can be observed. Credits: [52].

the production of gaseous species, wood is also treated as a porous medium, so that:

$$\phi_g + \phi_s = 1 \tag{2.1}$$

where ϕ_g is the gaseous volume fraction (also known as *porosity*), while ϕ_s is the solid volume fraction. Considering an average control volume $\mathrm{d}V = \mathrm{d}V_g + \mathrm{d}V_s$, characterized by the presence of a gaseous phase (denoted with subscript g) and a solid one (indicated by s), the volume fractions can be defined as follows:

$$\phi_g = \frac{\mathrm{d}V_g}{\mathrm{d}V}, \quad \phi_s = 1 - \phi_g = \frac{\mathrm{d}V_s}{\mathrm{d}V} \tag{2.2}$$

Hence, this model requires to express the mass, momentum and energy balance equations in terms of volume fractions, in order to describe a multiphase system. Hence, fluid dynamics and mechanics are combined together to predict the swelling behaviour. The mathematical model can be directly derived from physical insights: once subjected to heat, the solid phase undergoes a thermal decomposition so that a solid mass loss is expected, accompanied by an increase in the gaseous mass, due to the gas production associated with pyrolysis reactions. Naturally, an energy exchange between the two phases is expected too, so an additional term related to the interfacial heat transfer should be taken into account. A momentum balance should be also considered, but the solid phase deserves a special consideration. In fluid dynamics and heat transfer problems, solid materials are generally treated as rigid and stationary, i.e. characterized by a zero velocity. At the contrary, solid mechanics studies the behaviour of materials when they are subjected to forces, for the purpose of predicting their response in terms of strains and displacements. The combination of the two branches thus requires to define a velocity for solid materials too. This is the main point of the model proposed by Kuborn et al. [52]. The shrinkage of wood is indeed modeled with the aim of computing the velocity of the solid phase v_s, that actually is a strain rate. The intent of this overview is thus to focus on the salient points of the model, which are in the mass and momentum conservation equations written for the solid phase. The solid mass balance is given by:

$$\frac{\partial}{\partial t}\phi_s + \nabla \cdot (\phi_s v_s) = \sum_i \frac{\dot{\omega}_{s,i}}{\rho_{s,i}} \tag{2.3}$$

where σ_s is the mechanical stress tensor, while $\dot{\omega}_{s,i}$ and $\rho_{s,i}$ are respectively the production rate and the density of each solid species. Therefore, the term on the right-hand side of the equation is related to chemical mass production. The momentum conservation law in continuum mechanics is expressed by the indefinite equilibrium equations for the solid phase:

$$\nabla \cdot (\phi_s \sigma_s) + f = 0 \tag{2.4}$$

where, f represents the momentum exchanged between the two phases and it is given by:

$$f = p_g \nabla \phi_s + \delta v_g \tag{2.5}$$

p_g is the thermodynamic pressure, so the first term expresses the stress imposed by hydrostatic pressure to the solid phase and naturally connected to the solid volume fraction gradient. The second term describes the drag force imposed to the gas by the presence of the solid phase and it is proportional to the velocity of the gaseous phase by an interfacial drag coefficient δ. Considering that, in equation (2.4), the divergence of stress tensor is directly connected to the shrinkage phenomenon and has thereby a stronger effect than the momentum f exchanged between the two phases, f can be neglected:

$$\nabla \cdot (\phi_s \sigma_s) = 0 \tag{2.6}$$

Moreover, wood is considered as a linearly elastic porous medium, i.e. one that obeys the generalized *Hooke's law*:

$$\sigma_s = C_s \ \varepsilon_s \tag{2.7}$$

where ε_s is the mechanical strain vector and C_s is the matrix of the elastic stiffness coefficients. In general, this is a 9×9 square matrix containing 81 elements (elastic constants). However, the property of reciprocity implies that $\sigma_{ij} = \sigma_{ji}$, therefore the stiffness matrix C_s is actually 6×6. Defining the mechanical displacement vector of the solid u_s and assuming infinitesimal strains, the strain-displacement relations are given as follows:

$$\varepsilon_s = \frac{1}{2}\left(\nabla u_s + \nabla u_s^T\right) \tag{2.8}$$

Equations (2.8) and (2.7) can be substituited into equation (2.6), so that:

$$\nabla \cdot \left[\phi_s C_s \frac{1}{2}\left(\nabla u_s + \nabla u_s^T\right)\right] = 0 \tag{2.9}$$

This equation allows to compute the mechanical displacement field u_s and, finally, the solid velocity is given by:

$$v_s = \frac{\partial u_s}{\partial t} \tag{2.10}$$

For orthotropic materials like wood, the stiffness matrix is defined as:

$$C_s = \begin{bmatrix} C_{11} & C_{12} & C_{13} & 0 & 0 & 0 \\ C_{12} & C_{22} & C_{23} & 0 & 0 & 0 \\ C_{13} & C_{23} & C_{33} & 0 & 0 & 0 \\ 0 & 0 & 0 & C_{44} & 0 & 0 \\ 0 & 0 & 0 & 0 & C_{55} & 0 \\ 0 & 0 & 0 & 0 & 0 & C_{66} \end{bmatrix} \tag{2.11}$$

This means that there is no interaction between the normal stress σ_{11}, σ_{22}, σ_{33} and the shear strains ε_{23}, ε_{13}, ε_{12}, which are associated to different planes. Unfortunately, the limit of this approach is related to C_{ij} coefficients, which are not available in literature for cork and they should be determined experimentally.

A semi-empirical heat transfer model

Anderson et al. [53] developed a one dimensional heat transfer model, assuming the swelling to be a function of total mass loss. The analysis concerns an intumescent system protecting a substrate. When the virgin material is subjected to heat (Figure 2.9),

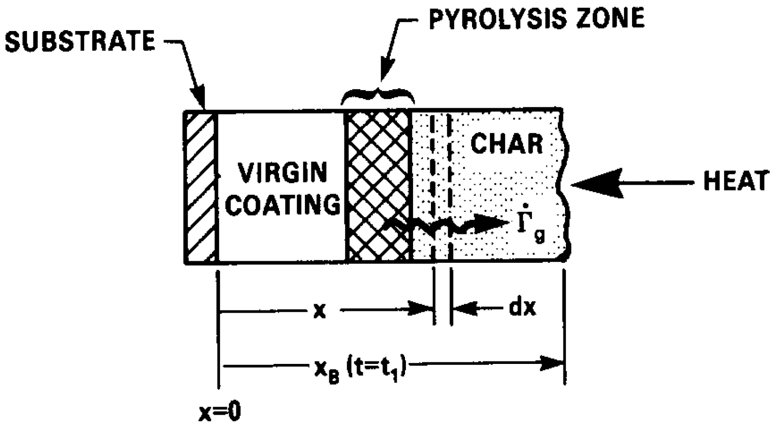

Figure 2.9: A scheme of the model proposed by Anderson et al. [53].

pyrolysis takes place so that a carbonaceous residue is produced and part of the solid mass is lost because of the outgassing $\dot{\Gamma}_g$ of the pyrolysis chemical species. Therefore, the pyrolysis zone expands at a velocity v, due to the gas pressure.

The problem is described coupling the continuity and energy conservation equations:

$$\frac{\mathrm{d}\rho}{\mathrm{d}t} + \rho\frac{\partial v}{\partial x} = -\dot{\Gamma}_g \tag{2.12}$$

$$\rho C_p\frac{\partial T}{\partial t} = \frac{\partial}{\partial x}k\frac{\partial T}{\partial x} - (h_g - h)\dot{\Gamma}_g - v\rho C_p\frac{\partial T}{\partial x} - \rho\dot{q}_{\mathrm{chem}} \tag{2.13}$$

where ρ is the solid density, v is the intumescence velocity, $\dot{\Gamma}_g$ is the production rate due to pyrolysis, C_p is the specific heat, k is the thermal conductivity, T is the temperature, h and h_g are the specific enthalpies of the solid and gas and $\dot{q}_{\mathrm{chem}}$ is the rate of heat per unit mass produced by chemical reactions [53]. The intumescence velocity can be related to the other parameters as:

$$v(x,t) = \int_0^x \frac{-n}{m_0 - m}[E_f(m) - 1]\frac{\mathrm{d}m}{\mathrm{d}t}\,\mathrm{d}t \tag{2.14}$$

where m_0 is the initial mass, m is the current mass and E_f is an expansion factor that is defined as:

$$E_f(m) = 1 + \Big[(E_f)_{max} - 1\Big]\left(\frac{m_0 - m}{m_0 - m_c}\right)^n \tag{2.15}$$

where n is an exponent which describes how $E_f(m)$ depends on the variation in mass. Finally, the problem can be closed by means of TGA analysis, in order to track the mass removal and compute the production rate as follows:

$$\dot{\Gamma}_g = \frac{\rho_0}{E_f}\frac{\mathrm{d}(m/m_0)}{\mathrm{d}T}\frac{\mathrm{d}T}{\mathrm{d}t} \tag{2.16}$$

A two-energy equation model

Another approach, proposed by several authors, is based on the resolution of two energy conservation equations, one for the virgin material and the other one for the char layer, in order to consider the change of the physical properties due to thermal degradation.

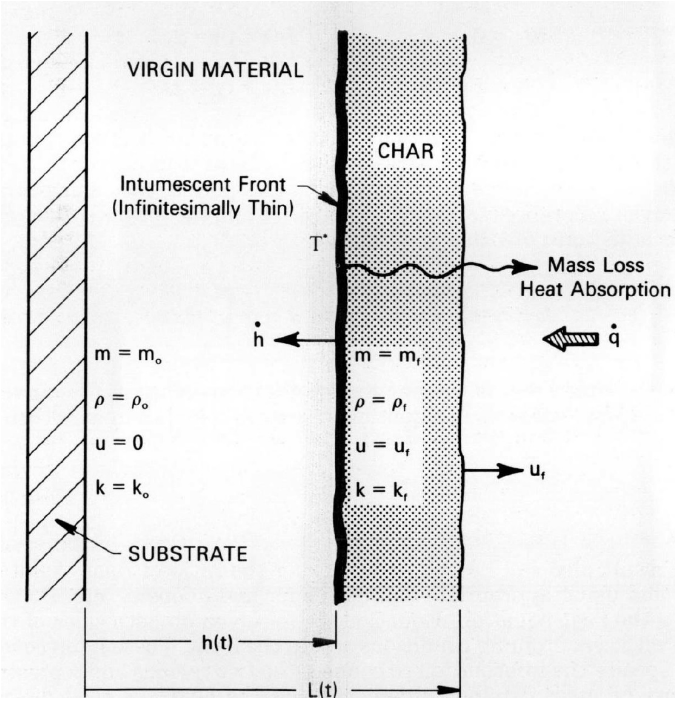

Figure 2.10: A scheme of the frontal model developed by Anderson et al. [51].

Anderson et al. [51] published another work for the purpose of improving the semi-empirical model and describing the thermal expansion as a function of not only mass loss but also temperature and mass loss rate. Therefore, they developed the so-called *frontal model*, shown in Figure 2.10: an intumescent front moving at a velocity $\dot{h}$ splits the material into two zones; in the virgin zone the particle velocity u is zero because the temperature is not enough high to trigger intumescence, whilst at the right of the front the char layer swells with a uniform velocity u_f. The energy conservation equation has to be solved within the two regions:

$$\rho C_p \left(\frac{\partial T}{\partial t} + u \frac{\partial T}{\partial x} \right) = \frac{\partial}{\partial x} k \frac{\partial T}{\partial x} \tag{2.17}$$

Moreover, the two energy fields have to be connected by means of specific jump conditions. Following this procedure, the char velocity can be computed as follows:

$$u_f = \dot{h} \left(1 - \frac{\rho_0 m_f}{\rho_f m_0} \right) = \dot{h} \left(1 - \frac{L_f}{L_0} \right) \tag{2.18}$$

A last work has been published by Buckmaster et al. [54], which revisited the same model and deepened it from a numerical point of view. Further details can be found in the references.

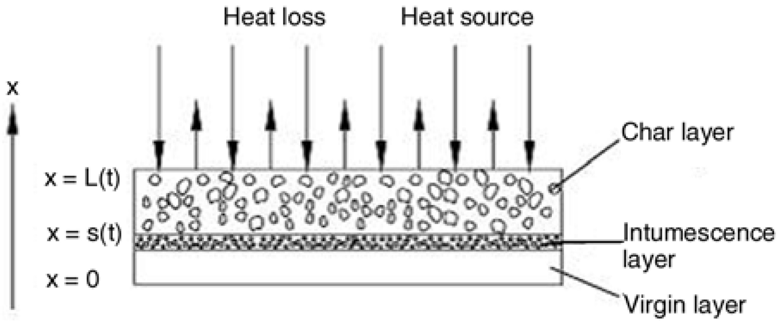

Figure 2.11: A scheme of the model developed by Zhang et al. [55].

Zhang et al. [55] developed a similar model based on the resolution of two energy conservation equations. This approach is schematized in Figure 2.11. If T_p is the pyrolysis temperature, in a *preheating stage* ($T < T_p$) a single energy equation is solved within the virgin material (denoted with subscript v):

$$\frac{\partial T_v}{\partial t} = \frac{k_v}{\rho_v c_v} \frac{\partial^2 T_v}{\partial x^2} \tag{2.19}$$

The boundary conditions are:

$$x = 0 \quad \longrightarrow \quad k_v \frac{\partial T_v}{\partial x} = 0 \tag{2.20}$$

$$x = L_i \quad \longrightarrow \quad k_v \frac{\partial T_v}{\partial x} = \dot{q}_{\text{ext}} - \varepsilon_v \sigma T_w^4 \tag{2.21}$$

where $\dot{q}_{\text{ext}}$ is the external heat flux, ε_v is the virgin material emissivity, σ is the Stefan–Boltzmann constant and T_w is the wall temperature.

When $T \geq T_p$, pyrolysis occurs and an *intumescent combustion stage* can be observed, so that it is possible to identify two regions separated by an intumescent layer, located in $x = s(t)$. Therefore, equation (2.19) has to be solved only within the virgin layer ($0 \leq x < s(t)$) with a different boundary condition at the interface:

$$x = 0 \quad \longrightarrow \quad k_v \frac{\partial T_v}{\partial x} = 0 \tag{2.22}$$

$$x = s(t) \quad \longrightarrow \quad T_v = T_p \tag{2.23}$$

At the same time, a second energy equation has to be solved within the char layer (denoted with subscript c, $s(t) < x \leq L(t)$), characterized by an intumescent velocity u:

$$\frac{\partial T_c}{\partial t} + u \frac{\partial T_c}{\partial x} = \frac{k_c}{\rho_c c_c} \frac{\partial^2 T_c}{\partial x^2} \tag{2.24}$$

Here, the boundary conditions are:

$$x = s(t) \quad \longrightarrow \quad T_c = T_p \tag{2.25}$$

$$x = L(t) \quad \longrightarrow \quad k_c \frac{\partial T_c}{\partial x} = \dot{q}_{\text{ext}} - \varepsilon_c \sigma T_w^4 \tag{2.26}$$

Finally, a jump condition is required at the interface between the two zones, $x = s(t)$:

$$\rho_v q_p \frac{\partial s}{\partial t} = k_v \frac{\partial T_v}{\partial x} - k_c \frac{\partial T_c}{\partial x} + u \rho_v q_i \tag{2.27}$$

where q_p is the heat of pyrolysis, q_i is the heat absorbed by intumescence process and $\partial s/\partial t$ is the velocity of the interface, which can be related to the intumescent velocity thorugh the variation in volume:

$$u = -\frac{\Delta V}{V_0} \frac{\partial s}{\partial t} \tag{2.28}$$

where, V_0 is the initial volume and ΔV its variation.

A final consideration

This last section presented three different models for the computation of the swelling velocity, with the intent to provide an overview of the possible numerical approaches to the swelling phenomenon. Although none of these models have actually been used in this work because an original approach has been expressly devised, they represented a starting point for the understanding of the problem. Moreover, they should be taken as a reference for the future, in view of further improvements.

Chapter 3

Physical modeling

This chapter deals with the modeling of highly porous ablative thermal protection materials for atmospheric entry applications. The governing equations of high-temperature and chemically reacting flows are first presented, including chemical non-equilibrium effects. The thermodynamic and transport properties will be discussed, as well as the chemical kinetics. Hence, the volume averaging theory is presented in the framework of the porous material treatment as a multiphase system. This is the founding element of the Unified Approach, a fully coupled method implemented within a multi-physics CFD code, Argo, that has been used to simulate the ablation of a thermal protection heat shield. In the second part of this chapter, the modeling of cork-based and charring ablators is examined, focusing on the physical phenomena of pyrolysis and swelling. Pyrolysis has already been modeled within Argo, therefore an accurate method to compute the pyrolysis gas composition is analyzed. On the contrary, the swelling prediction is still completely absent in this software, therefore an original model is exploited, for the purpose of preliminary testing it through a Matlab code.

3.1 Modeling of porous ablators by means of a Unified Approach

Ablation during atmospheric re-entry is a complex phenomenon under a physical point of view, but it is also challenging from a computational perspective. The simulation of such conditions requires a considerable modeling effort, due to the need to take into consideration several physical-chemical phenomena. It is necessary to specify that the study of the supersonic region and the bow shock capturing are beyond the scope of this work, as well as beyond the capabilities of the numerical tools chosen for the simulations. This work aims to study the interaction between a high-enthalpy flow and a reactive porous medium. Schrooyen [11] developed and implemented within Argo the *DGAblation* module, capable of solving ablation problems. In particular, it is able to treat multi-species compressible flows by means of a Discontinuous Galerkin Method (DGM). As already mentioned, a strong coupling strategy is used to gradually progress from the pure fluid region to the solid porous one. Therefore, the first part of this section presents the governing equations of fluid dynamics specialized for aerothermal flows. After the flow modeling part, the discussion will deal with the reactive porous material.

3.1.1 Navier-Stokes equations for viscous, high-temperature, non-equilibrium flows

In the framework of atmospheric entry flows, high-temperature and high-speed gas dynamics is involved. The physics of such flows is strictly connected to the flow regime, so that the choice of the mathematical model of governing equations must be made with care, depending on the Knudsen number. Ablation typically takes place at low altitudes along re-entry trajectory, below 60 km [11], where the continuum hypothesis is still valid. Such a flow is described by the Navier-Stokes balance equations for a viscous, high-temperature, chemically reacting and non-equilibrium flow, which express the mass, momentum and energy conservation[1]:

$$\frac{\partial \rho_i}{\partial t} + \nabla \cdot (\rho_i \mathbf{u}) = -\nabla \cdot (\mathbf{J}_i) + \dot{\omega}_i, \quad \forall i = 1, \dots, N_s \tag{3.1}$$

$$\frac{\partial (\rho \mathbf{u})}{\partial t} + \nabla \cdot (\rho \mathbf{u}\mathbf{u}) = -\nabla P + \nabla \cdot \boldsymbol{\tau} \tag{3.2}$$

$$\frac{\partial (\rho E)}{\partial t} + \nabla \cdot (\rho H \mathbf{u}) = -\nabla \cdot \mathbf{q} + \nabla \cdot (\boldsymbol{\tau} \cdot \mathbf{u}) + \dot{\omega}_T \tag{3.3}$$

where ρ_i is the density of each gaseous species, N_s is the number of chemical species, $\mathbf{u}$ is the velocity vector, $\mathbf{J}_i$ is the species diffusion flux vector, $\dot{\omega}_i$ is the chemical source term, P is the thermodynamic pressure, $\boldsymbol{\tau}$ is the viscous stress tensor, E is the total (non-chemical) energy per unit mass, H is the total (non-chemical) enthalpy per unit mass, $\mathbf{q}$ is the heat flux vector and $\dot{\omega}_T$ is the energy contribution related to the chemical production term. The viscous stress is defined as:

$$\tau_{ij} = \mu \Big[\Big(\frac{\partial u_j}{\partial x_i} + \frac{\partial u_i}{\partial x_j} \Big) - \frac{2}{3} (\nabla \cdot \mathbf{u}) \delta_{ij} \Big] \tag{3.4}$$

where μ is the dynamic mixture viscosity and δ_{ij} is the Kronecker delta. Furthermore, the Stokes' hypothesis has been enforced for the bulk viscosity:

$$\lambda = -\frac{2}{3} \mu \tag{3.5}$$

Concerning what has been referred to *total* energy E, it is actually a *total non-chemical* energy, according to the formulation of Poinsot for combustion [56]. Hence, E is given by the sum of sensible and kinetic energies:

$$E = e + \frac{\mathbf{u}^2}{2} \tag{3.6}$$

---

[1] The notation of Schrooyen [11] is adopted.

Treating a multi-species reactive flow, the heat of formation of each species has thus to be included in the source term $\dot{\omega}_T$. Furthermore, according to statistical thermodynamics, the internal energy of a molecule can be modeled as:

$$e' = e'_{\text{trans}} + e'_{\text{rot}} + e'_{\text{vibr}} + e'_{\text{el}} \tag{3.7}$$

These indicate respectively the translational, rotational, vibrational end electronic energies. Actually, the temperature model implemented within Argo does not take into account vibrational and electronic degrees of freedom. Therefore, additional equations describing the thermal non-equilibrium have not been included yet. Concerning the thermodynamic pressure, the Dalton's law of partial pressures P_i for a mixture of perfect gaseous species is valid:

$$P = \sum_{i=1}^{N_s} P_i \tag{3.8}$$

Moreover, in Re-entry Aerothermodynamics the hypothesis of thermally perfect gas (i.e. non-calorically perfect gas) is generally assumed, so the perfect gas law can be used:

$$P_i = \frac{\rho_i \mathcal{R} T}{W_i} \tag{3.9}$$

where $\mathcal{R}$ is the universal gas constant and W_i is the molecular weight of each species. Under this hypothesis, the thermodynamic properties of each species depend on temperature only. Actually, equations (3.1), (3.2) and (3.3) are specialized for a reacting gas in *chemical non-equilibrium*, for which there is no enough time for its chemical composition to reach the equilibrium conditions; as a result, a *relaxation time* can be observed, during which the gas composition changes with time too [2]. Hence, for such a flow, the thermodynamic properties are function of temperature and mass fractions [2]:

$$h = h(T, Y_i) \tag{3.10}$$

$$e = e(T, Y_i) \tag{3.11}$$

$$c_p = c_p(T, Y_i) \tag{3.12}$$

$$c_v = c_v(T, Y_i) \tag{3.13}$$

where the mass fractions are function of temperature, pressure and history of the flow:

$$Y_i = Y_i(T, p, t) \tag{3.14}$$

Considering the multi-species nature of a chemical non-equilibrium flow, a global continuity equation is not sufficient and this is the reason why the mass conservation equation (3.1) has been specified for each chemical species. Moreover, the mass diffusion mechanism related to a viscous flow has to be taken into account too. In fact, according to the kinetic theory, while in an inviscid flow all the species move at the mixture velocity $\mathbf{u}$, in a viscous flow the diffusion velocity $\mathbf{V}_i$ of species i has to be considered [1]. Hence, the species diffusion flux can be defined as:

$$\mathbf{J}_i = \rho_i \mathbf{V}_i \tag{3.15}$$

In particular, the global continuity equation (as well as the momentum equations) is purely mechanic in nature [1], therefore it is not influenced by chemical reactions. In other words, the total mass cannot diffuse and the following condition has to be satisfied [2]:

$$\sum_{i=1}^{N_s} \mathbf{J}_i = \sum_{i=1}^{N_s} \rho_i \mathbf{V}_i = 0 \tag{3.16}$$

Finally, a compact form for the system of equations can be adopted:

$$\frac{\partial \mathbf{U}}{\partial t} + \nabla \cdot \mathbf{F}^c = \nabla \cdot \mathbf{F}^d + \mathbf{S} \tag{3.17}$$

where:

$$\mathbf{U} = \begin{pmatrix} \rho_i \\ \rho \mathbf{u} \\ \rho E \end{pmatrix}, \quad \mathbf{F}^c = \begin{pmatrix} \rho_i \mathbf{u} \\ \rho \mathbf{u}\mathbf{u} + P\mathbf{I} \\ \rho \mathbf{u} H \end{pmatrix}, \quad \mathbf{F}^d = \begin{pmatrix} -\mathbf{J}_i \\ \boldsymbol{\tau} \\ \boldsymbol{\tau} \cdot \mathbf{u} - \mathbf{q} \end{pmatrix}, \quad \mathbf{S} = \begin{pmatrix} \dot{\omega}_i \\ 0 \\ \dot{\omega}_T \end{pmatrix} \tag{3.18}$$

These are respectively the vectors of conservative variables, convective fluxes, diffusive fluxes and source terms.

The system (3.17) expresses the balance of mass, momentum and energy, but it requires knowledge of thermodynamic and transport properties, as well as chemical kinetics. Within ARGO, the evaluation of physico-chemical properties can be realized through a coupling with the VKI external library MUTATION++[2]. When used as a stand-alone program, MUTATION++ is only able to perform equilibrium computations: taking as inputs a list of species, a range of pressure, temperature and an elemental composition, it applies the minimization of the Gibbs free energy of the mixture [57], returning the equilibrium composition of the mixture as well as its thermodynamic and transport properties. However, the full power of MUTATION++ is in the ability to compute non-equilibrium conditions when it is used as a routine within a CFD code, like ARGO, in order to read a fluid velocity field and take full advantage of both of them. In particular, when MUTATION++ is interrogated through a calling routine, an additional system of differential equations is solved, after reading the *reaction mechanisms*.

Thermodynamic properties

The thermodynamic data of the chemical species can be evaluated with the NASA polynomial database. These 7- or 9-coefficient polynomials provide a fitting of the enthalpy, the specific heats and the entropy of each species as function of temperature. Then, the mixture enthalpy is computed by MUTATION++ as a linear combination of the species enthalpy [42]:

$$h = \sum_{i=1}^{N_s} Y_i h_i \tag{3.19}$$

---

[2] MUTATION++ stands for MUlticomponent Thermodynamic And Transport properties for IONized plasmas in C++.

The species enthalpy can be splitted in a sensible term and a chemical one:

$$h_i = \int_{T_0}^{T} c_{pi}\ \mathrm{d}t + h^0_{f,i} \tag{3.20}$$

where $h^0_{f,i}$ is the formation enthalpy at a reference temperature T_0. This allows to define in equation (3.3) the energy contribution related to the chemical source term:

$$\dot{\omega}_T = -\sum_{i=1}^{N_s} \dot{\omega}_i h^0_{f,i} \tag{3.21}$$

Transport properties

In high-temperature and chemically reacting viscous flows, dynamic viscosity μ and thermal conductivity λ are further unknowns. Moreover, the diffusion mechanism strongly affects both mass diffusion and energy transport. MUTATION++ is able to accurately compute transport properties and coefficients by means of kinetic theory and, specifically, solving collision integrals derived from the Chapman-Enskog solution of the Boltzmann equation [11], [57]. As regards mass diffusion, the species diffusion flux can be written as [11]:

$$\mathbf{J}_i = -\rho D_{i,m}\frac{W_i}{W}\nabla X_i + \rho Y_i \sum_{k=1}^{N_s} D_{k,m}\frac{W_k}{W}\nabla X_k \tag{3.22}$$

where $D_{i,m}$ is the *multi-component diffusion coefficient*, defined as follows:

$$D_{i,m} = \frac{1 - Y_i}{\sum_{j\neq i}\frac{X_j}{D_{ij}}} \tag{3.23}$$

whilst D_{ij} is *the binary diffusion coefficient*, related to the diffusion of the species i into j [2]. X_j denotes the mole fraction of the species j. MUTATION++ is able to compute $D_{i,m}$ in a rigorous way, but within ARGO other simplified diffusion models have been implemented: a constant diffusivity model $D_{i,m} = D$, a constant Lewis number model:

$$D_{i,m} = D = \frac{\lambda}{\mathrm{Le}\ \rho\ c_p^{\mathrm{Frozen}}} \tag{3.24}$$

and a constant Schmidt number model:

$$D_{i,m} = D = \frac{\mu}{\mathrm{Sc}\ \rho} \tag{3.25}$$

In a viscous flow, the energy transport is operated by thermal conduction (Fourier's law):

$$\mathbf{q}_c = -\lambda\nabla T \tag{3.26}$$

For a chemically reacting gas, an additional flux of energy due to the diffusion of each chemical species has to be taken into account, therefore the total heat flux vector is given by:

$$\mathbf{q} = \mathbf{q}_c + \mathbf{q}_d = -\lambda\nabla T + \rho\sum_{i=1}^{N_s} h_i Y_i \mathbf{V}_i \tag{3.27}$$

where λ is the mixture conductivity, h_i is the species enthalpy and Y_i is the species mass fraction. The first term is related to the thermal conduction, while the latter is the energy transport due to the diffusion of each chemical species. Moreover, both radiative contribution and Dufour effect due to mass concentration gradients are neglected here.

Chemical Kinetics

A chemical kinetic model is required for the computation of the chemical reaction rates, in order to evaluate the production terms appearing in the system of governing equations. In general, a flow characterized by reaction rate constants equal to zero (infinitely long relaxation time) is defined as a *frozen flow*. A flow where the reaction rates tend to infinity (relaxation time equal to zero) is an *equilibrium flow* [2]. Finally, a *non-equilibrium flow* is characterized by a finite-rate chemistry.

At equilibrium, the following relation is valid [2]:

$$\sum_{i=1}^{N_s} \nu_i A_i = 0 \tag{3.28}$$

where ν_i is the stoichiometric mole number associated with species A_i. Any chemical reaction is described by an *equilibrium constant*, that is a function of temperature and it is defined as:

$$K_P(T) = \prod_{i=1}^{N_s} P_i^{\nu_i} \tag{3.29}$$

For chemical non-equilibrium flows, like the ones solved by ARGO, the chemical composition does not have enough time before collisions adjust it to the equilibrium composition [2], therefore the production rates for species due to elementary chemical reactions have to be computed. For a generic but elementary chemical reaction, the non-equilibrium condition thus can be described as [11], [2]:

$$\sum_{i=1}^{N_s} \nu'_{i,k} A_{i,k} \iff \sum_{i=1}^{N_s} \nu''_{i,k} A_{i,k} \tag{3.30}$$

where the exponent $'$ and $''$ indicates respectively reactants and products. Hence, considering N_r reactions, the production rate related to each species can be written as:

$$\dot{\omega}_i = W_i \sum_{k=1}^{N_r} (\nu''_{i,k} - \nu'_{i,k}) \left(k_{f,k} \prod_{j=1}^{N_s} \tilde{\rho}_j^{\nu'_{j,k}} - k_{b,k} \prod_{j=1}^{N_s} \tilde{\rho}_j^{\nu''_{j,k}} \right) \tag{3.31}$$

where $\tilde{\rho}$ is the molar density, while $k_{f,k}$ and $k_{b,k}$ are respectively the forward and backward (or reverse) reaction rates. They can be measured experimentally and a general way to express them mathematically is by means of an *Arrhenius law*:

$$k_{f,k}(T) = A_k T^{n_k} \exp\left(\frac{-E_{a_k}}{\mathcal{R}T}\right) \tag{3.32}$$

where, A_k is the pre-exponential factor, n_k is the temperature exponent and E_{a_k} is the activation energy. The backward reaction rate can be computed through the relation with the equilibrium constant:

$$k_{b,k}(T) = \frac{k_{f,k}(T)}{K_{P,k}(T)} \tag{3.33}$$

Equation (3.31) describes the net time rate of change of the concentration of the species [2] and, in ARGO, the production terms related to homogeneous reactions are computed by means of MUTATION++. The source terms linked to heterogeneous reactions requires instead a different treatment, that will be explained in the following sections, in which the discussion will progress explaining how, in the *Unified Approach*, the flow is coupled with the reactive porous material.

3.1.2 Reactive porous media: the volume averaging theory

Within ARGO platform, the simulation of ablation is allowed through a strong coupled approach, in which both the flow and the material response are solved within the same domain of computation. Here, the ablative material is treated as a porous medium, therefore the physical problem turns into the resolution of a multiphase system. Hence, the method of volume averaging is applied to derive continuum Navier-Stokes equations for multiphase systems, so that equations are locally averaged in volume, i.e. they are spatially smoothed in order to be valid everywhere [58]. This continuum approach thus allows to describe the macroscopic behaviour of the physical phenomena [11], [59].

In this approach, two-phase system is considered: a fluid phase (denoted with subscript g) and a solid one (denoted with subscript s). Equations describing each phase are averaged over a Representative Elementary Volume (REV), which is assumed to be much larger than the characteristic size of the pores but much smaller than the domain [59]. The result is that the volume averaged quantities are continuous in space [11] and the macroscopic behaviour is modeled.

An averaging volume $\mathrm{d}V$ can be defined considering the presence of two different phases (Figure 3.2):

$$\mathrm{d}V = \mathrm{d}V_g + \mathrm{d}V_s \tag{3.34}$$

It is now possible to define the volume fractions:

$$\epsilon_g = \frac{\mathrm{d}V_g}{\mathrm{d}V}, \qquad \epsilon_s = 1 - \epsilon_g = \frac{\mathrm{d}V_s}{\mathrm{d}V} \tag{3.35}$$

where ϵ_g is known as *porosity* and describes the void fraction, while ϵ_s is the solid volume fraction. The superficial average of a quantity α on a generic phase γ is defined as [11]:

$$\langle \alpha \rangle = \frac{1}{\mathrm{d}V} \int_{\mathrm{d}V_\gamma} \alpha \ \mathrm{d}V \tag{3.36}$$

while, the intrisic average is:

$$\langle \alpha \rangle_\gamma = \frac{1}{\mathrm{d}V_\gamma} \int_{\mathrm{d}V_\gamma} \alpha \ \mathrm{d}V \tag{3.37}$$

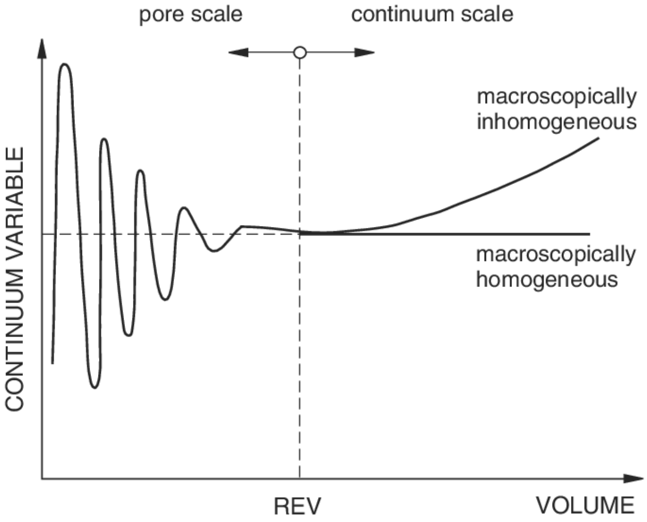

Figure 3.1: Definition of a Representative Elementary Volume. Image taken from [60].

A relation between the two averages exists:

$$\langle \alpha \rangle = \epsilon_\gamma \langle \alpha \rangle_\gamma \tag{3.38}$$

The volume averaging theory can be applied to equations (3.1), (3.2) and (3.3), in order to obtain the Volume Averaged Navier-Stokes equations (VANS), written in terms of volume fractions. The full derivation of VANS for a non-charring material can be found in [11] and they will be now presented and briefly discussed.

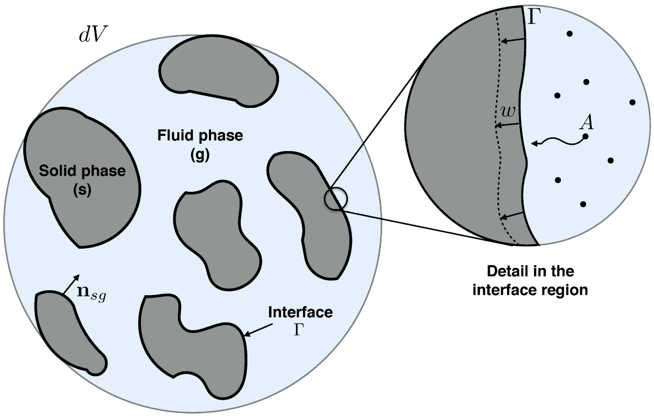

Figure 3.2: The physical problem is modeled as a two-phase system. Image from [11].

Gaseous species mass conservation equation

$$\frac{\partial}{\partial t}(\epsilon_g \langle \rho_i \rangle_g) + \nabla \cdot (\epsilon_g \langle \rho_i \rangle_g \langle \mathbf{u} \rangle_g) = -\nabla \cdot \langle \mathbf{J}_i \rangle + \epsilon_g \langle \dot{\omega}_i^{\mathrm{hom}} \rangle_g + \langle \dot{\omega}_i^{\mathrm{het}} \rangle \tag{3.39}$$

The averaged species diffusion flux vector $\langle \mathbf{J}_i \rangle$ is given by:

$$\langle \mathbf{J}_i \rangle = -\epsilon_g \langle \rho_i \rangle_g \frac{D_{i,m}}{\eta} \frac{W_i}{W} \nabla X_i + \epsilon_g \langle \rho_i \rangle_g \sum_{k=1}^{N_s} \frac{D_{k,m}}{\eta} \frac{W_k}{W} \nabla X_k \tag{3.40}$$

In particular, an effective diffusion coefficient has been defined to take into account the tortuosity η of the material:

$$D_{\text{eff}} = \frac{\epsilon_g}{\eta} D_{i,m} \tag{3.41}$$

The tortuosity is a porous medium property which expresses the ratio between the trajectory of a particle and a straight line. It is strictly dependent on the porosity ϵ_g and a linear interpolation can be used to describe its evolution between the freestream value ($\eta = 1$) and the bulk one [13], [47]:

$$\eta = \frac{\eta_0}{1 - \epsilon_{g,0}} (\epsilon_g - 1) + 1 \tag{3.42}$$

Finally, the averaged source term due to homogeneous reactions is computed as follows:

$$\begin{aligned} \langle \dot{\omega}_i^{\text{hom}} \rangle = \epsilon_g \langle \dot{\omega}_i^{\text{hom}} \rangle_g = & W_i \sum_{k=1}^{N_r} (\nu''_{i,k} - \nu'_{i,k}) \left(k_{f,k} \prod_{j=1}^{N_s} \frac{1}{\mathrm{d}V_g} \int_{\mathrm{d}V_g} \left(\frac{\langle \rho_j \rangle_g}{W_j} \right)^{\nu'_{j,k}} \mathrm{d}v + \right. \\ & \left. - k_{b,k} \prod_{j=1}^{N_s} \frac{1}{\mathrm{d}V_g} \int_{\mathrm{d}V_g} \left(\frac{\langle \rho_j \rangle_g}{W_j} \right)^{\nu''_{j,k}} \mathrm{d}v \right) \end{aligned} \tag{3.43}$$

Solid mass conservation equation and recession model

$$\frac{\partial \langle \rho_s \rangle}{\partial t} + \nabla \cdot \langle \rho_s \mathbf{u}_s \rangle = -\langle \dot{\omega}^{\text{het}} \rangle \tag{3.44}$$

where $\mathbf{u_s}$ is the solid velocity. Schrooyen [11] treats the solid matrix as stationary and non-elastic, so the convective term is equal to zero. Moreover, considering that $\langle \rho_s \rangle = \epsilon_s \langle \rho_s \rangle_s$, equation (3.44) can be written as:

$$\frac{\partial}{\partial t} (\epsilon_s \langle \rho_s \rangle_s) = -\langle \dot{\omega}^{\text{het}} \rangle \tag{3.45}$$

where $\langle \dot{\omega}^{\text{het}} \rangle$ is the averaged global production term due to heterogeneous reactions; it represents the amount of mass lost by the solid matrix and it has to be equal to the mass gained by the gaseous phase, in order to ensure the mass conservation. This source term can be modeled assuming an irreversible first order reaction. It is given by:

$$\langle \dot{\omega}^{\text{het}} \rangle = \sum_{i=1}^{N_s} \langle \dot{\omega}_i^{\text{het}} \rangle = \frac{1}{\mathrm{d}V} \oint_{\partial \Omega_g} -k_f \langle \rho_A \rangle_{gs} \, \mathrm{d}S = -S_f k_f \langle \rho_A \rangle_g \tag{3.46}$$

where S_f is the specific (volumetric) surface of the carbon fibers, k_f is the forward reaction rate, while $\langle \rho_A \rangle_{gs}$ is the area averaged density on the surface of the solid phase [11].

Furthermore, the intrinsic solid density of the fibers is considered as a constant, so that the solid volume fraction ϵ_s can be computed as:

$$\epsilon_s = \frac{\langle \rho_s \rangle}{\langle \rho_s \rangle_s} \tag{3.47}$$

Therefore, equation (3.45) is solved to track the change in porosity [42]. As regards ablation, a cylindrical model for the carbon fibers has been implemented within ARGO and recession is assumed to be uniform and radial, as sketched in Figure 3.3. Hence, the solid volume fraction is given by:

$$\epsilon_s = \frac{N_f \pi r^2 L_f}{\mathrm{d}V} \tag{3.48}$$

where N_f is the number of cylindrical carbon fibers, r is the radius and L_f is the length. The variables ϵ_s and r thus can be related to the initial decomposition state:

$$\frac{r_0^2}{\epsilon_{s,0}} = \frac{r^2}{\epsilon_s} \tag{3.49}$$

This allows to compute the specific surface as:

$$S_f = \frac{N_f 2\pi r L_f \epsilon_s}{N_f \pi r^2 L_f} = \frac{2}{r_0}\sqrt{\epsilon_{s,0}\epsilon_s} \tag{3.50}$$

Therefore, tracking the change in solid volume fraction ϵ_s, the recession of the fibers can be directly computed through a geometrical procedure.

Momentum conservation equation

$$\frac{\partial}{\partial t}\langle \rho \mathbf{u} \rangle_g + \nabla \cdot (\langle \rho \rangle_g \langle \mathbf{u} \rangle_g \langle \mathbf{u} \rangle_g + P) = \nabla \cdot \langle \boldsymbol{\tau} \rangle_g + \mathbf{F_{gs}} \tag{3.51}$$

where $\mathbf{F_{gs}}$ is drag force imposed by the presence of the solid phase in the porous medium [11]. It can be modeled as follows [11], [58]:

$$\mathbf{F_{gs}} = \frac{\mu}{\kappa}\epsilon_g^2 \langle \mathbf{u}_g \rangle \tag{3.52}$$

where κ is the permeability, a medium property related to the microstructure of the material. In ARGO, it is evaluated by means of the semi-empirical model of Carman-Kozeny:

$$\kappa^{-1} = \frac{S_{f,0}^2 (1-\epsilon_g)^2 k_k}{\epsilon_g^3} \tag{3.53}$$

where $S_{f,0}$ is the initial specific surface, while k_k is a constant of proportionality that relates κ with the tortuosity.

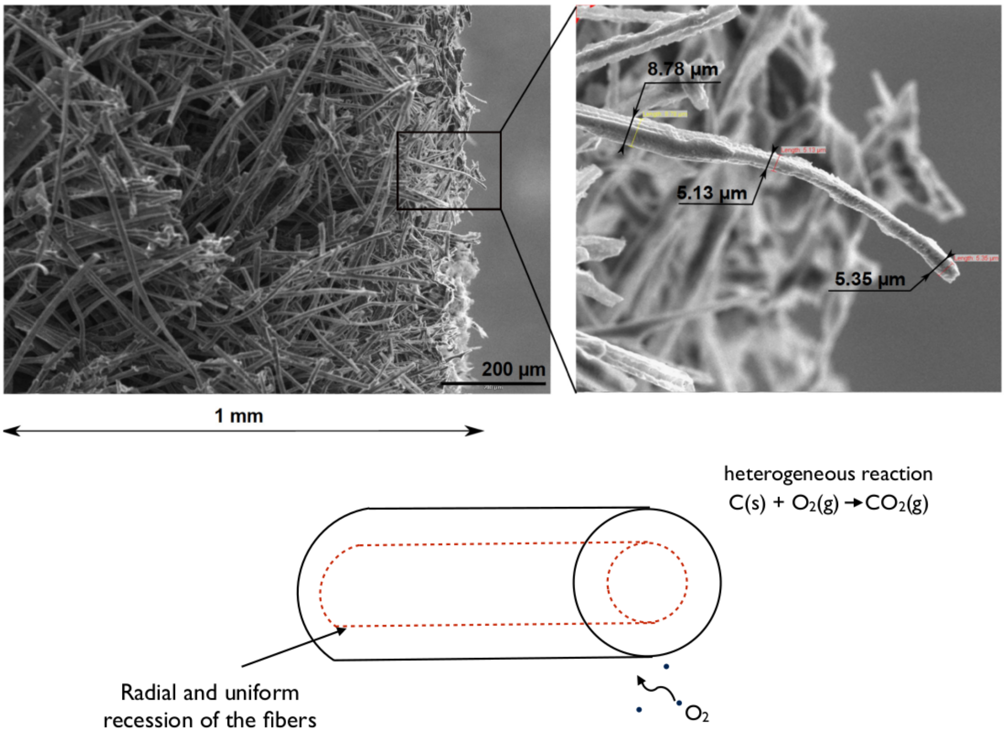

Figure 3.3: Recession model implemented within Argo. Carbon fibers are considered as cylindrical and the recession is assumed to be uniform and radial. Credits: [11].

Energy conservation equation

Only one energy equation is solved, with the assumption of thermal equilibrium between the solid matrix and the gaseous phase. This is the most usual hypothesis in the material response codes when the Peclet number for the heat transfer in the pores is small [11]. The averaged energy balance is given by:

$$\begin{aligned}\frac{\partial}{\partial t}(\langle \rho E_{\text{tot}} \rangle) + \nabla \cdot \left(\epsilon_g \langle \rho \rangle_g \langle H \rangle_g \langle \mathbf{u} \rangle_g\right) =& \nabla \cdot \left(\langle \boldsymbol{\tau} \cdot \mathbf{u} \rangle + \lambda_{\text{eff}} \nabla \langle T \rangle - \sum_{i=1}^{N_s} h_i \langle \mathbf{J}_i \rangle\right) + \\ & - \sum_{i=1}^{N_s} \left(\epsilon_g \langle \dot{\omega}_i^{\text{hom}} \rangle_g + \langle \dot{\omega}_i^{\text{het}} \rangle\right) h_{f,i}^0\end{aligned} \tag{3.54}$$

where λ_{eff} is the effective thermal conductivity defined as:

$$\lambda_{\text{eff}} = \epsilon_s \lambda_s + \epsilon_g \lambda_g \tag{3.55}$$

VANS equations for a non-charring ablator

The system of volume averaged Navier-Stokes equations can be rewritten in the compact form:

$$\frac{\partial \mathbf{U}}{\partial t} + \nabla \cdot \mathbf{F}^c = \nabla \cdot \mathbf{F}^d + \mathbf{S} \tag{3.56}$$

Hence, the vector of conservative variables is:

$$\mathbf{U} = \begin{pmatrix} \epsilon_g \langle \rho_i \rangle_g \\ \langle \rho \mathbf{u} \rangle_g \\ \langle \rho E_{\text{tot}} \rangle \\ \langle \rho_s \rangle \end{pmatrix} \tag{3.57}$$

The convective flux vector is:

$$\mathbf{F}^c = \begin{pmatrix} \epsilon_g \langle \rho_i \rangle_g \langle \mathbf{u} \rangle_g \\ \langle \rho \rangle_g \langle \mathbf{u} \rangle_g \langle \mathbf{u} \rangle_g + P \\ \epsilon_g \langle \rho \rangle_g \langle H \rangle_g \langle \mathbf{u} \rangle_g \\ 0 \end{pmatrix} \tag{3.58}$$

The diffusive flux vector is:

$$\mathbf{F}^d = \begin{pmatrix} -\langle \mathbf{J} \rangle_i \\ \langle \boldsymbol{\tau} \rangle_g \\ \langle \boldsymbol{\tau} \cdot \mathbf{u} \rangle + \lambda_{\text{eff}} \nabla \langle T \rangle - \sum_{i=1}^{N_s} h_i \langle \mathbf{J} \rangle_i \\ 0 \end{pmatrix} \tag{3.59}$$

Finally, the source term vector is:

$$\mathbf{S} = \begin{pmatrix} \epsilon_g \langle \dot{\omega}_i^{\text{hom}} \rangle_g + \langle \dot{\omega}_i^{\text{het}} \rangle \\ \mathbf{F_{gs}} \\ -\sum_{i=1}^{N_s} \left(\epsilon_g \langle \dot{\omega}_i^{\text{hom}} \rangle_g + \langle \dot{\omega}_i^{\text{het}} \rangle \right) h_{f,i}^0 \\ -\sum_{i=1}^{N_s} \langle \dot{\omega}_i^{\text{het}} \rangle \end{pmatrix} \tag{3.60}$$

This is the system of equations originally implemented within the *DGAblation* module of ARGO by Schrooyen [11], in order to predict the behaviour of a non-charring ablator, i.e. a carbon preform TPM. A module accounting for pyrolysis was added by Coheur et al. [13] a few years later, allowing to expand the capabilities of ARGO to treat a porous charring ablator too and, in particular, a carbon-phenolic TPM. The module for pyrolysis will be introduced in the following section, because it represents a step forward towards the modeling of cork-phenolic ablators.

3.2 Extension to cork-phenolic specific phenomena

The thermochemical characterization of cork-based TPMs has already been widely presented in Chapter 2, as well as the available solutions to treat pyrolysis and swelling phenomena. This section thus contains new answers to the problem of modeling cork-phenolic ablators. Specifically, the development of a new feature to compute the pyrolysis gas in ARGO is treated and, finally, an original but preliminary idea to model the swelling behaviour is described.

3.2.1 Model for pyrolysis

The thermal decomposition of charring ablators has already been modeled and implemented within ARGO by Coheur et al. [13]. A scheme of the model is shown in Figure 3.4. The virgin material, a carbon-phenolic TPM, is characterized by a structure of cylindrical carbon fibers filled with a phenolic resin. A new definition for the average solid density is needed, in order to take into account the presence of the two solid components:

$$\langle\rho_s\rangle = \langle\rho_f\rangle + \langle\rho_m\rangle \tag{3.61}$$

where $\langle\rho_f\rangle$ is the average solid density of the fibers, while $\langle\rho_m\rangle$ is the one of the resin matrix. Equation (3.61) can be rewritten in terms of solid volume fractions:

$$\epsilon_s\langle\rho_s\rangle_s = \epsilon_f\langle\rho_f\rangle_f + \epsilon_m\langle\rho_m\rangle_m \tag{3.62}$$

where ϵ_f and ϵ_m are respectively the volume fractions of the fibers and the resin. Hence, the solid mass conservation equation (3.45) turns into:

$$\frac{\partial}{\partial t}\Big(\epsilon_f\langle\rho_f\rangle_f + \epsilon_m\langle\rho_m\rangle_m\Big) = -\langle\dot{\omega}^{\text{het}}\rangle - \langle\dot{\omega}^{\text{pyro}}\rangle \tag{3.63}$$

where $\langle\dot{\omega}^{\text{pyro}}\rangle$ is the source term due to the thermal degradation of the solid material. Moreover the average solid density of the resin matrix can be splitted considering the presence of multiple fictitious solid compounds, in order to express the production rate of pyrolysis through a certain number N_p of pyrolysis reactions [61]:

$$\langle\rho_m\rangle = \sum_{I=A}^{N_p}\langle\rho_I\rangle \tag{3.64}$$

where $\langle\rho_I\rangle$ is the average solid density of the resin compound I. The decomposition rate of the compound I can thus be described by an *Arrhenius law*:

$$\frac{\partial}{\partial t}\langle\rho_I\rangle = -A_{0,I}\langle\rho_I^v\rangle \exp\Big(\frac{-E_{a,I}}{\mathcal{R}T}\Big)\Big(\frac{\langle\rho_I\rangle - \langle\rho_I^c\rangle}{\langle\rho_I^v\rangle}\Big)^{n_I} \tag{3.65}$$

where the virgin and char density of the compound I can be re-defined in terms of a fraction F_I of the average solid matrix:

$$\langle\rho_I^v\rangle = F_I^v\langle\rho_m^v\rangle; \qquad \langle\rho_I^c\rangle = F_I^c\langle\rho_m^c\rangle \tag{3.66}$$

The progress variable ξ_I is defined to describe each pyrolysis reaction, i.e. the local decomposition state of the material:

$$\xi_I = \frac{\langle\rho_I^v\rangle - \langle\rho_I\rangle}{\langle\rho_I^v\rangle - \langle\rho_I^c\rangle}, \qquad \xi = \sum_I F_I^v\xi_I \tag{3.67}$$

The source term $\langle\dot{\omega}^{\text{pyro}}\rangle$ can be computed considering all the pyrolysis reactions of each resin compound:

$$\langle\dot{\omega}^{\text{pyro}}\rangle = \sum_I^{N_p}\langle\dot{\omega}_I^{\text{pyro}}\rangle = \sum_I^{N_p}\frac{\partial}{\partial t}\langle\rho_I\rangle \tag{3.68}$$

Finally, the computation of pyrolysis production rate π_i for each chemical species i is given by:

$$\pi_i = m_{i,I} \, \langle \dot{\omega}_I^{\text{pyro}} \rangle \tag{3.69}$$

where, $m_{i,I}$ is the mass fraction of the spiecies i generated by the thermal decomposition of the compound I [13].

When pyrolysis occurs, a carbonaceous residue is left, so a model of char surrounding the cylindrical carbon fibers has been implemented [13], as shown in Figure 3.4. This model requires the definition of an equivalent radius:

$$r_e = r_{f,0} + e_c = r_{f,0}\sqrt{\frac{\epsilon_s}{\epsilon_{f,0}}} \tag{3.70}$$

where $r_{f,0}$ is the initial radius of the fibers, whilst e_c is the additional thickness due to the formation of the char; it simply depends on the amount of carbonaceous residue that one decides to leave after pyrolysis. This allows to re-define the specific surface as:

$$S_f = \frac{2}{r_{f,0}}\sqrt{\epsilon_{f,0}\epsilon_s} \tag{3.71}$$

Therefore, the oxidation of the carbon fibers takes place only once the char has been totally removed.

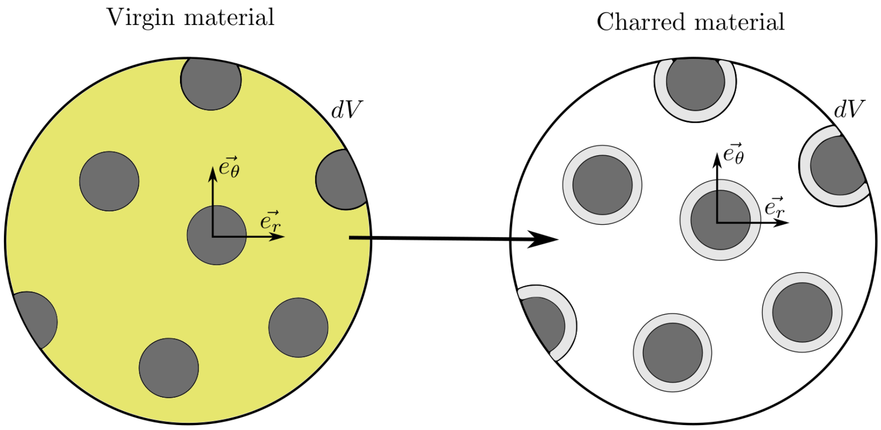

Figure 3.4: Model for pyrolysis implemented within Argo, in order to treat carbon-phenolic ablators. Figure taken from [13].

The system of VANS equation can be rewritten to include pyrolysis phenomenon:

$$\frac{\partial \mathbf{U}}{\partial t} + \nabla \cdot \mathbf{F}^c = \nabla \cdot \mathbf{F}^d + \mathbf{S} \tag{3.72}$$

Hence, the vector of conservative variables is:

$$\mathbf{U} = \begin{pmatrix} \epsilon_g \langle \rho_i \rangle_g \\ \langle \rho \mathbf{u} \rangle_g \\ \langle \rho E_{\text{tot}} \rangle \\ \langle \rho_f \rangle + \sum_{I=1}^{N_p} \langle \rho_I \rangle \end{pmatrix} \tag{3.73}$$

The convective flux vector is:

$$\mathbf{F}^c = \begin{pmatrix} \epsilon_g \langle\rho_i\rangle_g \langle\mathbf{u}\rangle_g \\ \langle\rho\rangle_g \langle\mathbf{u}\rangle_g \langle\mathbf{u}\rangle_g + P \\ \epsilon_g \langle\rho\rangle_g \langle H\rangle_g \langle\mathbf{u}\rangle_g \\ 0 \end{pmatrix} \tag{3.74}$$

The diffusive flux vector is:

$$\mathbf{F}^d = \begin{pmatrix} -\langle\mathbf{J}\rangle_i \\ \langle\boldsymbol{\tau}\rangle_g \\ \langle\boldsymbol{\tau}\cdot\mathbf{u}\rangle + \lambda_{\text{eff}}\nabla\langle T\rangle - \sum_{i=1}^{N_s} h_i \langle\mathbf{J}\rangle_i \\ 0 \end{pmatrix} \tag{3.75}$$

Finally, the source term vector is:

$$\mathbf{S} = \begin{pmatrix} \epsilon_g \langle\dot\omega_i^{\text{hom}}\rangle_g + \langle\dot\omega_i^{\text{het}}\rangle + \sum_{I=1}^{N_p} m_{i,I} \langle\dot\omega_I^{\text{pyro}}\rangle \\ \mathbf{F_{gs}} \\ -\sum_{i=1}^{N_s} \left(\epsilon_g \langle\dot\omega_i^{\text{hom}}\rangle_g + \langle\dot\omega_i^{\text{het}}\rangle + \sum_{I=1}^{N_p} m_{i,I} \langle\dot\omega_I^{\text{pyro}}\rangle\right) h_{f,i}^0 \\ -\sum_{i=1}^{N_s} \langle\dot\omega_i^{\text{het}}\rangle - \sum_{I=1}^{N_p} m_{i,I} \langle\dot\omega_I^{\text{pyro}}\rangle \end{pmatrix} \tag{3.76}$$

The implementation of these equations made ARGO capable of simulating the ablation of a charring carbon-phenolic TPM.

Concerning the treatment of cork-phenolic ablators such as the Cork P50, it should be emphasised that a further development is required because, when subjected to heat, the P50 undergoes thermal degradation of both cork and phenolic resin. This process leads to the formation of carbon fibers (not present in the virgin material) and the carbonaceous residue. Ideally, the physical model should be modified in order to define a *multi-char model*, capable of taking into account the carbon fibers, a first char due to the degradation of the cork and a second char due to the decomposition of the phenolic resin. Considering the complexity of distinguishing the different degradation processes, another possibility is to treat the virgin material as made up of a single charring constituent (single-char model). The two models are sketched in Figure 3.5. In practice, the implementation of one of these two models requires a considerable effort and it is beyond the scope of this work. For this reason, the main contribution to pyrolysis modeling of this work consists in the improvement of the current model which well describes the structure of a carbon-phenolic TPM and, in particular, in the definition of an accurate method to compute the pyrolysis production rate.

The chemical composition of pyrolysis gas has been treated as known and constant so far. Considering equation (3.69):

$$\pi_i = m_{i,I}\ \langle\dot\omega_I^{\text{pyro}}\rangle \tag{3.77}$$

the mass fractions $m_{i,I}$ are unknown and they should be determined from experimental data, since they are not available in literature [13]. To date, the species mass fractions $m_{i,I}$ were pre-fixed and hard-coded within the input file of ARGO. As already discussed

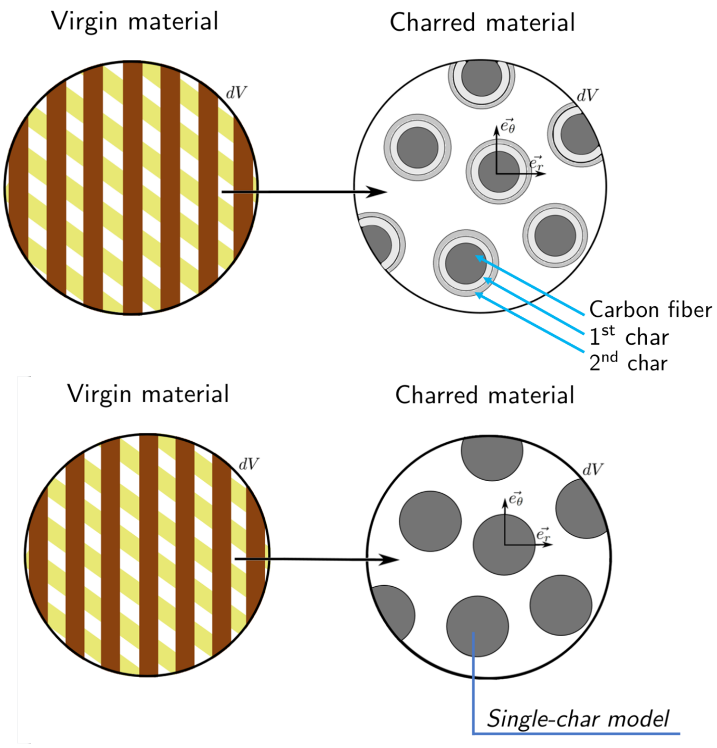

Figure 3.5: Ideas for modeling of pyrolysis in cork-phenolic ablators. The virgin material could be treated as a homogeneous medium. The charred material could be modeled through a multi-char model (top) or a single-char one (bottom). Figure modified from [13].

in Section 2.1.1, this is a strong assumption, as the composition of pyrolysis gas actually is not constant and it is a function of the local thermodynamic conditions and of the elemental composition too. However, the computation of $m_{i,I}$ requires to specify the conditions in which the pyrolysis gas is generated and they are not known a priori. Nevertheless, a reasonable hypothesis is to impose the production of pyrolysis gases at thermochemical equilibrium. This is a very common assumption in literature, since the pyrolysis gas flows at relatively low speeds inside the porous medium [17]. Moreover, while a material response code is not able to describe the evolution of the gas, the *Unified Approach* allows the pyrolysis gas to react with the sorrounding gases (if the proper reaction mechanisms are included) once it has been generated at equilibrium, because ARGO actually solves the governing equations of fluid dynamics.

Therefore, a new routine calling MUTATION++ has been implemented within ARGO. It provides to MUTATION++ the local temperature and pressure so that, starting from the elemental composition of pyrolysis gases, MUTATION++ is able to compute the species mass fractions $m_{i,I}$ at the local thermochemical equilibrium (Figure 3.6). Hence, through the minimization of the Gibbs free energy of the mixture [57], MUTATION++ applies the elemental mass conservation. In this way, the composition of the mixture depends on temperature, pressure and elemental composition [11]:

$$Y_i = Y_i(T, P, \mathcal{X}_j) \tag{3.78}$$

where $\mathcal{X}_j$ is the elemental mass fraction, $j = 1, ..., N_e$ and N_e is the number of chemical elements.

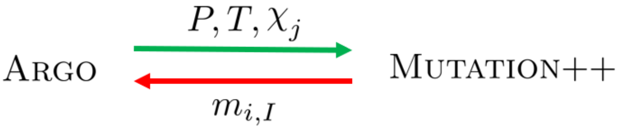

Figure 3.6: Scheme of the new routine for the computation of pyrolysis production rate.

This procedure shifts the problem towards the evaluation of the elemental composition $\mathcal{X}_j$ of pyrolysis gases. The best choice is to perform targeted analyses but, due to the unavailability of experimental data, Başkaya [20] proposed a simplified strategy to estimate $\mathcal{X}_j$ for the Cork P50, starting from the measurements of Sakraker [7] and collecting data related to the chemical composition of cork from literature. In this work the same approach is adopted, using more recent data.

The elemental composition of the virgin P50 can be computed by means of a weighted average and considering a mass ratio between resin and cork of 1:4 [7]. Furthermore, several compounds can be identified inside cork, as shown in Figure 3.7. Data are taken from the literature [20], [62] and outlined in Table 3.2.

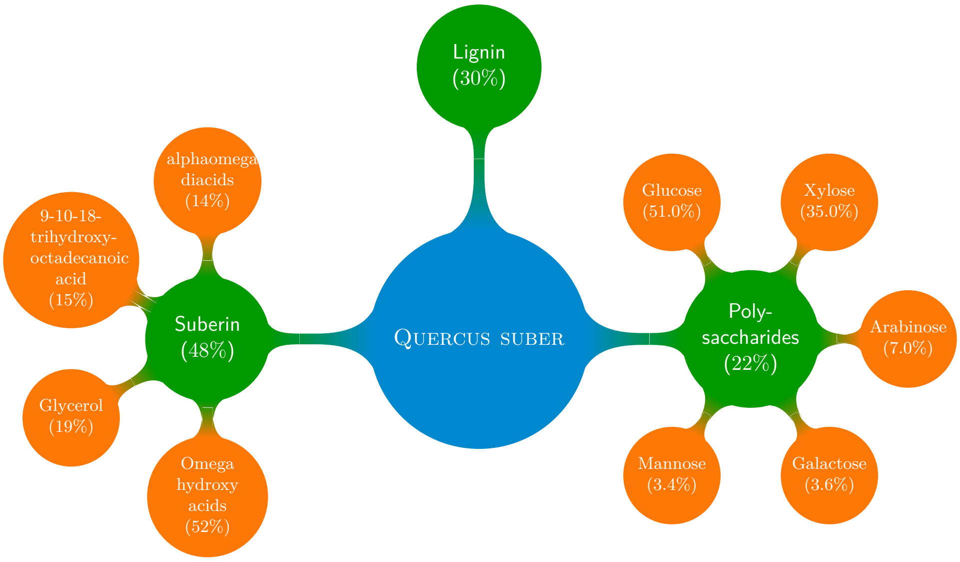

Figure 3.7: Cork composition. Data from literature [20], [62].

Figure 3.8 shows a section of a P50 sample tested in VKI Plasmatron. Sakraker [7] measured the length of the sample and provided the thickness of each layer along the

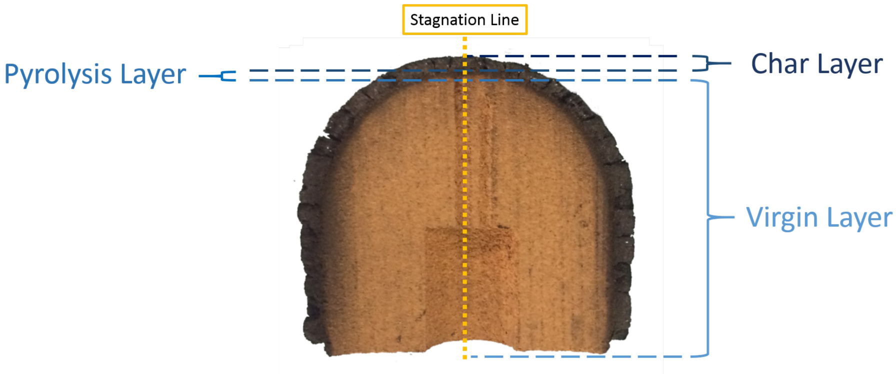

Figure 3.8: Section of a P50 sample tested in VKI Plasmatron by Sakraker [7]. Figure taken from [20].

stagnation line, as well as its mass and radius (initial and final values). Moreover, the virgin and char density have been measured through TGA analysis ($\rho_v \approx 470$ kg/m^3, $\rho_c \approx 280$ kg/m^3). Assuming as a constant the thickness of the layers, it is possible to easily compute their volume and the mass values. Then, the residual mass fraction of each element (C:H:O) after the heat treatment can be computed as follows:

$$Y_{\text{res}\,(i)} = \Big(\frac{m_{\text{char}}}{m_{\text{res}}}\Big) Y_{\text{char}\,(i)} + \Big(\frac{m_{\text{pyro}}}{m_{\text{res}}}\Big)\Big(\frac{Y_{\text{char}\,(i)} + Y_{\text{virgin}\,(i)}}{2}\Big) + \Big(\frac{m_{\text{virgin}}}{m_{\text{res}}}\Big) Y_{\text{virgin}\,(i)} \tag{3.79}$$

where $Y_{\text{virgin}} \equiv Y_0$, while $Y_{\text{char}\,(\text{C})} = 1$. Hence:

$$Y_{\text{pyro}\,(i)} = \Big(\frac{m_0}{m_{\text{lost}}}\Big) Y_{0\,(i)} - \Big(\frac{m_{\text{res}}}{m_{\text{lost}}}\Big) Y_{\text{res}\,(i)} \tag{3.80}$$

The test 21 performed by Sakraker [7] has been taken as a reference, so this procedure allowed to assess the elemental composition of pyrolysis gases shown in Table 3.1. It is a only a first approximation for $\mathcal{X}_j$, but it will be used in the simulations of charring ablators to test the new routine of ARGO for the computation of pyrolysis gas composition.

Table 3.1: Elemental composition of pyrolysis gases, for Cork P50.

	C	H	O
Mass fraction	0.0872	0.1937	0.7192
Mole fraction	0.0297	0.7864	0.1839

	Compound	Chemical formula	C	H	O
	Omega-hydroxyacids	$C_{19}H_{37}O_3$	0.7279	0.1190	0.1531
	Glycerol	$C_3H_8O_3$	0.3913	0.0876	0.5212
	9-10-18-trihydroxyoctadecanoic acid	$C_{18}H_{37}O_5$	0.6483	0.1118	0.2399
	Alfa-omega-diacids	$C_{18}H_{37}O_5$	0.6831	0.1146	0.2022
Suberin			0.6458	0.1113	0.2429
Lignin [13]			0.5730	0.0630	0.3640
	Glucose	$C_6H_{12}O_6$	0.4000	0.0671	0.5328
	Xylose	$C_5H_{10}O_5$	0.4000	0.0671	0.5328
	Arabinose	$C_5H_{10}O_5$	0.4000	0.0671	0.5328
	Galactose	$C_6H_{12}O_6$	0.4000	0.0671	0.5328
	Mannose	$C_6H_{12}O_6$	0.4000	0.0671	0.5328
Polysaccharides			0.4000	0.0671	0.5328
Quercus suber			0.5675	0.0869	0.3456
Phenolic resin		C_6H_5OH	0.7657	0.0643	0.1700
Virgin P50			0.6171	0.0812	0.3017

Table 3.2: Mass fraction of Cork P50 compounds. Data from literature [20], [62].

3.2.2 Model for swelling

The research of a physical model capable of predicting the swelling behaviour drives this part of the work. Three different models for swelling materials have been presented in Section 2.2.1, but the method investigated here should have certain features which make it suitable for the implementation in ARGO, as a future task. Firstly, it should be based on a continuum approach, in order to be representable through equations valid over the whole domain of computation. This would allow to not upset the current model and to easily apply the method of volume averaging to write the equations in terms of porosity. Moreover, the new model should also be compatible with the numerical method (DGM) used in ARGO to solve the system of governing equations. For instance, the approach investigated by Kuborn et al. [52] is probably the most complete but it involves the theory of elasticity to derive the swelling velocity from the displacement field, therefore it requires a multi-physics coupling with a structural mechanics solver. The method proposed by Anderson et al. [51], [53] is very promising but the semi-empirical equation modeling the swelling velocity should be integrated over the domain and solved using the DG method, which would make the implementation very complex. Finally, the approach of Zhang et al. [55] is interesting too, but it requires two different energy conservation equations for the material, while a single equation model is adopted in ARGO.

A simplified strategy is now devised, based on an *a priori assumption on the velocity profile*. The starting point is the mass conservation equation for the solid phase:

$$\frac{\partial \langle \rho_s \rangle}{\partial t} + \nabla \cdot \langle \rho_s \mathbf{u}_s \rangle = -\langle \dot{\omega}^{\text{het}} \rangle - \langle \dot{\omega}^{\text{pyro}} \rangle \tag{3.81}$$

where $\langle \rho_s \rangle$ is the average density of the solid phase, connected to the intrinsic density $\langle \rho_s \rangle_s$ through the solid volume fraction ϵ_s:

$$\langle \rho_s \rangle = \epsilon_s \langle \rho_s \rangle_s \tag{3.82}$$

In the current model of ARGO, the solid matrix is treated as rigid and stationary, so that the convective term is equal to zero. Actually, a velocity for the solid phase must be now defined in order to treat the swelling mechanism. For this reason, the chemical production terms can be neglected, in order to focus on the convective transport mechanism, which is what actually needs to be modeled:

$$\frac{\partial \langle \rho_s \rangle}{\partial t} + \underbrace{\nabla \cdot \langle \rho_s \mathbf{u}_s \rangle}_{\text{Convective term}} = 0 \tag{3.83}$$

The solid velocity $\mathbf{u_s}$ is thus the focal point of the model. Therefore, equation (3.83) can be rewritten in terms of a generic variable U:

$$\frac{\partial U}{\partial t} + \nabla \cdot (U \mathbf{u}_s) = 0 \tag{3.84}$$

Equation (3.84) is a pure convection equation describing the transport of the generic variable U, operated by a flow moving at the transport velocity $\mathbf{u}_s = (u_s, v_s, w_s)$. Moreover, it is possible to split the divergence of a scalar per a vector in two terms:

$$\nabla \cdot (U \mathbf{u}_s) = U \nabla \cdot \mathbf{u}_s + \mathbf{u}_s \cdot \nabla U \tag{3.85}$$

In explicit form:

$$\frac{\partial U}{\partial t} + U\left(\frac{\partial u_s}{\partial x} + \frac{\partial v_s}{\partial y} + \frac{\partial w_s}{\partial z}\right) + \left(u_s\frac{\partial U}{\partial x} + v_s\frac{\partial U}{\partial y} + w_s\frac{\partial U}{\partial z}\right) = 0 \tag{3.86}$$

For simplicity, the assumption of one dimensional flow in the y-direction is adopted, so that the derivatives along the other directions are equal to zero. Therefore:

$$\frac{\partial U}{\partial t} + U\frac{\partial v_s}{\partial y} + v_s\frac{\partial U}{\partial y} = 0 \tag{3.87}$$

This 1D nonlinear convection equation has been implemented within a MATLAB code using the Finite Difference Method (FDM).

In view of a future implementation within ARGO, the variable U would represent the current average solid density normalized, for instance, with the nominal value:

$$U = \frac{\langle\rho_s\rangle}{[\langle\rho_s\rangle]_n} = \frac{\epsilon_s\langle\rho_s\rangle_s}{[\epsilon_s\langle\rho_s\rangle_s]_n} = \frac{\epsilon_s}{[\epsilon_s]_n} \tag{3.88}$$

The intrinsic density $\langle\rho_s\rangle_s$ is treated as a constant[3], therefore the variable U actually would reflect the solid volume fraction ϵ_s. The boundary conditions are a consequence of the normalization, since U may vary between 0 and 1:

$$\begin{cases} y = 0 & \longrightarrow \quad U(0,t) = 1 \\ y = 2L_i & \longrightarrow \quad U(2L_i,t) = 0 \end{cases} \tag{3.89}$$

Adopting the same philosophy of ARGO, the initial condition has to describe the transition from a pure fluid region to a porous medium, as sketched in Figure 3.9. Furthermore, the interface should be enough smoothed to prevent the formation of a discontinuity. For these reasons, the initial condition can be expressed through a hyperbolic tangent function:

$$t = 0 \quad \longrightarrow \quad U(y,0) = \frac{1}{2}[1 - \tanh{(y - L_i)}] \tag{3.90}$$

where L_i is the initial length of the porous material.

The main point is the modeling of the solid velocity v_s. The simpliest approach could consist in the assumption of a constant value for v_s:

$$v_s(y,t) = \overline{v}_s = \frac{L_f - L_i}{\Delta t} \tag{3.91}$$

where L_f is the final length of the sample at the end of the test in Plasmatron and Δt is the swelling period. Therefore, v_s could be modeled as the mean velocity during the test performed by Sakraker [7]. However, this simple approach does not ensure the solid

---

[3] This assumption, acceptable for a stationary and non-elastic solid, could be no longer valid for a swelling material. A deeper explanation will be provided in the conclusive part of this thesis.

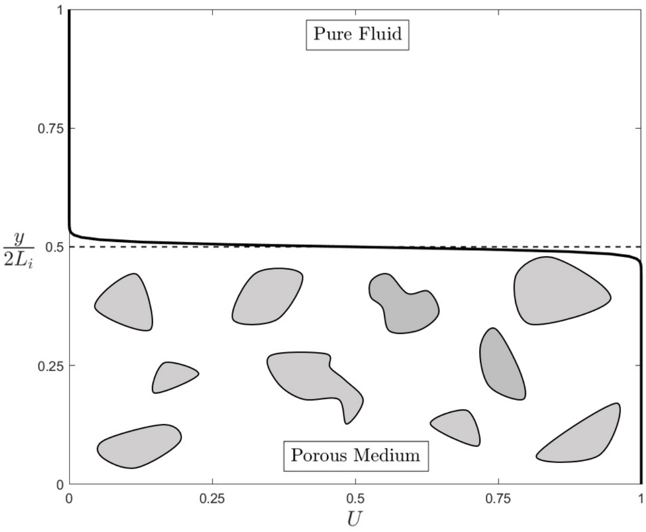

Figure 3.9: Sketch of the initial condition, in analogy with the current model in ARGO.

mass conservation, an issue that has already been highlighted by Martinez [47]. In fact, the general definition of mass is given by:

$$m = \int_{\mathrm{dV}} \rho \; \mathrm{d}V \tag{3.92}$$

Considering that the quantity U stands for $\langle \rho_s \rangle$ (normalized), the corresponding area under the curve represents the solid mass and, as shown in Figure 3.10, it is increasing because of a mass injection from the bottom. This is a direct consequence of a non-zero

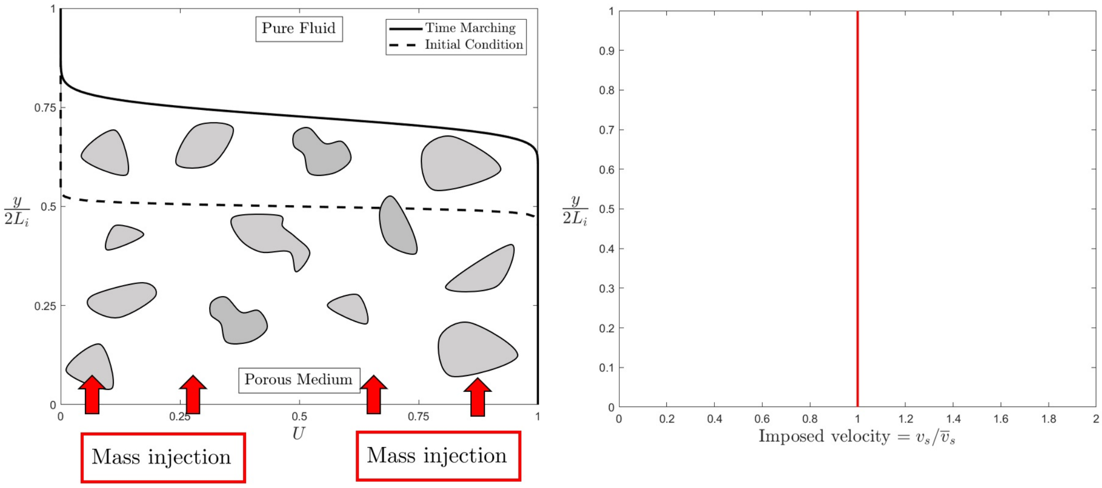

Figure 3.10: Effect of a constant velocity profile on the solid mass conservation.

and, specifically, positive velocity at the boundary. Imposing a constant value for v_s, the velocity gradient is indeed equal to zero everywhere:

$$v_s(y,t) = \overline{v}_s \qquad \Longrightarrow \qquad \frac{\partial v_s}{\partial y} = 0 \tag{3.93}$$

Therefore, equation (3.87) turns into:

$$\frac{\partial U}{\partial t} + v_s \frac{\partial U}{\partial y} = 0 \tag{3.94}$$

This is a 1D nonlinear convection equation, similar to the inviscid *Burgers' equation*, thus it correctly describes the evolution of a wave feeded by a flow injection at the inlet which is, in turn, equal to the flow ejection at the outlet. However, this solution does not describe the expansion of a solid material, because the average solid density seems to increase along the domain. Instead, the expected result should be similar to the physics of a shock-tube: the flow density increases after the shock wave but, on the other side, it decreases because of the expansion waves (Figure 3.11). The physical mechanism beyond this behaviour is naturally different, but the expected result is comparable.

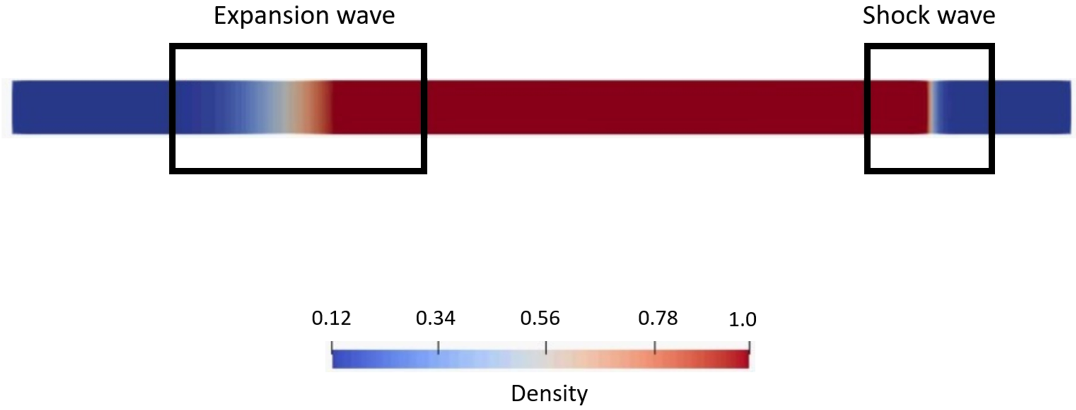

Figure 3.11: An analogy with the shock-tube.

A swelling porous material can indeed be treated as an elastic sponge: stretching the sponge, the region close to the interface on the side of the gas will see an increase in $\langle \rho_s \rangle$, due to the injection of solid mass where an instant before there was a pure fluid. At the same time, on the other side of the interface, $\langle \rho_s \rangle$ has to decrease because the solid mass has been convected over a bigger volume. This leads to the conclusion that the solid mass conservation is due to the elastic nature of the material, so that solving a simple transport equation in $\langle \rho_s \rangle$ seems not to be a sufficient condition to ensure respect for the conservation law. Finding practicable alternatives thus requires understanding of what the assumption of a constant velocity has physically implied: the first solid points starting to swell are the ones very close to the interface because, in the general context of atmospheric re-entry, they are subjected to aerodynamic heating, whilst the solid points which are far from the interface must have an initial velocity equal to zero. The first consequence is that not all the solid particles should move and the moving ones should not have all the same velocity. Therefore, a simplified way to guarantee the solid mass conservation without involving the theory of elasticity could be to impose a velocity profile characterized by a null value at the bottom (in order to stop the mass injection at the boundary) and a positive gradient at the interface (where the heat load triggers the swelling mechanism), as shown in Figure 3.12. A final comment concerns the particles inside the pure fluid region: although a non-zero velocity has been imposed on them, they are not involved in the swelling motion because v_s is mutiplied by U which, in that region, is equal to zero, so that the convective term is not active there.

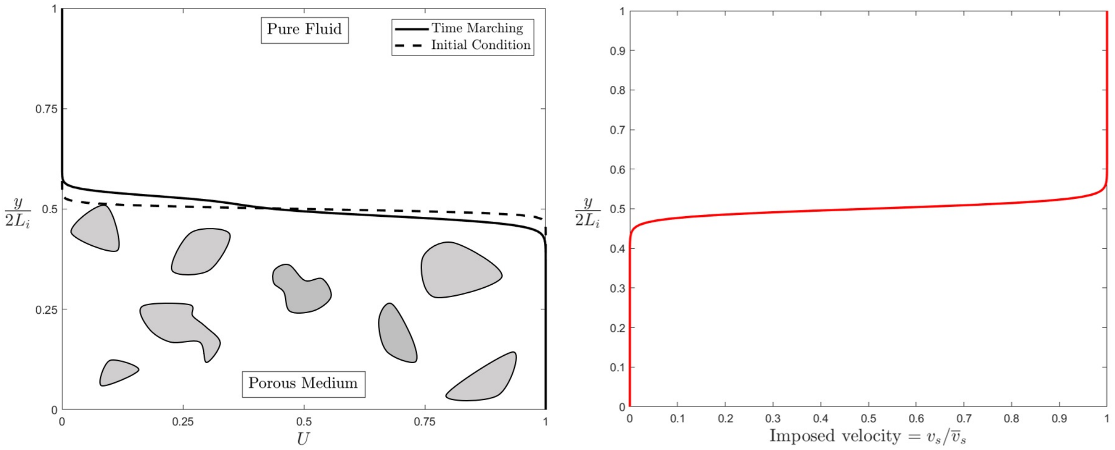

Figure 3.12: Velocity profile ensuring the solid mass conservation.

Such a velocity profile can be modeled as:

$$v_s(y) = \overline{v}_s S(y) \tag{3.95}$$

where $S(y)$ is the function used to describe the velocity gradient:

$$S(y) = \frac{1}{1 + e^{-(y - L_i)}} \tag{3.96}$$

The choice fell on the sigmoid function, because it is easy to manipulate in order to take into account other physical effects. One of these, could be the effect of thermal gradients: the swelling mechanism consists indeed in a thermal expansion, therefore it is expected to automatically stop when the temperature gradients decrease below a minimum value. Considering the 1D energy conservation equation:

$$\frac{\partial T}{\partial t} + \underbrace{v_s \frac{\partial T}{\partial y}}_{C} = \underbrace{\nu \frac{\partial^2 T}{\partial y^2}}_{D} \tag{3.97}$$

where ν is the thermal diffusivity:

$$\nu = \frac{k}{\rho c} \tag{3.98}$$

k_v, ρ_v and c_v are respectively the thermal conductivity, density and specific heat capacity. Since $\mathrm{Pe} = C/D \ll 1$, the convective term C is negligible. This allows to solve a 1D pure diffusion equation, i.e. the 1D heat equation, decoupling it from the convection equation:

$$\frac{\partial T}{\partial t} = \nu \frac{\partial^2 T}{\partial y^2} \tag{3.99}$$

As a first approximation, equation (3.99) can be solved for the virgin material (denoted with the subscript v):

$$\frac{\partial T_v}{\partial t} = \frac{k_v}{\rho_v c_v} \frac{\partial^2 T_v}{\partial y_v^2} \tag{3.100}$$

For the purpose of reproducing the test in Plasmatron, the boundary conditions can be defined as follows:

$$\begin{cases} y = 0 & \longrightarrow \quad k_v \dfrac{\partial T_v}{\partial y_v} = 0 \\ y = L_i & \longrightarrow \quad k_v \dfrac{\partial T_v}{\partial y_v} = \dot{q}_{\text{ext}} - \varepsilon_v \sigma T_w^2 \end{cases} \tag{3.101}$$

where ε_v is the emissivity of the virgin material, $\dot{q}_{\text{ext}}$ is the external heat flux, σ is the Stefan–Boltzmann constant and T_w is the wall temperature.

Assuming a linear thermal expansion, the general definition for the expansion coefficient α is given by:

$$\alpha = \frac{1}{L} \frac{\mathrm{d}L}{\mathrm{d}T} \tag{3.102}$$

The local strain ϵ is defined as:

$$\epsilon = \frac{\mathrm{d}L}{L} = \alpha \ \mathrm{d}T \tag{3.103}$$

A relation between strain and displacement also exists:

$$\epsilon = \frac{\mathrm{d}s}{\mathrm{d}y} \tag{3.104}$$

The displacement field can thus be found as:

$$s = \int_0^L \epsilon \ \mathrm{d}y = \int_0^L \alpha \ \mathrm{d}T \ \mathrm{d}y \tag{3.105}$$

In an evolution problem, s and T are function of time too. Therefore, computing the time derivative and assuming α as a constant, it is possible to define a velocity related to the effect of thermal gradients:

$$\hat{v}_s(t) = \frac{\partial s}{\partial t} = \alpha \int_0^L \frac{\partial T}{\partial t} \ \mathrm{d}y \tag{3.106}$$

where the temperature gradient is computed solving the 1D heat equation (3.100). Hence, a new definition for the swelling velocity can be considered:

$$v_s(y,t) = \hat{v}_s(t) S(y) \tag{3.107}$$

While in equation (3.95) there is no relation with the history of the flow because $\overline{v}_s$ is a mean velocity, $\hat{v}_s$ is a function of time. Therefore, the spatial distribution is modeled by the sigmoid function $S(y)$ and the evolution in time is described in terms of a decreasing velocity $\hat{v}_s(t)$, which is driven by the temporal variation of thermal gradients. Finally, concerning the linear thermal expansion coefficient α, it can be determined experimentally. In the MATLAB code written to test the physical model, α is computed matching it with data of Sakraker [7], who provided the swelling period Δt and the final length L_f of the sample. An iterative process can be adopted to look for the value of α which allows to stop the thermal expansion after a period equal to Δt, showing a final length equal to L_f.

What has just been described is a simplified approach, because of two main assumptions. The first approximation is related to the resolution of the 1D heat equation (3.100) over a domain of length L_i; this is indeed the length of the virgin material and it should change because of swelling and recession due to oxidation too. Nevertheless, the temperature field inside the material is not expected to experience high variations due to the phenomena mentioned, therefore this is a reasonable hypothesis. The second simplification is that equation (3.100) is solved for a material (virgin) which maintains its physical properties constant but, in view of a future implementation within ARGO, pyrolysis should be considered too, so that the physical properties k, ρ and c actually would change during the thermal decomposition. ARGO accounts for this effect by means of the progress variable ξ, that has been introduced in equation (3.67) to reflect the local decomposition state of the material. Hence, the points of the material where pyrolysis has not yet occurred are denoted with $\xi = 0$ while, in contrast, the region where the medium has been totally charred is identified by $\xi = 1$. The transitional zone, i.e. the pyrolysis layer, is characterized by $0 < \xi < 1$. The same philosophy has been thought for this physical model, in order to increase the degree of compatibility with ARGO. In this case, the only available parameter capable of reflecting the decomposition state of the material is the local temperature. Therefore, a pyrolysis temperature T_p is used to locate the border ($\xi = 0$) between the virgin zone and the pyrolysis layer, whilst a char temperature T_c is chosen to identify the edge ($\xi = 1$) between the pyrolysis layer and the totally charred zone, as shown in Figure 3.13.

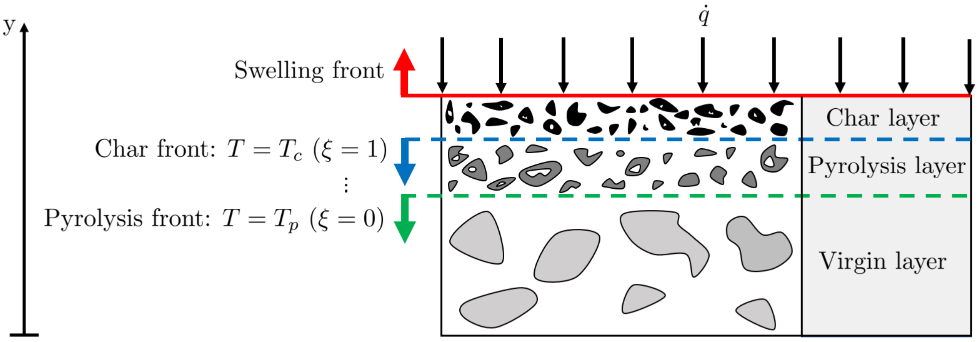

Figure 3.13: Two characteristic temperatures are tracked in order to locate pyrolysis and char fronts.

Both pyrolysis and char fronts are expected to travel along the material, when it is subjected to a heat flux $\dot{q}$. Hence, the velocity profile defined by equation (3.107) is shifted down at each time step in order to track the pyrolysis front, which is moving at a mean velocity $(\overline{v}_s)_{\xi=0}$ along the positions $y_{\xi=0}(t)$. Furthermore, since the pyrolysis front is expected to move faster than the char front (i.e. $(\overline{v}_s)_{\xi=0} > (\overline{v}_s)_{\xi=1}$), the pyrolysis layer will see an increase in its thickness, defined by means of the parameter $\delta_p(t)$:

$$\frac{1}{\delta_p(t)} = y_{\xi=1}(t) - y_{\xi=0}(t) \tag{3.108}$$

The expanding thickness $(y_{\xi=1}-y_{\xi=0})$ of the pyrolysis layer can be simulated manipulating the sigmoid function $S(y)$ in order to change its slope, i.e. smoothing the velocity gradient at the interface. Combining these effects, the final definition for the swelling velocity is:

$$v_s(y,t) = \hat{v}_s(t)\frac{1}{1+e^{\delta_p(t)\{-(y-L_i)-[L_i-y_{\xi=0}(t)]\}}} \tag{3.109}$$

All these aspects will be clarified in Section 5.5, analyzing the results provided by the Matlab simulations.

3.3 Road map for the implementation

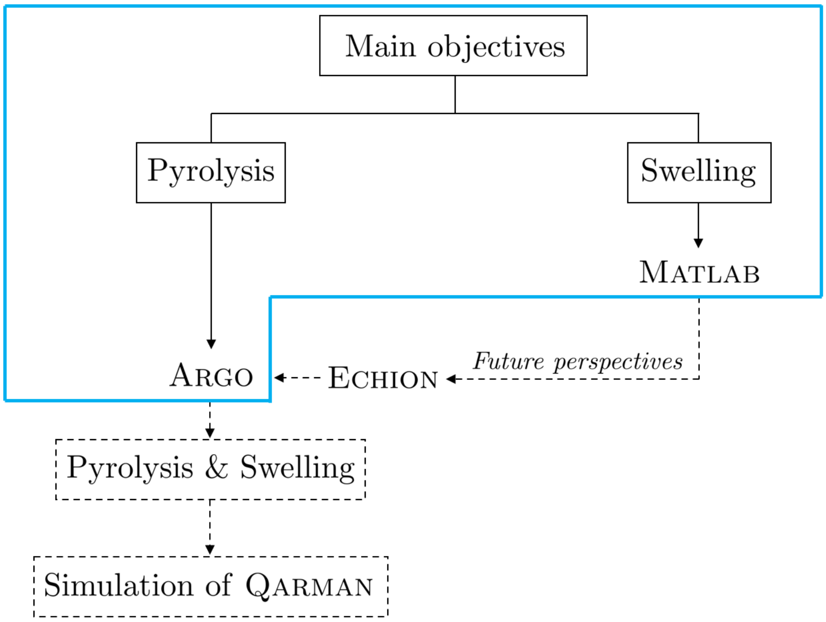

Figure 3.14: Road map for the implementation. The dash lines indicate the future developments.

A road map is given in Figure 3.14, to help the reader to follow the logical flow of the current work and the future perspectives. In this thesis, there are two main objects of study: pyrolysis and swelling. The contribution to the former is in the implementation within of ARGO of a more sophisticated approach to compute the pyrolysis production rate. This has a direct impact not only on cork-based ablative materials, but also on carbon-based ones. However, ARGO is not capable of treating swelling materials yet, therefore a physical model accounting for this phenomenon has been proposed and tested, as a preliminary study, within MATLAB. A great attention has been paid to follow the same philosophy used by ARGO in the treatment of this kind of physical problems, for the purpose of ensuring a large degree of compatibility for a future implementation within *DGAblation*. As an intermediate step, this model could be first implemented within ECHION, a one-dimensional material response code developed at Cenaero [11] and characterized by an architecture similar to ARGO, but simplified. The final aim is to get an appealing numerical tool capable of simulating the re-entry of the QARMAN CubeSat and, more generally, of cork-phenolic ablators.

Chapter 4

Numerical methods

This chapter presents the numerical methods adopted to solve the systems of governing partial differential equations. Since two distinct codes have been used to perform the simulations, two different discretization techniques have to be discussed. In fact, the multi-physics CFD code ARGO, used to simulate ablation in a high-enthalpy flow, is based on the Discontinuous Galerkin Method (DGM). Instead, the Finite Difference Method (FDM) is used within the MATLAB code developed to simulate the swelling mechanism. Hence, a general summary of the two formulations will be presented.

4.1 The Discontinuous Galerkin Method

The Discontinuous Galerkin Method (DGM) is considered as a special class of FEM, but it is often classified as a particular numerical technique combining the Finite Volume (FVM) and the Finite Element (FEM) methods. Therefore, the advantages of both of these approaches are merged togheter, in order to offer a modern numerical method characterized by high order of accuracy on unstructured grids, computational efficiency, robustness, compactness and scalability [63], [11]. CFD codes are typically based on FVM or FDM, even if most of the codes taking into account the material thermal response are applied to simple geometries. At the same time, the versatility of FEM solvers in handling complex geometries and boundary conditions by means of unstructured meshes makes them very appealing for ablation simulations [64].

The system of governing equations (3.72) has been presented in a compact form as a hyperbolic conservation equation:

$$\frac{\partial \mathbf{U}}{\partial t} + \nabla \cdot \mathbf{F}^c - \nabla \cdot \mathbf{F}^d - \mathbf{S} = 0 \tag{4.1}$$

A general form can be adopted to introduce the DGM, considering the solution vector $\tilde{\mathbf{u}}_m$:

$$\mathcal{L}_m(\tilde{\mathbf{u}}) = 0, \quad \forall m = 1, ..., N_v \tag{4.2}$$

where $\mathcal{L}_m$ is a differential operator and N_v is the number of variables in the system. Hence, equation (4.1) can be formulated as follows:

$$\mathcal{L}_m(\tilde{\mathbf{u}}) = \frac{\partial \tilde{u}_m}{\partial t} + \nabla \cdot F^c_m(\tilde{\mathbf{u}}) - \nabla \cdot F^d_m(\tilde{\mathbf{u}}, \nabla \tilde{\mathbf{u}}) - S(\tilde{\mathbf{u}}, \nabla \tilde{\mathbf{u}}) = 0 \tag{4.3}$$

Using an alternative form for the divergence:

$$\mathcal{L}_m(\tilde{\mathbf{u}}) = \frac{\partial \tilde{u}_m}{\partial t} + \frac{\partial}{\partial x^k} F_m^{c,k}(\tilde{\mathbf{u}}) - \frac{\partial}{\partial x^k} F_m^{d,k}(\tilde{\mathbf{u}}, \nabla \tilde{\mathbf{u}}) - S(\tilde{\mathbf{u}}, \nabla \tilde{\mathbf{u}}) = 0 \tag{4.4}$$

The diffusive term $F_m^{d,k}$ can be defined as follows:

$$F_m^{d,k} \approx -D_{m,n}^{k,l}(\mathbf{u}) \frac{\partial \tilde{\mathbf{u}}_n}{\partial x^l} \tag{4.5}$$

where $D_{m,n}^{k,l}$ is the Jacobian of the diffusive flux with respect to the solution gradient [63], [11].

An infinite number of values are required to solve the system of equations (4.4) and determine the exact solution vector $\tilde{\mathbf{u}}$, so that the only practicable way consists in the computation of an approximate solution $\mathbf{u}$, within a finite-dimensional trial function vector space $\mathcal{V}$. The domain of computation Ω is thus discretized into a finite number of elements Ω_e which, as a whole, constitute the computational grid (mesh). There is no constraint on the shape of the elements, but they must cover the whole domain without overlapping. Therefore, the finite-dimensional vector space $\mathcal{V}$ is defined by means of piecewise polynomial approximations, i.e. polynomials of order p which have to be a regular behaviour within each element but they are allowed to be discontinuous at the interfaces across elements, as shown in Figure 4.1. For this reason, the number of DOFs (degrees of freedom) is duplicated, therefore the high-order accuracy implies a greater computational cost.

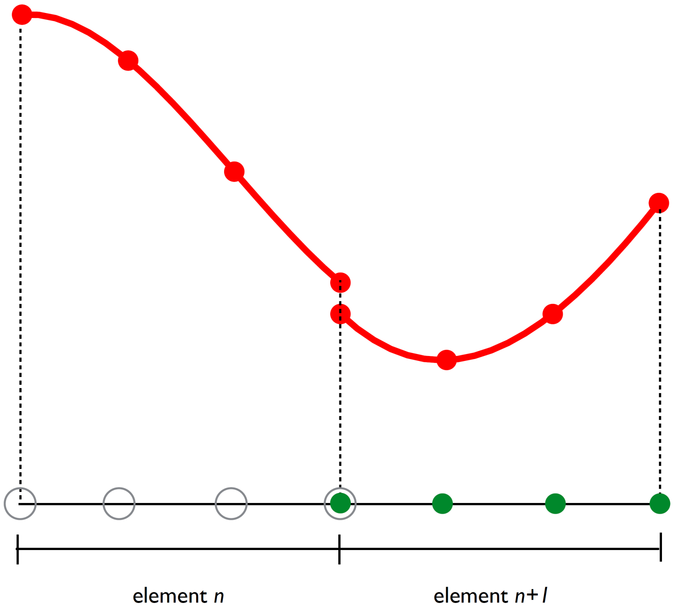

Figure 4.1: Discretization through a third order Lagrangian polynomial interpolation. Figure taken from [11], [63].

The approximate solution u_m is determined as a linear combination of the shape functions ζ_i, which form a basis for $\mathcal{V}$:

$$\tilde{\mathrm{u}}_m \approx u_m = \sum_{i=1}^{N} U_{i,m}\zeta_i \tag{4.6}$$

where N is the number of elements in the grid, while the coefficients $U_{i,m}$ represent the DOFs of the problem, i.e. a set of independent parameters which completely describe the configuration of the system. Eventually, different shapes can be considered for the elements, so that:

$$u_m = \sum_{e}\sum_{i=1}^{N^e} U^e_{i,m}\zeta^e_i \tag{4.7}$$

A Lagrangian polynomial interpolation of order p is used within ARGO, with equidistant nodes on each element [11]. In other words, on each element a set of nodes (the DOFs of the problem) is defined. The solution is thus approximated with an interpolation of its nodal values. Furthermore, a mapping is operated to transform each element into a reference one. In particular, this transformation allows to write the interpolating polynomials in terms of the parametric coordinates (ξ_1, ξ_2, ξ_3), rather than the physical ones (x_1, x_2, x_3), as shown in Figure 4.2.

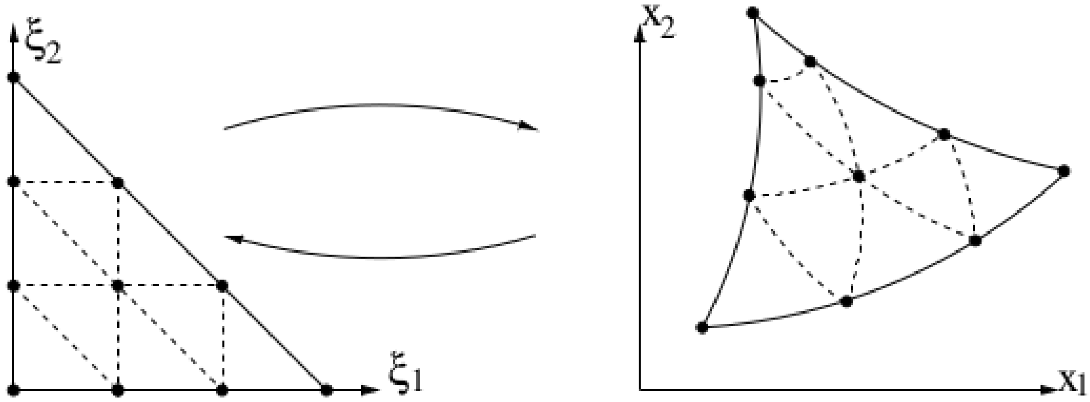

Figure 4.2: Transformation from physical coordinates to parametric ones (and viceversa). Image taken from [11].

The differential problem described by $\mathcal{L}_m(\tilde{u}_m) = 0$ is satisfied only by the exact solution $\tilde{u}_m$. Instead, applying the approximate solution u_m produces a residual, so that $\mathcal{L}_m(u_m) = \varepsilon_R \neq 0$. Therefore, the Galerkin variational formulation is applied to found the coefficients $U_{i,m}$ of the approximation:

$$\int_{\Omega} v\mathcal{L}_m(\mathbf{u}) = 0, \quad \forall v \in \mathcal{V} \tag{4.8}$$

Equation (4.8) allows to impose the orthogonality of the residual on the basis of the shape functions within the trial space vector $\mathcal{V}$. Hence, the weak formulation for the convection-diffusion-reaction problem is given by [11]:

$$
\begin{aligned}
\int_\Omega v\mathcal{L}_m(u) = 0, \quad & \forall v \in \mathcal{V},\ \forall m \in N_v \\
&= \underbrace{\sum_{\Omega_e\in\Omega} \int_{\Omega_e} v\frac{\partial u_m}{\partial t}\ \mathrm{d}\Omega_e +}_{T_v} \\
&- \underbrace{\sum_{\Omega_e\in\Omega} \int_{\Omega_e} \frac{\partial v}{\partial x^k} F_m^{c,k}(\mathbf{u})\ \mathrm{d}\Omega_e}_{C_v} + \underbrace{\sum_{I_i\in I} \oint_{I_i} [v]^k n^k \mathcal{H}_m(\mathbf{u}^+, \mathbf{u}^-, \mathbf{n})\ \mathrm{d}S +}_{C_i} \\
&+ \underbrace{\sum_{\Omega_e\in\Omega} \int_{\Omega_e} \frac{\partial v}{\partial x^k} F_m^{d,k}(\mathbf{u})\ \mathrm{d}\Omega_e}_{D_v} - \underbrace{\sum_{I_i\in I} \oint_{I_i} \langle D_{m,n}^{k,l} \frac{\partial \mathbf{u}_n}{\partial x^l}\rangle [v]^k\ \mathrm{d}S +}_{D_i} \\
&- \underbrace{\theta \sum_{I_i\in I} \oint_{I_i} \langle D_{m,n}^{k,l} \frac{\partial v}{\partial x^l}\rangle [u_m]^k\ \mathrm{d}S}_{D_t} + \underbrace{\alpha \sum_{I_i\in I} \oint_{I_i} [v]^k [u_m]^k\ \mathrm{d}S +}_{D_p} \\
&- \underbrace{\sum_{\Omega_e\in\Omega} \int_{\Omega_e} vS(\mathbf{u}, \nabla\mathbf{u})\ \mathrm{d}\Omega_e}_{S_v}
\end{aligned}
\tag{4.9}
$$

where Ω_e denotes the elements, I_i indicates the interfaces across elements and $\mathcal{H}$ represents the interface fluxes. Furthermore, the jump $[...]$ and the average $\langle ... \rangle$ operators are defined as follows [11]:

$$[a] = a^- n^- + a^+ n^+ \tag{4.10}$$

$$\langle a \rangle = \frac{1}{2}(a^- + a^+) \tag{4.11}$$

The terms T_v, C_v, D_v and S_v are respectively the temporal, convective, diffusive and source terms and they are present in Continuous Galerkin Finite Element Method (CGFEM) too. Instead, C_i, D_i, D_t and D_p represent the internal boundary conditions between two adjacent elements. They are related to the discontinuity of the polynomial functions at the interfaces, therefore they are missing in CGFEM [11].

Convective variational form

The discretization of the convective terms can be derived as a high-order extension of the classical upwind FVM [63]. This can be easily deducted simplifying equation (4.9) to the one-dimensional case in a single variable [11]:

$$
\begin{aligned}
\int_{\Omega} v\mathcal{L}(u) = 0, \quad & \forall v \in \mathcal{V} \\
& = \underbrace{\sum_{\Omega_e \in \Omega} \int_{\Omega_e} v\frac{\partial u}{\partial t}\ \mathrm{d}\Omega_e}_{T_v} + \\
& - \underbrace{\sum_{\Omega_e \in \Omega} \int_{\Omega_e} \frac{\partial v}{\partial x} F^c(u)\ \mathrm{d}\Omega_e}_{C_v} + \underbrace{\sum_{I_i \in I} \oint_{I_i} [v]\mathcal{H}(u^+, u^-, \mathbf{n})\ \mathrm{d}S}_{C_i}
\end{aligned}
\tag{4.12}
$$

If a piecewise constant function ($p = 0$) is chosen for v, the C_v term becomes equal to zero and the equation is reduced to an equivalent form of a classical first order FVM, as the temporal term is computed evaluating the interface fluxes:

$$
\sum_{\Omega_e \in \Omega} \int_{\Omega_e} v\frac{\partial u}{\partial t}\ \mathrm{d}\Omega_e = -\sum_{I_i \in I} \oint_{I_i} [v]\mathcal{H}(u^+, u^-, \mathbf{n})\ \mathrm{d}S \tag{4.13}
$$

Diffusive variational form

Various DG formulations are available within ARGO for the discretization of the diffusive terms. In particular, three different classes of Interior Penalty (IP) methods have been implemented, because of their compactness: SIPDG (*symmetric interior penalty method*), NIPDG (*non-symmetric interior penalty method*) and IIPDG (*incomplete interior penalty method*). However, the BR2 (second scheme of Bassi and Rebay) has been chosen as DG formulation of diffusion for the simulations performed in this work.

Interface fluxes

In DGM, the solution should not necessarily be continuous across elements, therefore a Riemann solver is needed for the computation of the interface fluxes, as in a FVM. For this purpose, various Riemann solvers for compressible flows have been implemented within ARGO, such as the exact Riemann solver, the Roe approximate Riemann solver and a Lax-Friedrich scheme. The last one has been chosen because it was easily applicable to a multispecies flow. However, considering the large temperatures involved in a high-enthalpy flow, the consequent high sound speed can imply very low Mach numbers, so that a compressible solver could cause numerical instabilities. In fact, in the physics of an incompressible flow a strong relation between pressure and velocity exists, so the velocity field is particularly sensitive to the pressure fluctuations and it instantly changes according to them. From a numerical point of view, the treatment of such a flow could be very challenging and may lead to convergence and accuracy issues [11].

For this reasons, the AUSM$^+$ *up* scheme has been made available, because of the great versatility it offers in all Mach number regimes and also due to the possibility of an easy extension to chemically reacting flows. Finally, another numerical scheme belonging to the same class, the Simple Low-dissipation AUSM (SLAU), is included within Argo. It ensures low numerical diffusion and it is combined with a preconditioning of the time derivative in order to grant good convergence properties at low Mach numbers [65]. Therefore, the SLAU scheme has been chosen as Riemann solver for the simulations performed in this work.

Implementation of boundary conditions

The resolution of the governing equations requires the specification of suitable conditions at the boundaries of the computational domain, in order to obtain a unique solution. Within Argo, boundary conditions are implemented weakly, since there are no grid points at the boundaries. Therefore, for the convective part, the values of the so-called *ghost cells* are typically specified. In this way, fictitious cell external to the domain allow to compute the boundary convective fluxes in a classical way, i.e. solving a Riemann problem [11], [66]. Generally, for hyperbolic Euler equations, the number of boundary conditions to be enforced should be equal to the number of characteristics which do not reach a specific boundary from the interior of the domain [67]. Considering Navier-Stokes equations, the diffusive part requires to be treated at the boundaries too and, for this purpose, either Dirichlet, Neumann or Robin boundary conditions are implemented [11]. The main boundary conditions which can be found in the *DGAblation* module of Argo are listed in Table 4.1.

Table 4.1: Boundary conditions implemented within the *DGAblation* module of Argo. Inner values are denoted with superscript $-$, while outer values with $+$. Table reproduced from [11].

B.C. type	**Euler conditions**	**Navier-Stokes conditions**
Subsonic inflow	$\mathbf{u}^-$, T^-, Y_i^- are given and $P^+ = P^-$	$\mathbf{F}^{d,+} \cdot \mathbf{n} = 0$
Adiabatic wall	$\mathbf{u}^-$ is given while other variables are taken as $\mathbf{U}^+ = \mathbf{U}^-$	$\mathbf{F}^{d,+}_{\text{energy}} \cdot \mathbf{n} = 0$, $\mathbf{F}^{d,+}_{\text{mass}} \cdot \mathbf{n} = 0$
Isothermal wall	$\mathbf{u}^-$ and T^- are given while other variables are taken as $\mathbf{U}^+ = \mathbf{U}^-$	$\mathbf{F}^{d,+}_{\text{mass}} \cdot \mathbf{n} = 0$
Subsonic outlet	P^- is given while other variables are taken as $\mathbf{U}^+ = \mathbf{U}^-$	$\mathbf{F}^{d,+} \cdot \mathbf{n} = 0$
Symmetry	$\mathbf{U}^+ = \mathbf{U}^-$	$\nabla \mathbf{U}^+ \cdot \mathbf{n} = 0$
Freestream	$\mathbf{u}^-$, T^-, Y_i^-, P^- are given	$\mathbf{F}^{d,+} \cdot \mathbf{n} = 0$

Time discretization

The *unified approach* involves the presence of an interface between the pure fluid region and the porous material and, considering that this interface is expected to move because of ablation phenomena, the physical problem has a strongly unsteady nature. The numerical resolution of such a problem thus requires a time discretization technique. In Argo code, both explicit and implicit schemes are available, even though the complex dynamics involving chemical reactions and mass diffusion imposes important restrictions to the usable time step [11]. Moreover, the presence of stiff processes such as pyrolysis makes extremely hard the integration of the PDEs, so that an explicit scheme would easily lead to numerical instabilities. For these reasons, an implicit strategy has been chosen for the numerical resolution of Navier-Stokes equations in this work. In particular, the multistep *Backward Differentiation Formula at second order* (BDF2) has been used. Considering the compact form of the governing equations:

$$\frac{\partial \mathbf{U}}{\partial t} + \nabla \cdot \mathbf{F}^c - \nabla \cdot \mathbf{F}^d - \mathbf{S} = 0 \tag{4.14}$$

and assembling convective, diffusive and source terms:

$$\mathcal{R}^{CDS}(\mathbf{U}) = -\nabla \cdot \mathbf{F}^c + \nabla \cdot \mathbf{F}^d + \mathbf{S} \tag{4.15}$$

equation (4.14) can be re-written as:

$$\frac{\partial \mathbf{U}}{\partial t} = \mathcal{R}^{CDS}(\mathbf{U}) \tag{4.16}$$

Hence, the BFD2 scheme computes $\mathbf{U}$ at the next step as follows [11]:

$$\mathbf{U}^{n+1} = \mathbf{U}^n + \Delta t\ \mathcal{R}^{CDS}(\mathbf{U}^{n+1}) \tag{4.17}$$

$$\mathbf{U}^{n+2} = \frac{4}{3}\mathbf{U}^{n+1} - \frac{1}{3}\mathbf{U}^n - \frac{2}{3}\Delta t\ \mathcal{R}^{CDS}(\mathbf{U}^{n+2}) \tag{4.18}$$

where n is the index of grid in time, while Δt is the time step. Furthermore, as an implicit scheme requires the resolution of a system of nonlinear equations, it is combined with a *Newton-Raphson algorithm* that, in turn, has to be coupled with a linear solver. The linear problem can be expressed as follows [11]:

$$\mathbf{L}^* \Delta \mathbf{U} = -\mathbf{r}^* \tag{4.19}$$

where $\mathbf{L}^*$ is the Jacobian matrix, while $\mathbf{r}^*$ is the residual. As linear solver, the *Generalized Minimal Residual Method* (GMRES) has been used in this work, an iterative method based on the *Coniugate Gradient Method*. In particular, the latter represents the state of the art of iterative methods for the resolution of linear systems but it can be used only for a symmetric positive definite matrix; GMRES is instead generalized to a nonsymmetric matrix. Moreover, considering that the problem associated to equation (4.19) is usually badly conditioned, GMRES is combined with a preconditioner, in order to reduce the number of iterations needed to reach convergence. Specifically, an *Incomplete LU factorization* (ILU) has been chosen for the simulations performed in this work.

4.2 The Finite Difference Method

The Finite Difference Method (FDM) is a numerical approach capable of providing an approximate solution to differential equations, by means of a discretization that results in a system of algebraic equations [68]. The philosophy of this numerical method comes from the definition of derivative at a point x_i:

$$\left(\frac{\partial\phi}{\partial x}\right)_{x_i} = \lim_{\Delta x\to 0}\frac{\phi(x_i+\Delta x)-\phi(x_i)}{\Delta x} \tag{4.20}$$

where ϕ is a generic variable. The idea behind the FDM is to approximate the derivative directly by means of the difference quotient, considering a Δx that should be small enough to neglect the limit as Δx approaches zero. This results in the discretization of the geometric domain in a certain number of grid points (nodes), in order to generate a structured computational grid characterized by a spacing Δx_i, as in Figure 4.3. In FDM, the Δx_i is thus a finite quantity, so the approximation becomes better the smaller Δx_i is. In other terms, the grid refinement allows to reduce the error faster, increasing the order of approximation [68].

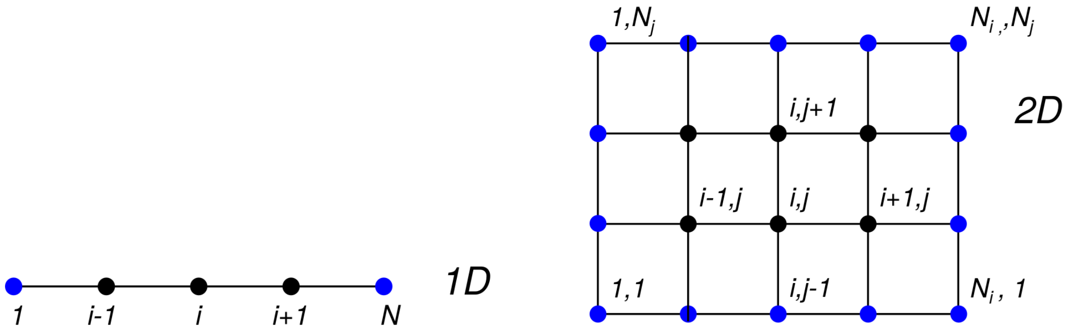

Figure 4.3: FDM: computational grid for 1D and 2D. Credits: [67].

The Figure 4.4 shows the basic schemes for the approximation of a derivative, such as the backward, forward and central differences. The FDM is thus applied for the estimation of the slope at each x_i. The choice of the numerical scheme affects both the accuracy and stability; for instance, the forward and backward difference schemes are first-order accurate, while the central difference scheme is second-order accurate [67], even though it is also less stable so that it may results in spurious numerical oscillations.

Approximations of the first derivative

In the physical model developed in this work, both first and second derivatives need to be approximated. In any case, the finite difference representation can be obtained using

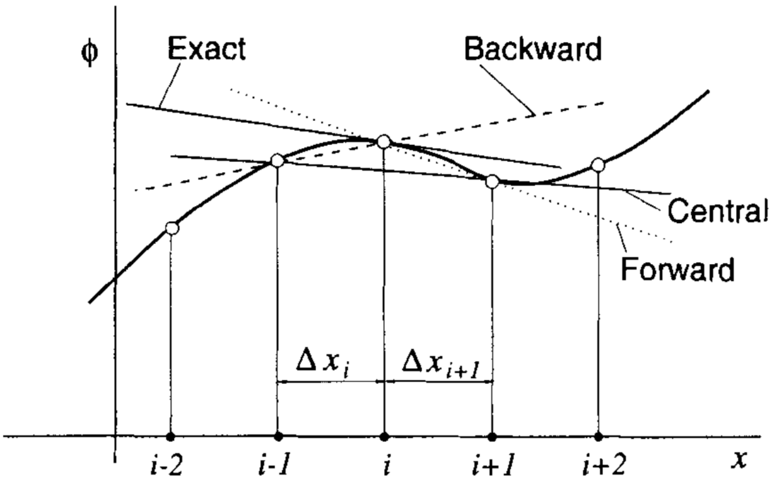

Figure 4.4: Different schemes for the approximation of a derivative. Figure taken from [68].

the Taylor's series expansions:

$$\begin{aligned}\phi(x) =&\phi(x_i) + (x-x_i)\left(\frac{\partial\phi}{\partial x}\right)_{x_i} + \frac{(x-x_i)^2}{2!}\left(\frac{\partial^2\phi}{\partial x^2}\right)_{x_i} + \frac{(x-x_i)^3}{3!}\left(\frac{\partial^3\phi}{\partial x^3}\right)_{x_i} + \\ &+\ \dots\ + \frac{(x-x_i)^n}{n!}\left(\frac{\partial^n\phi}{\partial x^n}\right)_{x_i} + H\end{aligned} \tag{4.21}$$

where, H is the leading truncation error due to the neglect of higher order terms. Replacing x by x_{i+1}:

$$\begin{aligned}\phi(x_{i+1}) =&\phi(x_i) + (x_{i+1}-x_i)\left(\frac{\partial\phi}{\partial x}\right)_{x_i} + \frac{(x_{i+1}-x_i)^2}{2!}\left(\frac{\partial^2\phi}{\partial x^2}\right)_{x_i} + \\ &\frac{(x_{i+1}-x_i)^3}{3!}\left(\frac{\partial^3\phi}{\partial x^3}\right)_{x_i} +\ \dots\ + \frac{(x_{i+1}-x_i)^n}{n!}\left(\frac{\partial^n\phi}{\partial x^n}\right)_{x_i} + H\end{aligned} \tag{4.22}$$

Therefore, the first derivative evaluated at x_i is given by:

$$\left(\frac{\partial\phi}{\partial x}\right)_i = \frac{\phi_{i+1}-\phi_i}{x_{i+1}-x_i} - \frac{x_{i+1}-x_i}{2}\left(\frac{\partial^2\phi}{\partial x^2}\right)_i - \frac{(x_{i+1}-x_i)^2}{6}\left(\frac{\partial^3\phi}{\partial x^3}\right)_i + H \tag{4.23}$$

Instead, replacing x by x_{i-1} the derivative results in:

$$\left(\frac{\partial\phi}{\partial x}\right)_i = \frac{\phi_i-\phi_{i-1}}{x_i-x_{i-1}} + \frac{x_i-x_{i-1}}{2}\left(\frac{\partial^2\phi}{\partial x^2}\right)_i - \frac{(x_i-x_{i-1})^2}{6}\left(\frac{\partial^3\phi}{\partial x^3}\right)_i + H \tag{4.24}$$

Finally, it is possible to get another scheme replacing x by x_{i+1} and x_{i-1}:

$$\begin{aligned}\phi(x_{i+1}) =&\phi(x_i) + (x_{i+1}-x_i)\left(\frac{\partial\phi}{\partial x}\right)_{x_i} + \frac{(x_{i+1}-x_i)^2}{2!}\left(\frac{\partial^2\phi}{\partial x^2}\right)_{x_i} + \\ &+ \frac{(x_{i+1}-x_i)^3}{3!}\left(\frac{\partial^3\phi}{\partial x^3}\right)_{x_i} + O(x_{i+1}-x_i)^4\end{aligned} \tag{4.25}$$

$$\begin{aligned}\phi(x_{i-1}) =&\phi(x_i) - (x_i-x_{i-1})\left(\frac{\partial\phi}{\partial x}\right)_{x_i} + \frac{(x_i-x_{i+1})^2}{2!}\left(\frac{\partial^2\phi}{\partial x^2}\right)_{x_i} + \\ &- \frac{(x_i-x_{i-1})^3}{3!}\left(\frac{\partial^3\phi}{\partial x^3}\right)_{x_i} + O(x_i-x_{i-1})^4\end{aligned} \tag{4.26}$$

If equation (4.26) is subtracted from equation (4.25), the first derivative is given by:

$$\begin{aligned}\left(\frac{\partial\phi}{\partial x}\right)_i =&\frac{\phi_{i+1}-\phi_{i-1}}{x_{i+1}-x_{i-1}} - \frac{(x_{i+1}-x_i)^2-(x_i-x_{i-1})^2}{2(x_{i+1}-x_{i-1})}\left(\frac{\partial^2\phi}{\partial x^2}\right)_i + \\ &- \frac{(x_{i+1}-x_i)^3+(x_i-x_{i-1})^3}{6(x_{i+1}-x_{i-1})}\left(\frac{\partial^3\phi}{\partial x^3}\right)_i + H\end{aligned} \tag{4.27}$$

Equations (4.23), (4.24) and (4.27) provide an exact evaluation for the first derivative but, if the spacing ($x_{i+1}-x_i$ and x_i-x_{i-1}) is small, the higher order terms, which are further unknowns, can be neglected in order to obtain an approximate solution for the derivative.

$$\left(\frac{\partial\phi}{\partial x}\right)_i \approx \frac{\phi_{i+1}-\phi_i}{x_{i+1}-x_i} \tag{4.28}$$

$$\left(\frac{\partial\phi}{\partial x}\right)_i \approx \frac{\phi_i-\phi_{i-1}}{x_i-x_{i-1}} \tag{4.29}$$

$$\left(\frac{\partial\phi}{\partial x}\right)_i \approx \frac{\phi_{i+1}-\phi_{i-1}}{x_{i+1}-x_{i-1}} \tag{4.30}$$

Equations (4.28), (4.29) and (4.30) represent the forward difference (FDS), backward difference (BDS) and central difference (CDS) schemes, respectively. The high order terms neglected at right-hand side constitutes the truncation error that, for a uniform grid ($\Delta x_i = \Delta x$), can be expressed as follows:

$$\varepsilon_\tau = (\Delta x)^m\alpha_{m+1} + (\Delta x)^{m+1}\alpha_{m+2} + \ \dots\ + (\Delta x)^n\alpha_{n+1} \tag{4.31}$$

where α is a higher-order derivative multiplied by a constant factor, while m is the exponent of the leading truncation term [68]. The truncation error is thus representative of the order of accuracy and, since it is proportional to $(\Delta x)^m$, it expresses the rate at which the error decreases as the grid is refined [67], [68]. For a uniform grid, the exact expression of the first derivative is given by:

$$\left(\frac{\partial \phi}{\partial x}\right)_i = \frac{\phi_{i+1} - \phi_i}{\Delta x} + O(\Delta x) \tag{4.32}$$

$$\left(\frac{\partial \phi}{\partial x}\right)_i = \frac{\phi_i - \phi_{i-1}}{\Delta x} + O(\Delta x) \tag{4.33}$$

$$\left(\frac{\partial \phi}{\partial x}\right)_i = \frac{\phi_{i+1} - \phi_{i-1}}{2\Delta x} + O(\Delta x^2) \tag{4.34}$$

Therefore, this proves that the error decreases as Δx for FDS and BDS, and as Δx^2 for CDS. In other terms, FDS and BDS are first-order accurate, whilst CDS is second-order accurate.

Approximations of the second derivative

As already mentioned, an approximation should also be found for the second derivatives, which typically describe the diffusion terms in fluid dynamics. The same approach can be adopted, summing equation (4.25) and (4.26), so that:

$$\left(\frac{\partial^2 \phi}{\partial x^2}\right)_i = \frac{\phi_{i+1} - 2\phi_i + \phi_{i-1}}{\Delta x^2} + O(\Delta x^2) \tag{4.35}$$

that is second-order accurate.

The same expressions may be derived by means of the polynomial fitting method. In this case, it is always possible to improve the accuracy increasing the stencil, i.e. including more data points (for instance, x_{i+2} or x_{i-2}), and the degree of the interpolating polynomial. Naturally, this not only makes the expressions more complex, but the high-order schemes also suffer from numerical instability, causing possible and undesirable oscillations of the numerical solution.

Implementation of boundary conditions

As in most of CFD applications, the physical model developed in this work is mathematically described by a boundary-value problem, i.e. a problem modeled by a set of partial differential equations for which additional constraints are required at the boundaries. In other terms, the resolution needs the treatment of a well-posed problem, for which the solution exists and is unique, and it depends continuously upon the initial and boundary conditions [69]. The implementation of a CDS at the boundaries is not allowed, because of the lack of grid points on one of the two sides. Boundary conditions thus require

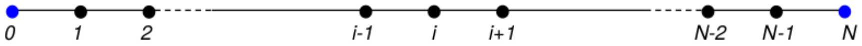

Figure 4.5: FDM: computational grid on a 1D geometric domain. Boundary conditions at x_0 and x_N require a special treatment. Credits: [67].

one-sided finite differences, such as forward and backward schemes:

$$\left(\frac{\partial \phi}{\partial x}\right)_0 \approx \frac{\phi_1 - \phi_0}{x_1 - x_0} \tag{4.36}$$

$$\left(\frac{\partial \phi}{\partial x}\right)_N \approx \frac{\phi_N - \phi_{N-1}}{x_N - x_{N-1}} \tag{4.37}$$

These are first-order accurate, but high-order approximations can be obtained for both first and second derivatives using the polynomial fitting technique [67]. These and other schemes can be used to represent the boundary conditions and, normally, two forms are given. The *Dirichlet boundary condition* provides the value of the solution at the boundaries:

$$\phi_0 = \phi_L \tag{4.38}$$

$$\phi_N = \phi_R \tag{4.39}$$

Instead, the *Neumann boundary condition* provides the gradient of the solution at the boundary. Assuming, as an example, that a Dirichlet condition is set at the left boundary and a Neumann condition at the right boundary, it results:

$$\phi_0 = \phi_L \tag{4.40}$$

$$\left(\frac{\partial \phi}{\partial x}\right)_N = k \tag{4.41}$$

where ϕ_L and k are known. Hence, the number of unknowns depends on the type of boundary conditions provided: the Neumann condition implies indeed an additional unknown, because the computation of ϕ_N is required.

The FDM applied to the swelling problem

All these concepts have been applied to the differential equations describing the physical model presented in Section 3.2.2. In particular, the model for swelling materials is governed by equations (3.87) and (3.99):

$$\frac{\partial U}{\partial t} + U\frac{\partial v_s}{\partial y} + v_s\frac{\partial U}{\partial y} = 0 \tag{4.42}$$

$$\frac{\partial T}{\partial t} - \nu\frac{\partial^2 T}{\partial y^2} = 0 \tag{4.43}$$

These are partial differential equations (PDE) because the problem involves functions of two variables, t and y. Therefore, a space-time discretization is required and the discrete equations can be obtained, in the simplest way, by means of the *Forward Time Centered Space* (FTCS) scheme. It consists in a forward Euler (or explicit Euler) scheme for the discretization in time and a central difference scheme for the discretization in space:

$$\frac{U_j^{n+1} - U_j^n}{\Delta t} + U_j^n \frac{(v_s)_{j+1}^n - (v_s)_{j-1}^n}{2\Delta y} + (v_s)_j^n \frac{U_{j+1}^n - U_{j-1}^n}{2\Delta y} = 0 \tag{4.44}$$

$$\frac{T_j^{n+1} - T_j^n}{\Delta t} - \frac{T_{j+1} - 2T_j + T_{j-1}}{\Delta y^2} = 0 \tag{4.45}$$

where n is the index of grid in time t, while i is the index of grid in space y. Transposing the only unknown for a given stepping time:

$$U_j^{n+1} = U_j^n - \frac{1}{2}\frac{\Delta t}{\Delta y}\Big[(v_s)_{j+1}^n - (v_s)_{j-1}^n\Big]U_j^n - \frac{1}{2}\frac{\Delta t}{\Delta y}(v_s)_j^n(U_{j+1}^n - U_{j-1}^n) \tag{4.46}$$

$$T_j^{n+1} = T_j^n + \frac{\Delta t}{\Delta y^2}\Bigg(T_{j+1} - 2T_j + T_{j-1}\Bigg) = 0 \tag{4.47}$$

These are thereby the discretized equations, solved to describe the thermal expansion.

Extension to a 2D domain

In view of a future implementation within ARGO, the code developed in the MATLAB environment has been improved in order to manage a two-dimensional domain of computation (Figure 4.6). However, it is important to clarify again that, since experimental tests of Sakraker [7] provided information about swelling only along the y-direction, it is not possible to model and test the material behaviour along x yet. Hence, the following equations have been implemented within the MATLAB code but, for the moment, the terms related to the second direction have been rendered inactive, imposing $u_s = 0$. Therefore, the results given in the next chapter, will show indeed a material response only along the y-direction.

The 2D convection equation can be directly derived from equation (3.86) and it is given by:

$$\frac{\partial U}{\partial t} + U\left(\frac{\partial u_s}{\partial x} + \frac{\partial v_s}{\partial y}\right) + \left(u_s\frac{\partial U}{\partial x} + v_s\frac{\partial U}{\partial y}\right) = 0 \tag{4.48}$$

Applying the FTCS scheme, the discretized form is:

$$\begin{aligned}\frac{U_{i,j}^{n+1} - U_{i,j}^n}{\Delta t} + U_{i,j}^n\left[\frac{(u_s)_{i+1}^n - (u_s)_{i-1}^n}{2\Delta x} + \frac{(v_s)_{j+1}^n - (v_s)_{j-1}^n}{2\Delta y}\right] + \\ + \left[(u_s)_i^n\frac{U_{i+1,j}^n - U_{i-1,j}^n}{2\Delta x} + (v_s)_j^n\frac{U_{i,j+1}^n - U_{i,j-1}^n}{2\Delta y}\right] = 0\end{aligned} \tag{4.49}$$

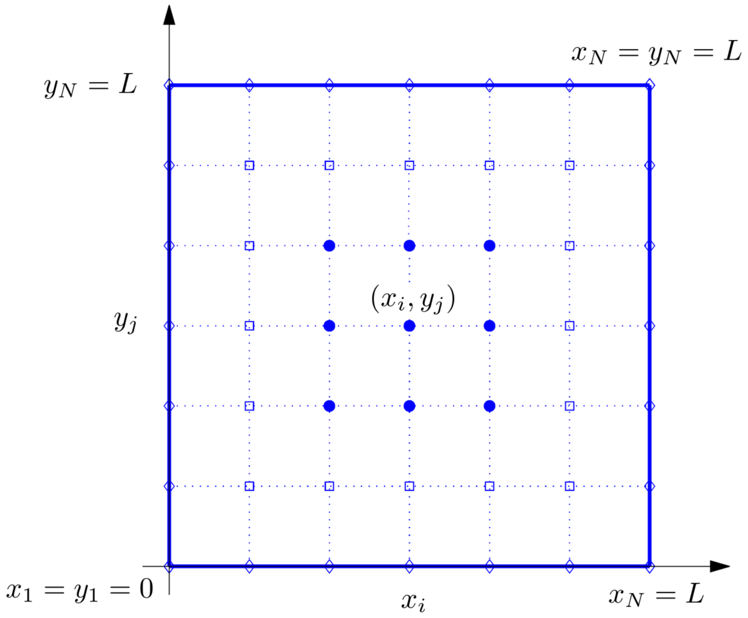

Figure 4.6: FDM: two-dimensional square domain, discretized in x_i and y_j computational nodes.

Finally, the unknown at the step $n+1$ is transposed as follows:

$$\begin{aligned} U_{i,j}^{n+1} =& U_{i,j}^{n} - \frac{1}{2}\frac{\Delta t}{\Delta x}\left[(u_s)_{i+1}^n - (u_s)_{i-1}^n\right]U_{i,j}^n - \frac{1}{2}\frac{\Delta t}{\Delta y}\left[(v_s)_{j+1}^n - (v_s)_{j-1}^n\right]U_{i,j}^n + \\ & - \frac{1}{2}\frac{\Delta t}{\Delta x}(u_s)_i^n\left(U_{i+1,j}^n - U_{i-1,j}^n\right) - \frac{1}{2}\frac{\Delta t}{\Delta y}(v_s)_j^n\left(U_{i,j+1}^n - U_{i,j-1}^n\right) = 0 \end{aligned} \tag{4.50}$$

Chapter 5

Results

In this chapter, the results of numerical simulations are presented, serving a dual purpose of testing the new routine implemented within Argo for the computation of pyrolysis gases at equilibrium and analyzing the physical model developed for the simulation of swelling materials. Hence, a first series of test cases and ablation simulations were performed by means of Argo, followed by a simulation of the swelling mechanism coded in the Matlab platform.

5.1 Adiabatic 0D reactor

Pyrolysis of TACOT

A first simple test case was studied by means of the *ReactorZeroD* solver, in order to verify the new implemented tool. This is one of the simplest solvers available in the *DGAblation* module of Argo: only the evolution of the species is solved, assuming adiabatic conditions, no convection and no diffusion [11]. Therefore, the only heat source comes from pyrolysis. An unsteady simulation was performed, using an explicit scheme for the temporal discretization and a time step equal to $\Delta t = 10^{-4}$ s. A total time of 0.1 seconds was simulated, since a preliminary analysis showed that is sufficient to reach the steady state.

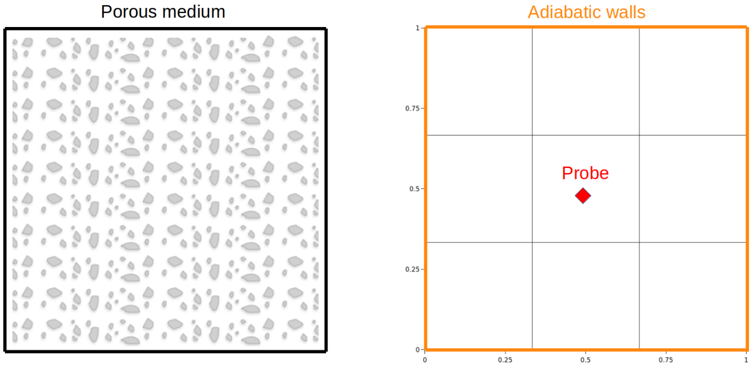

Figure 5.1: Adiabatic 0D reactor: domain of computation (left) and mesh (right).

The domain of computation is a square containing the porous medium, discretized in 9 square elements to form the computational grid (Figure 5.1) and all the boundaries are treated as adiabatic walls. As regards the solid phase, the TACOT (*Theoretical Ablative Composite for Open Testing*) material was simulated; it is a fictitious TPM created from literature data in order to mimic low-density carbon-phenolic charring ablators, such as PICA. TACOT is characterized by a virgin density of 280 kg m^{-3}, with a porosity equal to 0.8. The permeability starts from $1.60 \cdot 10^{-11}$ m^2 and it evolves with porosity according to the Carman-Kozeny model. The tortuosity of the virgin material is equal to 1.2, while the initial radius of the carbon fibers is $r_0 = 5$ μm. As regards the thermal properties, heat capacity and thermal conductivity are fitted as functions of temperature using the NASA-9 polynomial interpolation and they are shown in Figure 5.2 for the virgin and charred materials.

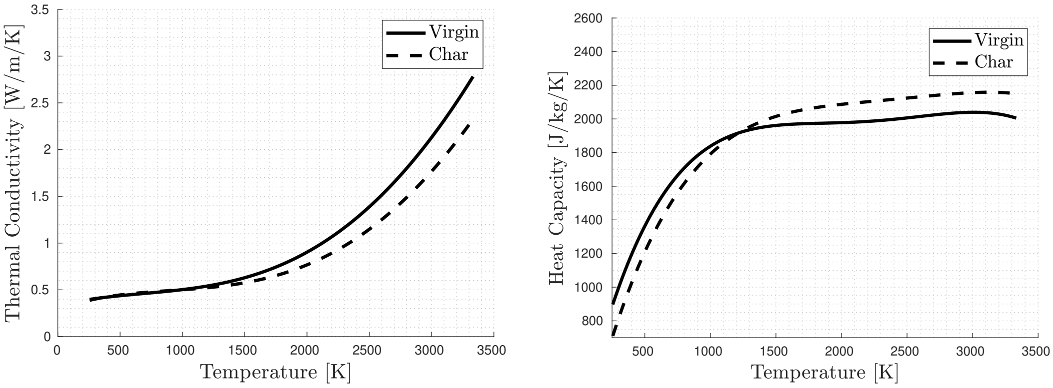

Figure 5.2: Thermal properties of TACOT, expressed as a function of temperature.

For the fluid phase, a list of 7 species was considered: CO_2, CO, C_6H_6, C_6H_5OH, CH_4, H_2O, H_2. Finally, as explained in Section 3.2.1, the thermal degradation of two fictitious compounds is described by means of an Arrhenius type law [13]:

$$\frac{\partial}{\partial t}\langle \rho_I \rangle = -A_{0,I}\langle \rho_I^v \rangle \exp\Big(\frac{-E_{a,I}}{\mathcal{R}T}\Big)\Big(\frac{\langle \rho_I \rangle - \langle \rho_I^c \rangle}{\langle \rho_I^v \rangle}\Big)^{n_I} \tag{5.1}$$

The coefficients are listed in Table 5.1, while the elemental composition of pyrolysis gases is given in Table 5.2. As initial condition, a uniform field was set, with an initial pressure of 101325 Pa and a temperature of 1500 K, that is enough high to activate pyrolysis reactions. Furthermore, the chemical composition of the mixture was initialized at thermochemical equilibrium, computed by Mutation++.

Table 5.1: Arrhenius law coefficients for the description of pyrolysis (test case of TACOT).

	A_0 [s^{-1}]	$E_a/\mathcal{R}$ [K]	n
Reaction R1	1.2e4	8555	3.00
Reaction R2	4.48e9	20444	3.00

Two simulations were performed: in the first one, a pre-fixed composition was set for the pyrolysis gas while, in the second one, the new implemented routine was tested calling Mutation++ to compute the pyrolysis gas composition at equilibrium conditions, starting from its elemental composition specified in Table 5.2. A probe was located in the middle of the domain, as shown in Figure 5.1, in order to track the time evolution of the quantities. The results are plotted in Figure 5.3 and 5.4.

Table 5.2: Elemental composition of pyrolysis gases (test case of TACOT).

	C	H	O
Mole fraction	0.206	0.679	0.115

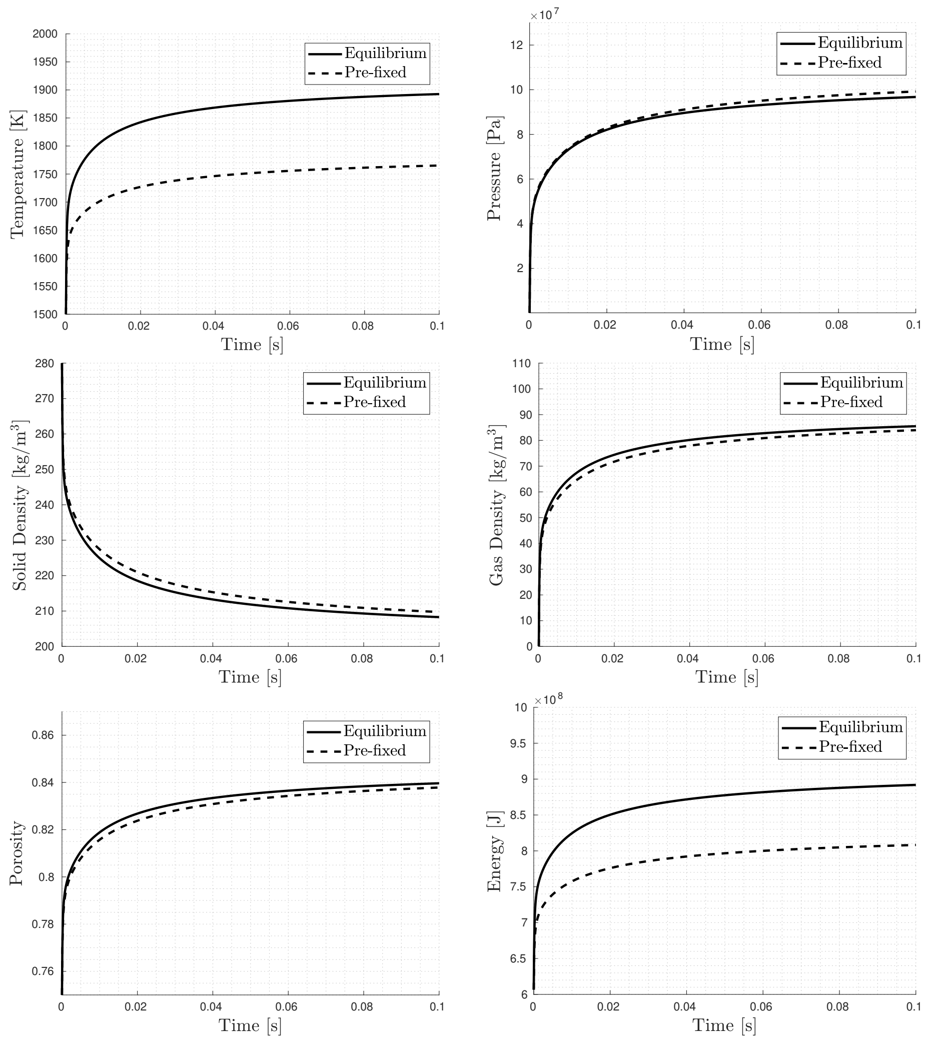

Figure 5.3: Results of the pyrolysis of TACOT, simulated by means of the adiabatic 0D reactor solver.

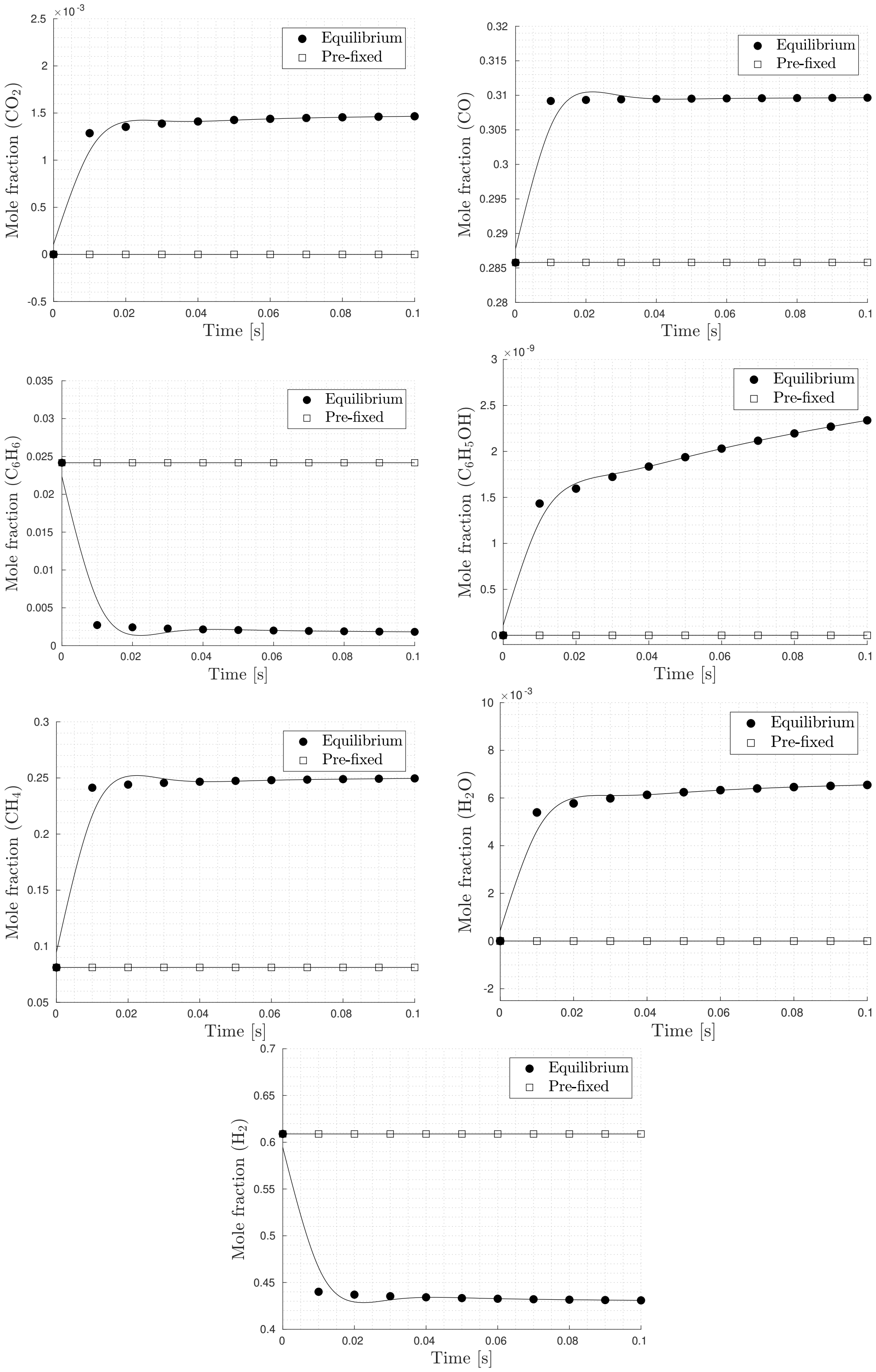

Figure 5.4: Comparison between pre-fixed and equilibrium mole fractions of each chemical species, during pyrolysis of TACOT.

The comparison shows that the main difference is in temperature profile and, as a consequence, in energy evolution too; in particular, the pre-fixed composition specified for this test case produced an underestimation of the temperature reached at the steady state in the middle of the domain. Furthermore, another interesting result is in the discrepancy of chemical composition of the mixture, shown in Figure 5.4, in terms of species mole fractions. As expected, the new routine implemented within ARGO allowed to compute the composition of pyrolysis gases on the basis of the local temperature and pressure (at equilibrium) rather than fixing the same composition for the whole simulation, as had been done so far. Therefore, this is a more reasonable way of treating the production of pyrolysis gases and it represents a further step towards the improvement of the numerical simulations of charring ablators.

Pyrolysis of another material

The same test case was replicated for another charring ablator, taken from the database of VKI. It has an average density of 430 kg m^{-3} and a porosity approximately equal to 0.6. The initial permeability is equal to $2.31 \cdot 10^{-13}$ m^2, the tortuosity is 1.2 and the initial radius of the carbon fibers is equal to $r_0 = 5$ μm. The same list of 7 chemical species was considered, while the decomposition of three fictitious compounds was studied, through three pyrolysis reactions. The coefficients of the Arrhenius law describing the decomposition of the resin are listed in Table 5.3, while the elemental composition of pyrolysis gases is shown in Table 5.4.

Table 5.3: Arrhenius law coefficients for the description of pyrolysis (test case of a charring ablator from database of VKI).

	A_0 [s^{-1}]	$E_a/\mathcal{R}$ [K]	n
Reaction R1	6.667e4	8577	5.00
Reaction R2	8.256e5	13302	2.90
Reaction R3	9.499e3	11952	2.20

Table 5.4: Elemental composition of pyrolysis gases (test case of a charring ablator from database of VKI).

	C	H	O
Mole fraction	0.125	0.125	0.750

The results are given in Figure 5.5 and 5.6, and similar conclusions can be drawn.

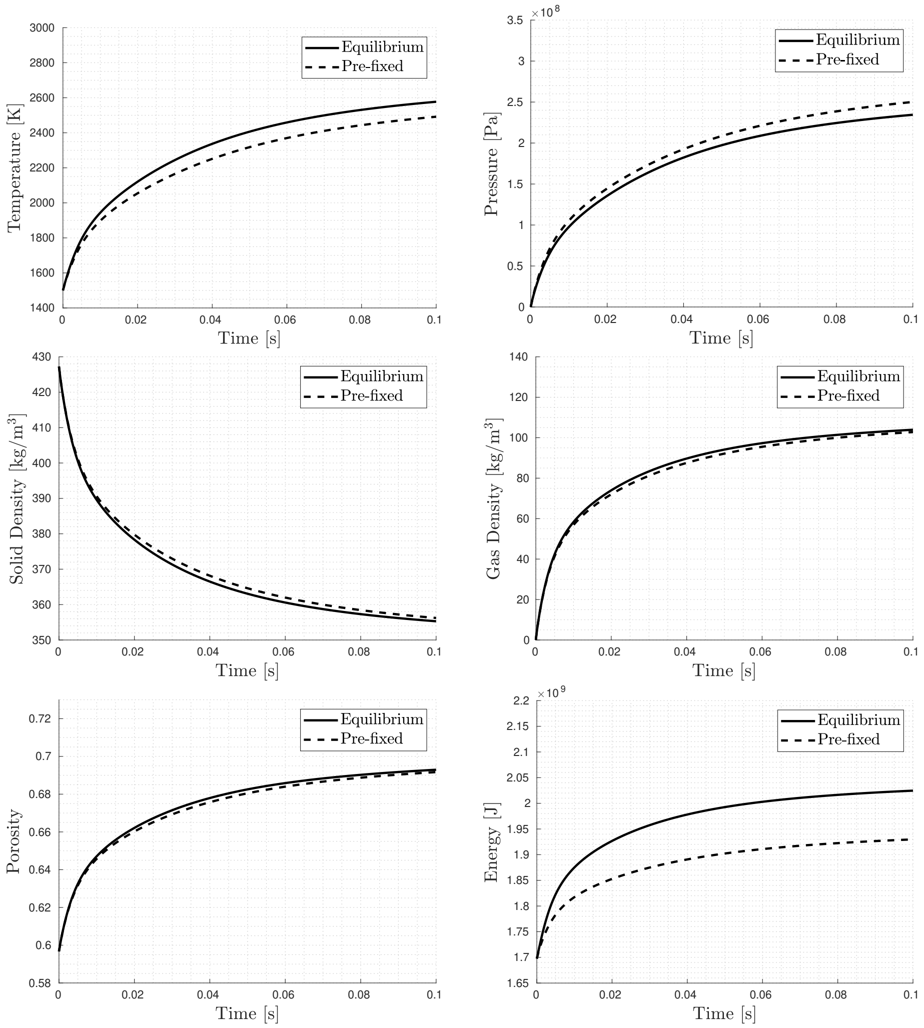

Figure 5.5: Results of the pyrolysis of another charring ablator, simulated by means of the adiabatic 0D reactor solver.

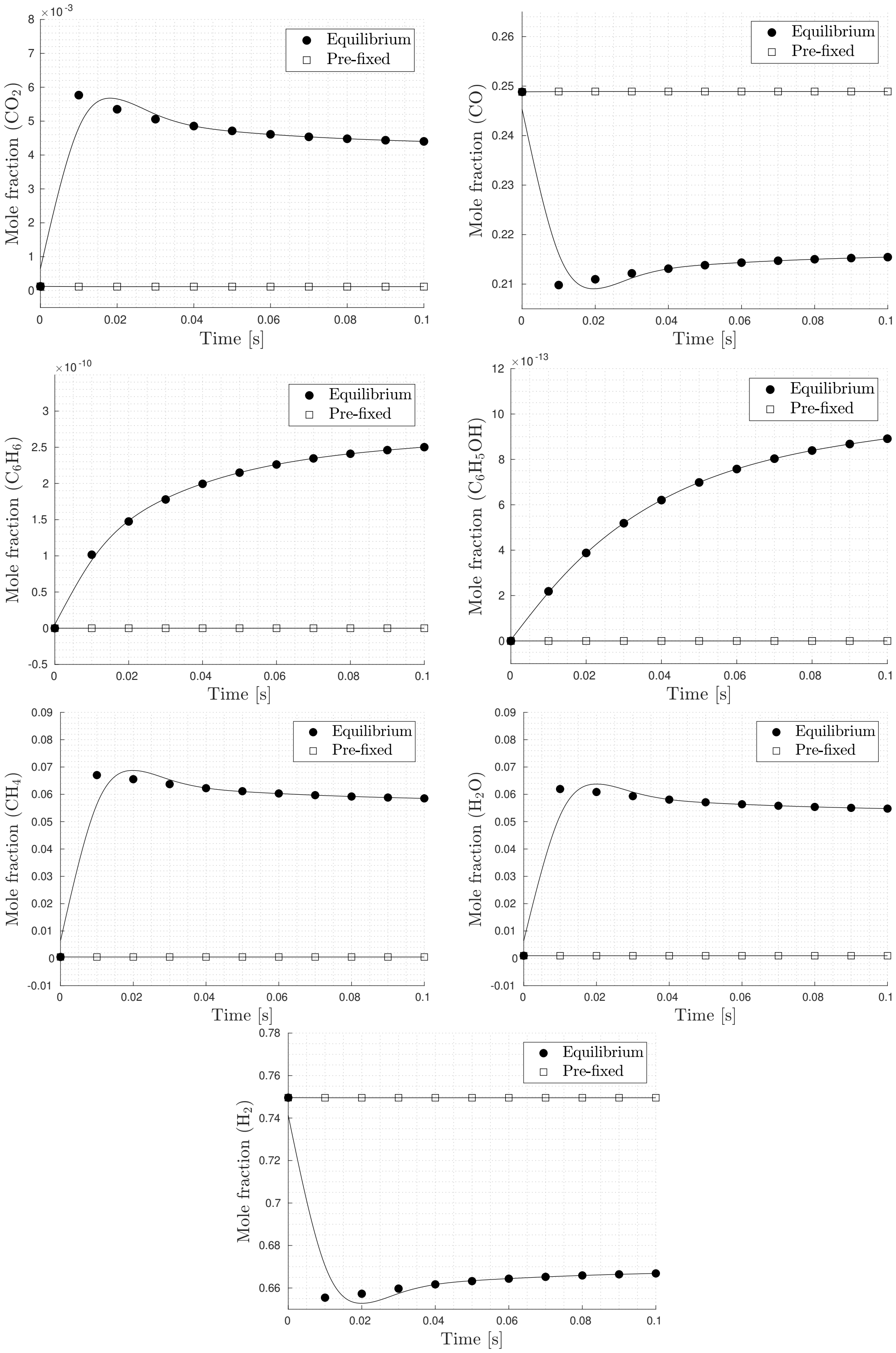

Figure 5.6: Comparison between pre-fixed and equilibrium mole fractions of each chemical species, during pyrolysis of another charring ablator.

5.2 Non-charring ablator

The previous test cases were studied by means of a simplified solver, neglecting convection and diffusion and solving only the thermal decomposition. With a view to include all the transport phenomena, the following simulations were performed using the Navier-Stokes solver of ARGO, presented in Section 3.1.2. The ablation of a carbon preform TPM was first analyzed. Pyrolysis was not included yet because a non-charring ablator was considered in this first simulation, for the purpose of studying only the material recession due to oxidation of the carbon fibers and as a repeatability test of the simulation performed by Schrooyen et al. [43]. An axisymmetric simulation was performed, due to the hemispherical geometry of the sample. Furthermore, 10 seconds were simulated in total, in order to reach the quasi-steady state. A sketch of the simulation in Plasmatron conditions is shown in Figure 5.7.

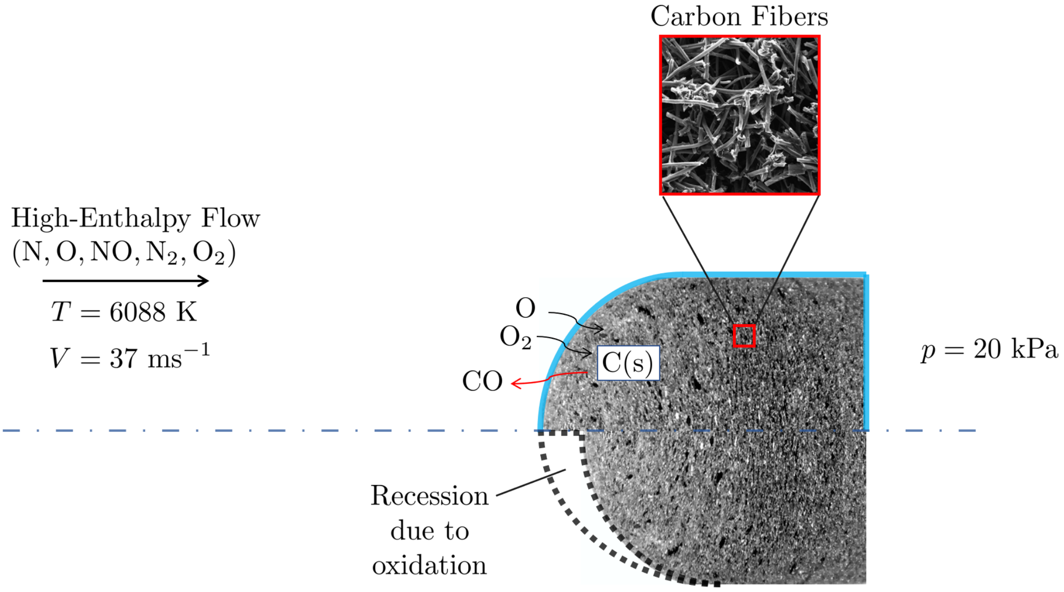

Figure 5.7: Scheme of the simulation of the carbon preform ablator in Plasmatron conditions.

The domain of computation is shown in Figure 5.8. The hemispherical sample has a diameter equal to 25 mm and it is located at a distance of 15 cm from the subsonic inlet. According to Schrooyen et al. [42], a previous analysis had proved that just 13 cm are sufficient to correctly solve the flow field. The slip wall is far enough too, in order to avoid the blockage effect. Finally, the adiabatic walls of the holder extend to 25 mm from the sample up to the subsonic outlet.

The mesh consists of 4925 nodes and 6003 elements. A 1st order Lagrangian polynomial interpolation ($p = 1$) is used inside each element, so that a 2nd order of accuracy ($p + 1$) is investigated using DGM. The computational grid is shown in Figure 5.8 and the boundary conditions are listed in Table 5.5.

Table 5.5: Boundary conditions.

Subsonic inlet	$U_{\text{inlet}} = 37\ \text{ms}^{-1}$, $T_{\text{inlet}} = 6088$ K $Y_{\text{inlet}} =$ (N:0.26, O:0.23, NO:0.0039, N_2:0.50, O_2:6*e*-5, CO:0.0)
Subsonic outlet	$p_{\text{outlet}} = 20\ 000$ Pa

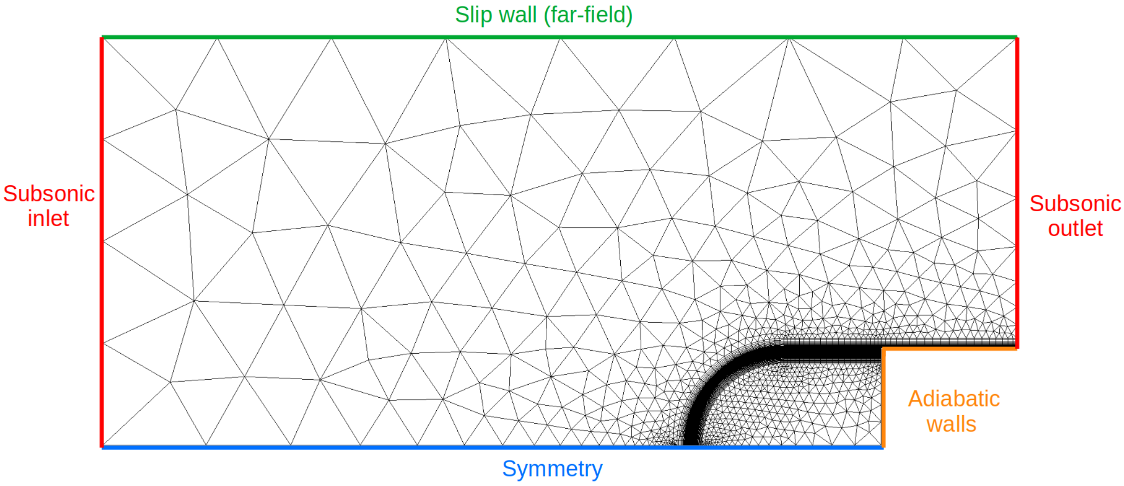

Figure 5.8: Computational grid and boundary conditions.

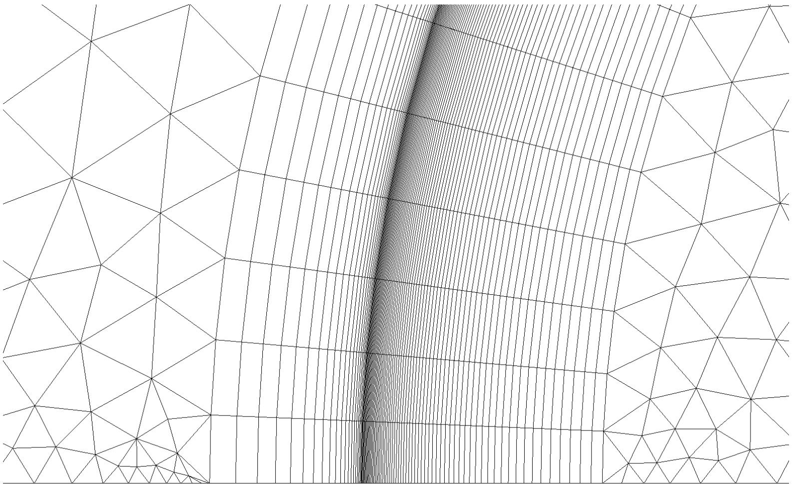

Figure 5.9: Prism layers at the interface of the two regions.

Two prism layers have been generated for the boundary layer and the material interface (Figure 5.9). In particular, the first cell of the interface has a thickness of 10 μm, in order to correctly track the material recession. In the *Unified approach*, a hyperbolic tangent is used to gradually describe the transition from the pure fluid region to the porous medium (Figure 5.10(a)). An initial thickness of $\varepsilon_\Phi = 0.2$ mm has been set, considering that a lower value may increase the risk of numerical instabilities. Spurious oscillations may indeed occur if the transition region is too sharp, as illustrated in Figure 5.11. Specifically, according to Schrooyen [11] the smoothing distance ε_Φ should satisfy the relation:

$$\varepsilon_\Phi > 3\frac{h}{p} \approx 30\ \mu\text{m}$$

where $h \approx 10\ \mu$m is the local mesh size and $p = 1$ is the order of the Lagrangian polynomial interpolation. Moreover, the mesh size has been increased at the outlet of the computational domain and a *sponge layer* has been set, in order to damp the oscillations due to non-physical wave reflections, by means of a source term which penalizes the difference between the local solution and a reference one (Figure 5.12). In this way, the flow fluctuations due to the boundaries reflection have been successfully removed. Another strategy requires to locally decrease the order of accuracy, even if it was not necessary in this work.

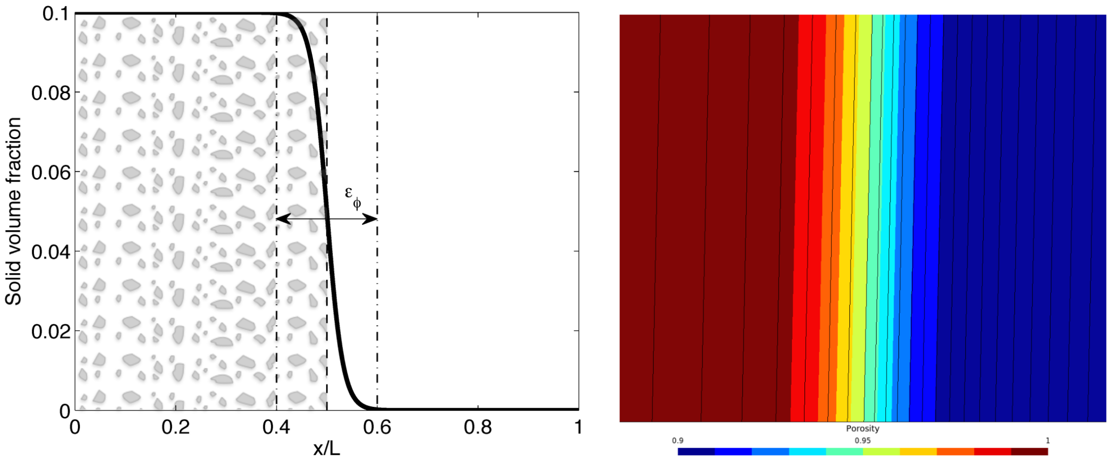

(a) The transition is described by means of a hyperbolic tangent function.

(b) Initial porosity field in the transition zone.

Figure 5.10: The physical quantities have to evolve continuously at the interface.

Considering the unsteady nature of the simulation, the time step has been gradually increased according to Table 5.6 and Figure 5.13. In fact, even though an implicit strategy has been chosen for the temporal discretization, the resolution of an unsteady flow, as well as the non-linearities of the equations, may apply restrictions to the choice of the maximum time step. In particular, it is essential to use very small Δt for the first steps, in order to avoid convergence issues and to reach an acceptable degree of accuracy too. A tolerance of 10^{-4} has been set for the residuals, with a maximum number of iterations equal to 20.

Six chemical species were considered: N, O, NO, N_2, O_2 from Air5 chemistry model, and CO as product of oxidation. The other ablation mechanisms, such as phase changes and spallation are not taken into account [43]. ARGO is coupled with MUTATION++,

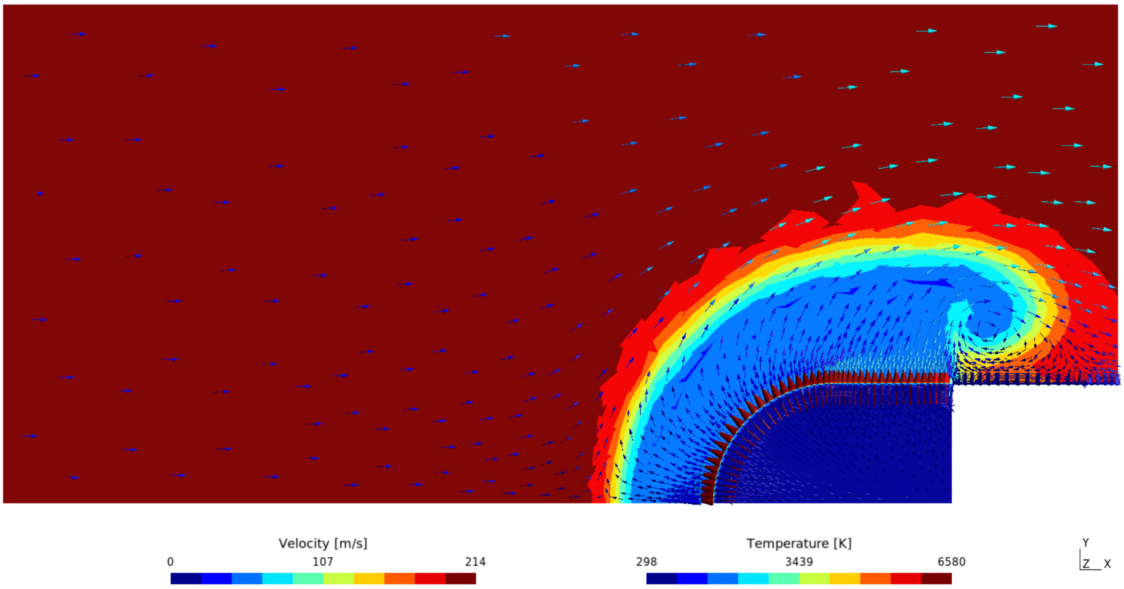

Figure 5.11: Spurious oscillations due to a too sharp transition region.

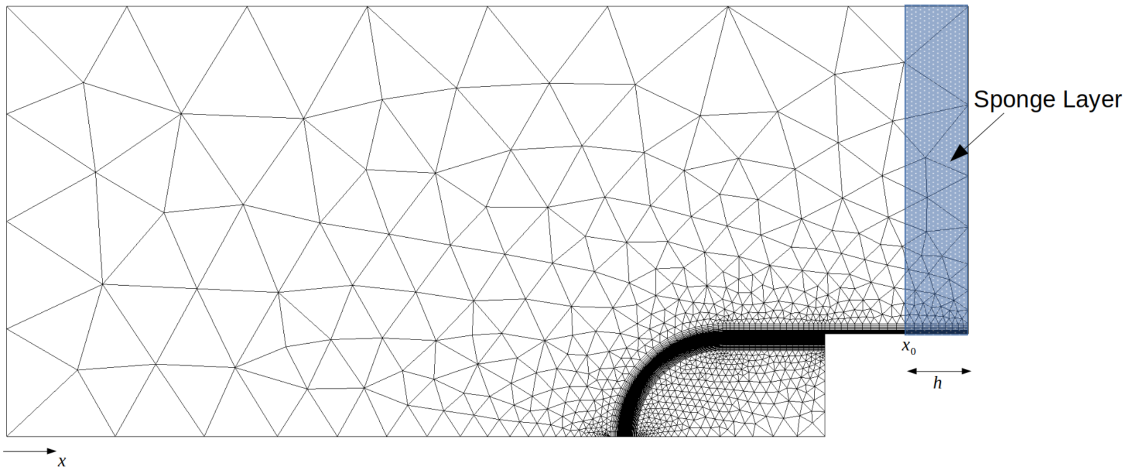

Figure 5.12: Sponge layer at the outlet to damp the numerical oscillations.

Table 5.6: Non-charring ablator: tabulated time step.

Δt [s]	1e-8	1e-7	5e-7	1e-6	1e-5	2.5e-5	5e-5	1e-4	2.5e-4	5e-4
Final time for Δt [s]	1e-7	1e-6	5e-5	5e-4	5e-3	0.01	0.05	0.1	0.5	10

which provides the thermodynamic and transport properties, and the reaction rates for

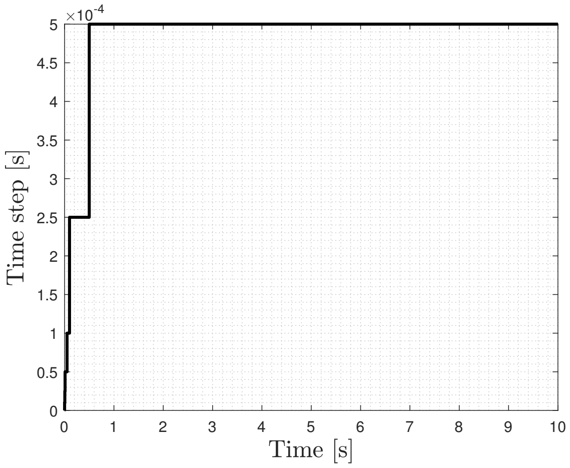

Figure 5.13: Non-charring ablator: time stepping during the simulation.

the fluid phase [11]. In particular, the computation of the thermodynamic properties is based on the NASA-9 polynomials database, while the transport properties are computed through the Chapman-Enskog method. As regards the chemical reactions, the chemistry model of Park et al. [70] was taken as a reference and five homogeneous reactions for air were included. They are listed in Table 5.7. Furthermore, a mass diffusion model based on a constant Schmidt number has been set. Although it provides results less accurate than the multicomponent model, it allowed to solve some convergence issues. Some chemical species, characterized by a low molecular mass, exhibited indeed a diffusion so fast that a too small time step would have been needed. Therefore, a Sc = 1 has been set, considering that it is between 0.6 and 1 for air at a temperature of 300-6000 K [71].

Table 5.7: Non-charring ablator: homogeneous reactions included in the reaction mechanisms database of MUTATION++.

Homogeneous reactions	
Dissociation reactions	Exchange reactions
$N_2 + M \rightleftharpoons 2N + M$	$NO + O \rightleftharpoons N + O_2$
$O_2 + M \rightleftharpoons 2O + M$	$N_2 + O \rightleftharpoons NO + N$
$NO + M \rightleftharpoons N + O + M$	

The carbon preform TPM is characterized by an intrinsic density of 1800 kg m^{-3}, with a volum fraction of 0.1. Therefore, the material has a nominal average density of 180 kg m^{-3}, with a porosity of 0.9. The thermal conductivity is constant and equal to 0.5 W $m^{-1}K^{-1}$, while the permeability evolves with the void fraction according to the Carman-Kozeny model, starting from an initial value of $1.45 \cdot 10^{-10}$ m^2. Finally, the initial radius of the carbon fibers is $r_0 = 5$ μm and it is expected to decrease because of material oxidation. A cylindrical model for the fibers is considered and a radial and uniform recession is assumed for the fiber oxidation (Figure 5.14).

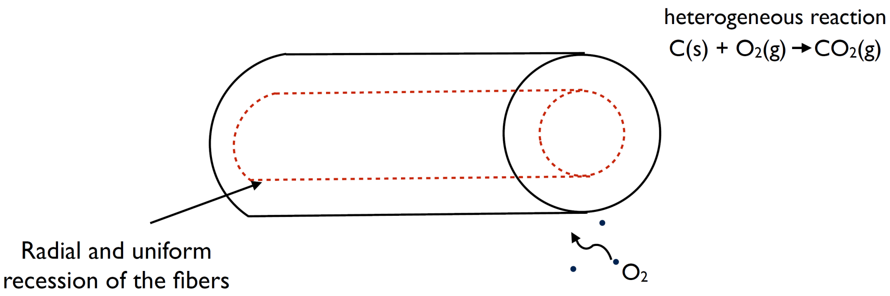

Figure 5.14: Recession model. The carbon fibers are modeled as cylinders receding in a radial and uniform way.

Two irreversible first order heterogeneous oxidation reactions were included. Both of them imply the production of CO and, theoretically, CO_2 too. However, when the temperature exceeds 800 K, oxidation is dominated by the production of CO, and CO_2 can thus be neglected. The oxidation reactions are shown in Table 5.8 and, as already explained in Section 3.1.2, their forward reaction rates are given by an Arrhenius type law [11]:

$$k_f^{i,C(s)} = AT^n \exp\left(\frac{-E_a}{\mathcal{R}T}\right) \tag{5.2}$$

Instead, since their backward reaction rates are very small, the reverse reactions were neglected [70].

Table 5.8: Non-charring ablator: heterogeneous reactions included in the input file of ARGO in order to describe the oxidation of the carbon fibers.

Oxidation reactions		A	$E_a/\mathcal{R}$	n
$O_2 + 2C(s) \rightarrow 2CO$	O_2 + 2FibersC → 2CO	5.73	$9.65e3$	0.5
$O + C(s) \rightarrow CO$	O + FibersC → CO	3.22	0	0.5

The evolution of the species mass fraction along the stagnation line is shown in Figure 5.15. The initial mass fractions are computed by MUTATION++ assuming the equilibrium. The pure fluid region is initialized at $T = 6088$ K, so that air is totally dissociated there. Instead, the initial temperature of the porous medium is 298 K, so that air is completely recombined within the material. A gradual transition is applied to the temperature profile at the interface, so that the initial temperature of the wall is $T_w = 537$ K. The production of CO occurs at the interface after few steps and a peak is observed in Figure 5.15(b), mainly due to the reaction between O and the carbon fibers. Once it has been generated, CO is assumed to be frozen. Within the porous medium, the fibers are attacked by O_2 molecules. The production of CO is accompanied by its convection and diffusion through the whole material. Finally, after 5 seconds a quasi-steady state is reached (Figure 5.15(d)).

Defining the interface at 50% of the nominal bulk density ($\rho_{\text{s,interf}} = 180/2$ kg m^{-3}

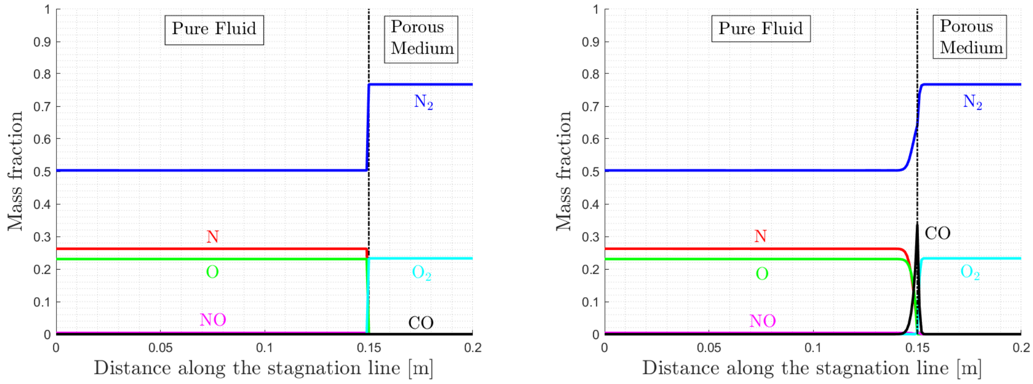

(a) $t = 0$ s (equilibrium) **(b)** $t = 0.005$ s

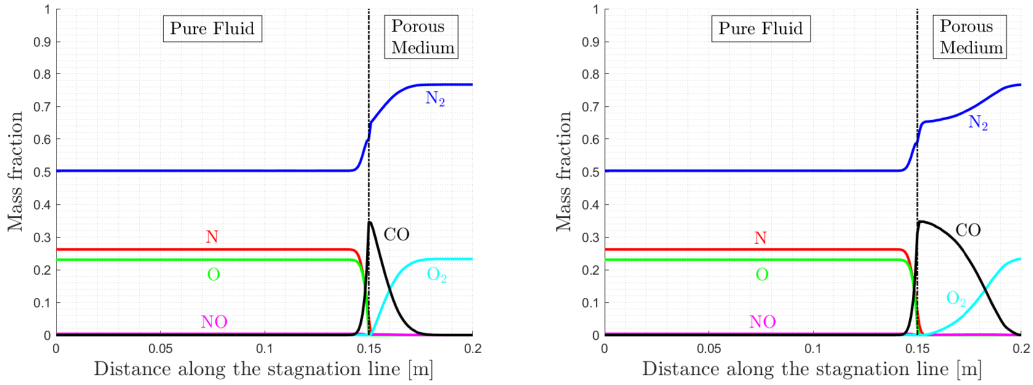

(c) $t = 0.5$ s **(d)** $t = 5.0$ s

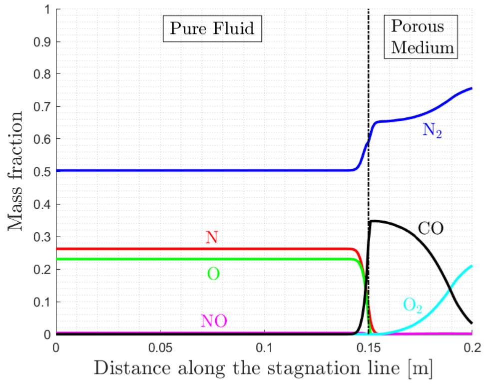

(e) $t = 10.0$ s

Figure 5.15: Non-charring ablator: evolution of the species mass fractions along the stagnation line.

= 90 kg m^{-3}), a stagnation point recession of 0.36 mm has been computed after 10 seconds (Figure 5.16(b)). The solid density profile recedes with time, but it remains constant inside the material, as evidenced by Figure 5.16(a). Therefore, the thickness of the interface transition region decreases with time, since the oxidation mainly occurs at the interface and a *surface ablation* regime is observed.

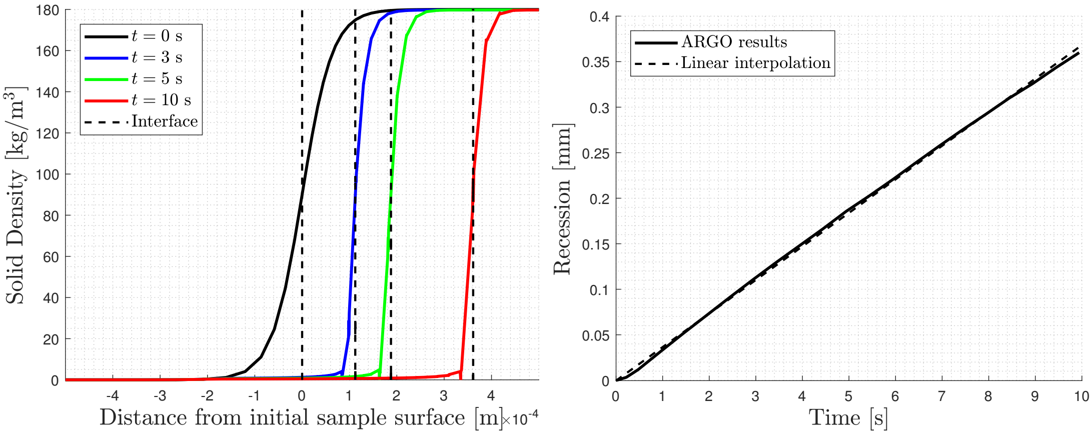

(a) Solid density along the stagnation line. **(b)** Stagnation point recession.

Figure 5.16: Non-charring ablator: stagnation point recession.

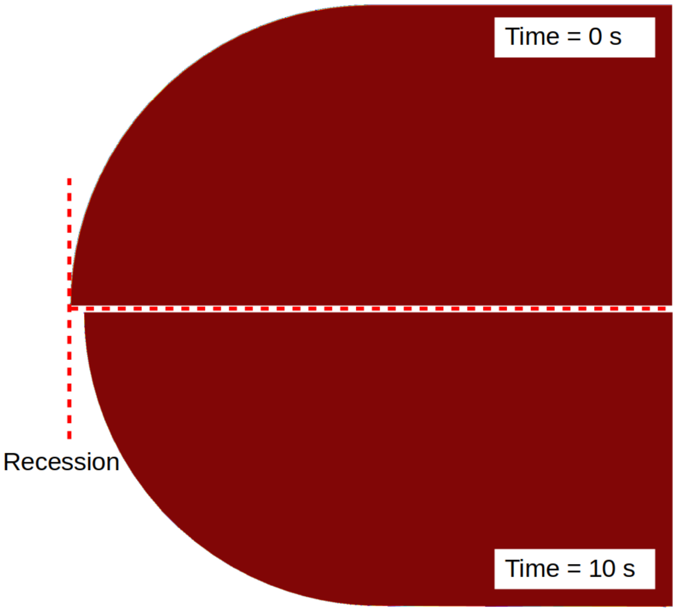

Figure 5.17: Non-charring ablator: recession of the sample after 10 seconds.

The time evolution of the stagnation point temperature is shown Figure 5.18. Starting from an initial value of 537 K, the surface temperature increases as the material is heated, reaching a value of 1900 K. Furthermore, this effect is amplified by the exothermic nature of oxidation. It is worth specifying that, in the unified approach, the wall temperature profile strongly depends on the definition of the interface, since it is obtained tracking a specific value of the solid density during post-processing. For instance, a reasonable solution could be to identify the interface with the half-value of the nominal bulk density. However, since this could result in differences in temperatures, a comparison with experimental data should be done, in order to better define the position of the solid wall. Moreover, as the transition zone becomes sharper, the tracking of the interface is less accurate, resulting in spurious oscillations in the temperature profile where the thermal gradients are very high. Finally, the temperature field after 10 seconds is shown in Figure 5.19, while the Figure 5.20 highlights a detailed view of both thermal and momentum boundary layers close to the holder. The prism layers allowed indeed to correctly capture the adiabatic temperature profile, as well as the velocity distribution.

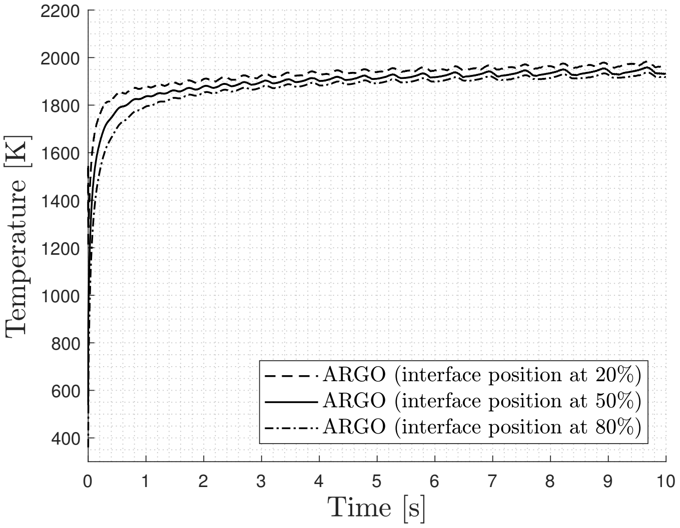

Figure 5.18: Non-charring ablator: stagnation point temperature.

A mass loss of 2% was computed after 10 seconds of exposure, corresponding to a loss of 0.3 grams. This phenomena has a good linear trend (Figure 5.21) and a mean value for the mass loss rate of 31 mg/s can be observed.

The static pressure along the stagnation line is showed after 10 seconds in Figure 5.22. The peak corresponds to the total pressure, therefore, as the Mach number is very low ($M_\infty \approx 0$), it is possible to neglect the compressible effects to exploit the Bernoulli law and verify the computed stagnation pressure:

$$p_{\infty,0} = p_{\infty,s} + K_H \frac{1}{2} \rho_\infty u_\infty^2 = 20006 \ Pa \tag{5.3}$$

where K_H is the Homann's correction factor and it accounts for the Barker effect at low Reynolds number. The simulation showed a total pressure of 20017 Pa, but the Bernoulli theory does not consider the fact that the stagnation point could be no longer on the surface material, because of the blowing effect. The Figure 5.23 shows the partial

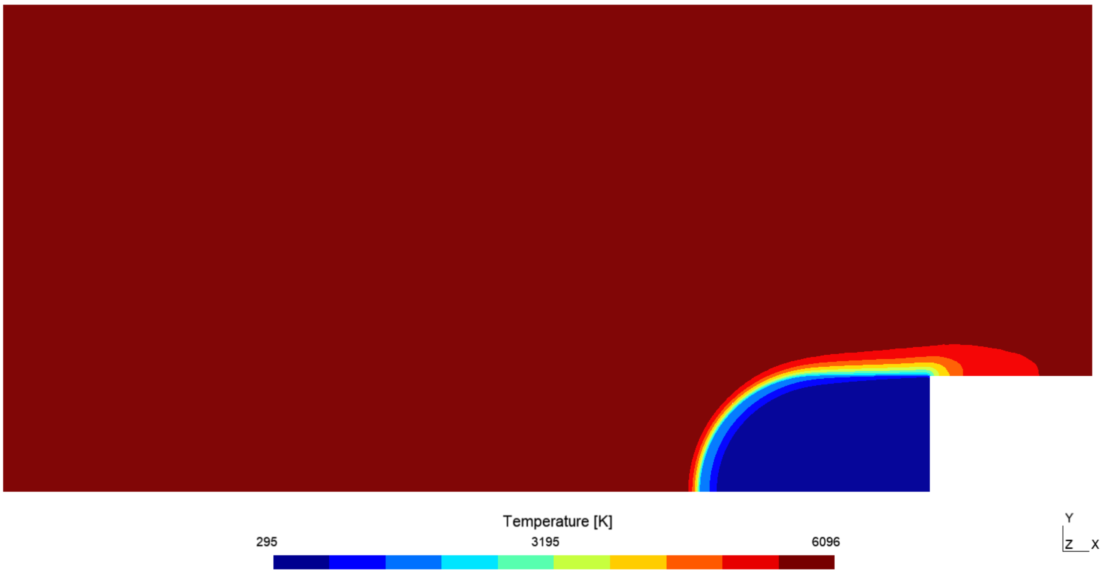

Figure 5.19: Non-charring ablator: temperature field after $t = 10$ s.

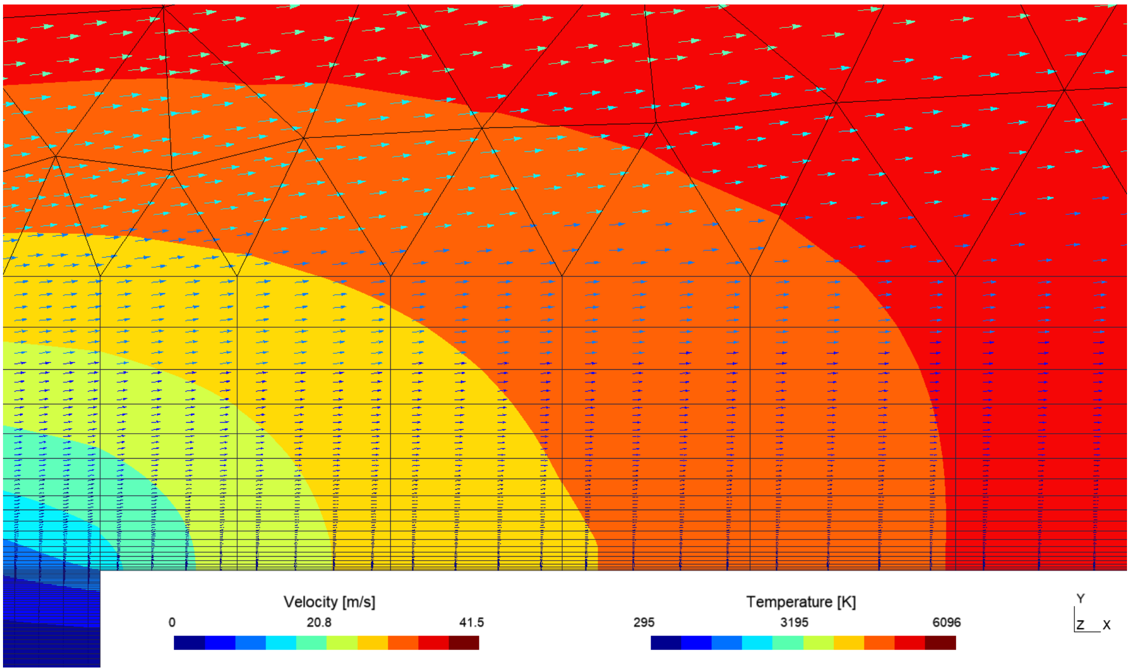

Figure 5.20: Non-charring ablator: thermal and momentum boundary layers close to the holder, after $t = 10$ s.

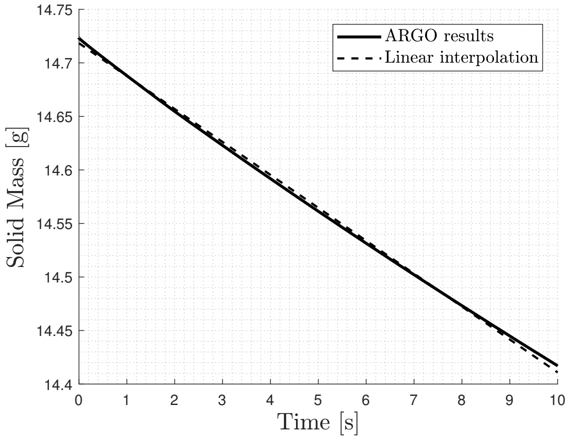

Figure 5.21: Non-charring ablator: mass loss.

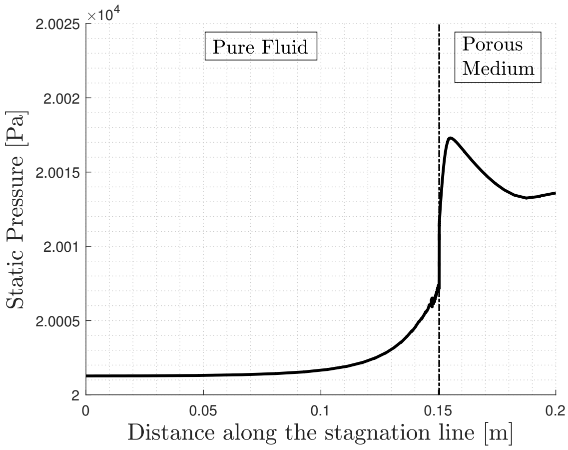

Figure 5.22: Non-charring ablator: static pressure along the stagnation line after $t = 10$ s.

pressure of CO at the steady state. The presence of carbon monoxide can be detected into the depths of the porous medium, due to convection and diffusion mechanisms. For the purpose of deducing the nature of ablation as a surface or volume phenomenon, the Thiele number can be computed [43]:

$$\mathrm{Th} = \frac{L}{\sqrt{D_{\mathrm{eff}}/S_f k_f}} = \frac{L}{l_{\mathrm{abl}}} \tag{5.4}$$

where $L = 0.025$ m is a reference length of the sample, D_{eff} is the effective diffusion coefficient and l_{abl} is the length of ablation. The latter can also be estimated as the distance between the interface and the point where the atomic oxygen is totally consumed. A value of $l_{\mathrm{abl}} \approx 150$ μm has been computed after 10 seconds, so that the Thiele number results equal to $\mathrm{Th} \approx 167 > 50$. This would prove that a surface ablation regime was established. However, it must be remembered that this estimation is strongly affected by

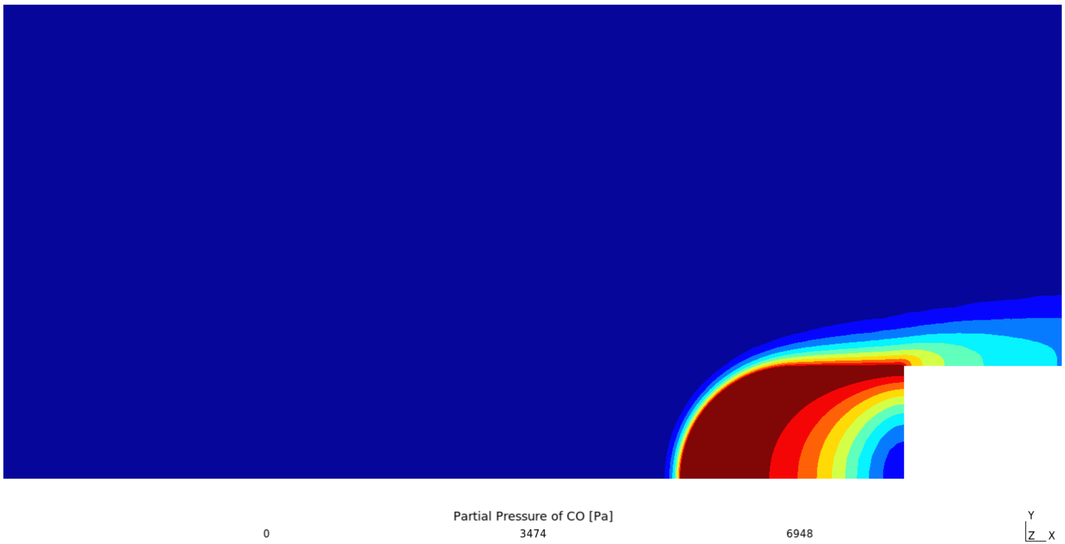

Figure 5.23: Non-charring ablator: partial pressure field of CO after $t = 10$ s.

the definition of the interface.

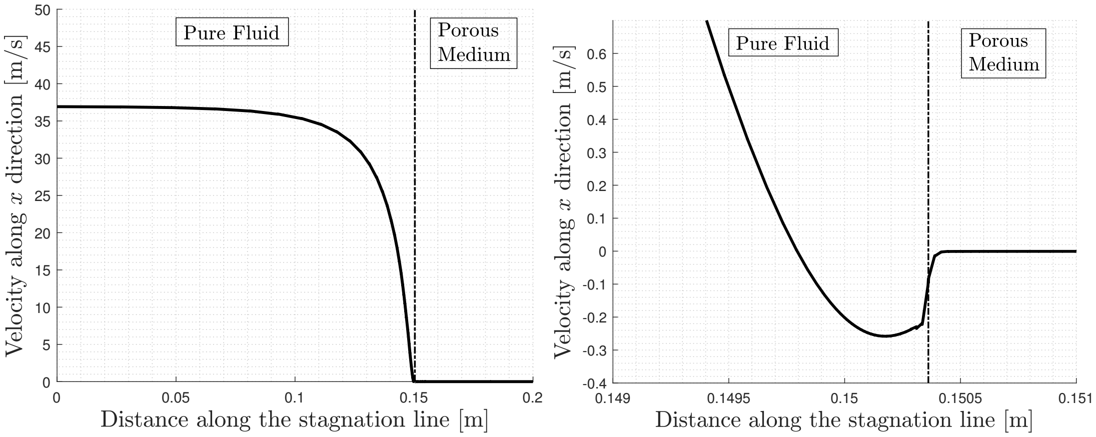

(a) Axial velocity along the stagnation line.

(b) Detailed view of the region close to the stagnation point.

Figure 5.24: Non-charring ablator: axial velocity along the stagnation line after $t = 10$ s.

The axial velocity along the stagnation line after 10 seconds can be observed in Figure 5.24. The freestream velocity is 37 m s^{-1} and it decreases as it approaches the sample. In particular, a maximum negative velocity of about 0.25 m/s is computed close to the interface, because of the blowing gas. Finally, a maximum velocity of 300 μm/s can be observed within the porous medium (Figure 5.25). This is the percolation phenomenon:

the gas slowly moves through the pore network towards the outside.

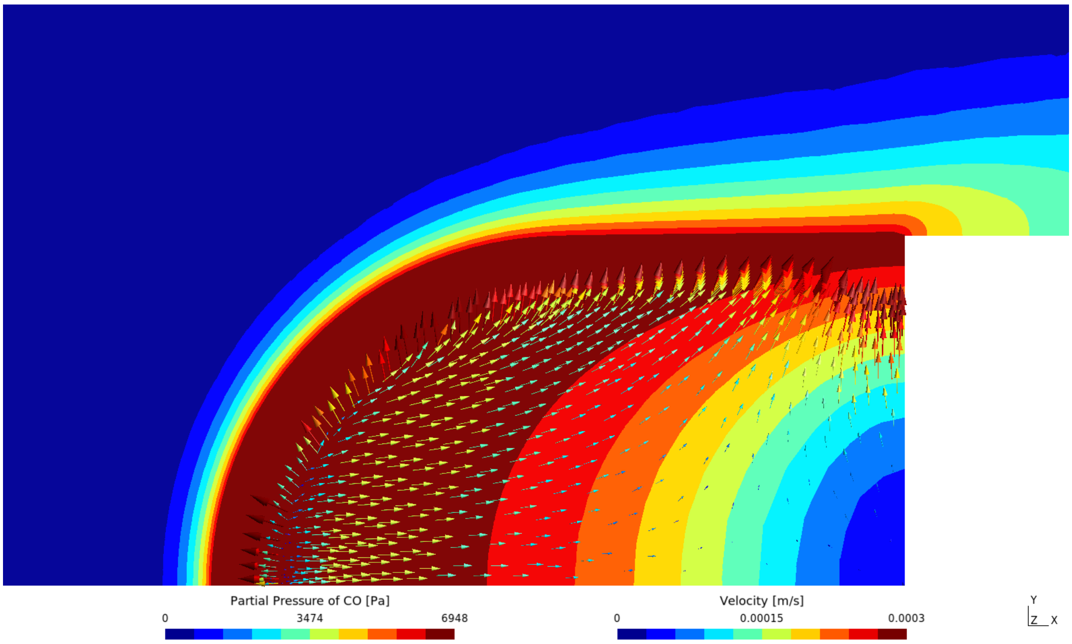

Figure 5.25: Non-charring ablator: velocity field inside the porous material ($t = 10$ s).

5.3 Charring ablator

Another Argo simulation was performed to examine the ablation of a charring TPM in Plasmatron conditions. Actually, the Argo tool is not yet ready for the full simulation of the cork-phenolic P50 of Qarman in re-entry conditions, due to the unavailability of technical data of cork-based ablators and considering also that only carbon-based materials can be treated at the moment by Argo. For these reasons, the TACOT material has once again been selected for the following analysis, for the purpose of testing, in the context of a preliminary analysis of Qarman, the implementation of the function calling Mutation++ to compute the production of pyrolysis gases at equilibrium. Moreover, considering that the inclusion of pyrolysis phenomenon implies the resolution of a stiff problem, the usage of extremely small time steps results in a very high computational cost. Therefore, a total time of 1 second has been simulated, which is enough large to study the thermal decomposition but it is not sufficient to reach the quasi-steady state in terms of material recession. A sketch of the simulation is illustrated in Figure 5.26.

As already mentioned, pyrolysis is a stiff process because it makes extremely difficult the integration of the PDEs describing this physical phenomenon. For this reason, the maximum time step was restricted to 1e-4 seconds, as shown in Table 5.9 and Figure 5.27.

The computational domain is exactly the same of Figure 5.8, as well as the grid and boundary conditions. Concerning the elemental composition of pyrolysis gases, the one

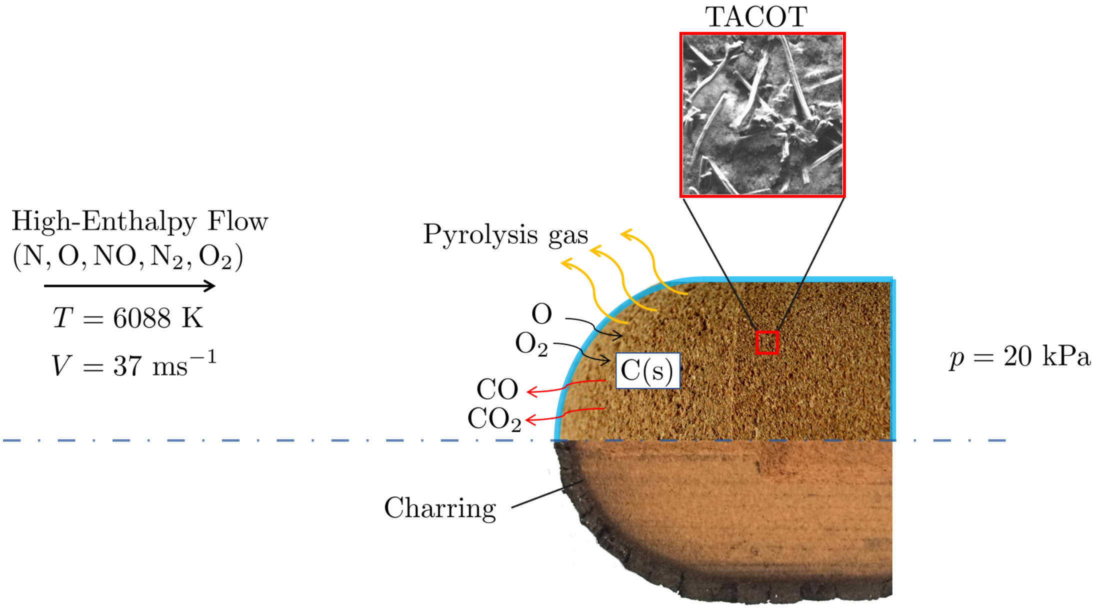

Figure 5.26: Scheme of the simulation of TACOT in Plasmatron conditions.

Table 5.9: Charring ablator: tabulated time step.

Δt [s]	1e-8	1e-7	5e-7	1e-6	1e-5	2.5e-5	5e-5	1e-4
Final time for Δt [s]	1e-7	1e-6	5e-5	5e-4	5e-3	0.01	0.25	1

estimated in Section 3.2.1 for Cork P50 has been chosen for the current analysis and it is shown in Table 5.10. Starting from that elemental composition, the species mass fractions are computed at the local equilibrium conditions by MUTATION++, used as a routine within ARGO. However, the equilibrium computation requires the establishment in advance of the list of chemical species which should be considered. For these reasons, a preparatory analysis was conducted using NASA Chemical Equilibrium with Applications (CEA), in order to detect the most relevant species in the range of temperature between 300 K and 3000 K, and in the range of pressure between 10 mbar and 500 mbar. These are indeed the thermodynamic conditions achievable in the VKI Plasmatron facility. Hence, starting from the elemental composition specified in Table 5.10, NASA CEA returned a list of 8 chemical species: CH_4, CO, CO_2, H_2, H_2O, O, OH, O_2. The same results were

Table 5.10: Elemental composition of pyrolysis gases, for Cork P50.

	C	H	O
Mass fraction	0.0872	0.1937	0.7192
Mole fraction	0.0297	0.7864	0.1839

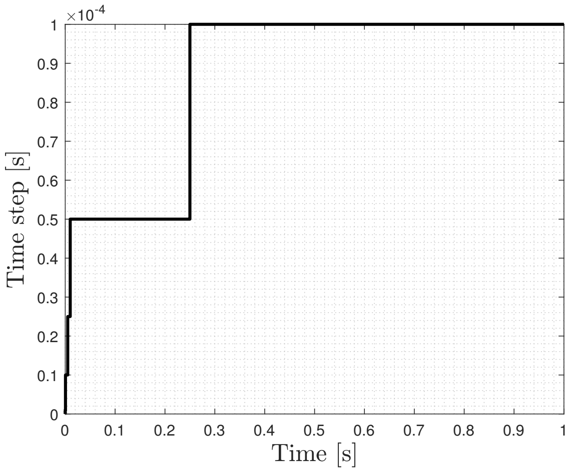

Figure 5.27: Charring ablator: time stepping during the simulation.

also found using MUTATION++, as shown in Appendix. In addition to those chemical species, it is necessary to include also the missing ones which belong to Air5 chemistry model. As a result, 11 chemical species were included in the mixture file of MUTATION++: N, O, NO, N_2, O_2, CH_4, CO, CO_2, H_2, H_2O, OH. Once produced, some of these species are frozen, while CO, CO_2, O and O_2 are able to react with oxygen, according to the homogeneous reactions shown in Table 5.11. In particular, the generation of CO and CO_2 comes from oxidation, pyrolysis and the homogeneous reaction too. In any case, all the chemical species are able to diffuse according to a Schmidt number of $\mathrm{Sc} = 1$. As in the carbon preform simulation, some preliminary tests using the multicomponent diffusion model indeed showed convergence issues, also due to the presence of H_2 that is known to have a quick diffusion because of its low molecular mass.

Table 5.11: Charring ablator: homogeneous reactions included in the reaction mechanisms database of MUTATION++.

Homogeneous reactions	
Dissociation reactions	Exchange reactions
$\mathrm{N_2 + M \rightleftharpoons 2N + M}$	$\mathrm{NO + O \rightleftharpoons N + O_2}$
$\mathrm{O_2 + M \rightleftharpoons 2O + M}$	$\mathrm{N_2 + O \rightleftharpoons NO + N}$
$\mathrm{NO + M \rightleftharpoons N + O + M}$	$\mathrm{CO_2 + O \rightleftharpoons O_2 + CO}$

As regards the oxidation reactions, they are listed in Table 5.12 and it is worth noting again that their backward reaction rates are so small that the reverse reactions do not need to be considered [70]. Moreover, differently from the carbon preform simulation, in TACOT material the carbon fibers are coated by char, therefore they begin to undergo oxidation only once the char has been totally removed. In addition, the charred material is able to react faster than the carbon fibers, therefore a factor 10 was applied to the pre-exponential coefficient A of char. The physical explanation behind this behaviour

Table 5.12: Charring ablator: heterogeneous reactions included in the input file of ARGO in order to describe the oxidation of the carbon fibers.

Oxidation reactions		A	$E_a/\mathcal{R}$	n
$O_2 + 2C(s) \rightarrow 2CO$	$O_2 + 2\text{FibersC} \rightarrow 2CO$	5.73	$9.65e3$	0.5
	$O_2 + 2\text{CharC} \rightarrow 2CO$	57.3	$9.65e3$	0.5
$O + C(s) \rightarrow CO$	$O + \text{FibersC} \rightarrow CO$	3.22	0	0.5
	$O + \text{CharC} \rightarrow CO$	32.2	0	0.5

lies in the structure of the char layer: its cracks and defects make the charred zone more vulnerable to the attack of oxygen, so that the chain of carbon undergoes a faster reaction.

Concerning pyrolysis, two decomposition reactions were taken into account. The coefficients of the Arrhenius type law are listed in Table 5.13 and they were computed by Sakraker [7] for the Cork P50, by means of a TGA analysis.

Table 5.13: Charring ablator: Arrhenius law coefficients for the description of pyrolysis (data from Sakraker [7]).

Pyrolysis reactions	A_0 [s^{-1}]	$E_a/\mathcal{R}$ [K]	n
Reaction R1	4987	9945	1.00
Reaction R2	9999	6187	3.00

The evolution of the species mass fractions along the stagnation line can be observed in Figure 5.28. As in the simulation of the carbon preform, the initial composition was computed by MUTATION++ at equilibrium (Figure 5.28(a)). At $t = 0.005$ s, traces of CO have been detected at the interface (Figure 5.28(b)), just as in the case of the carbon preform simulation. Therefore, one can deduce that these early signs of CO could be associated to oxidation reactions. After $t = 0.5$ s, the production of several species can be observed (Figure 5.28(c)), so this is an indication that pyrolysis has started and a thermal decomposition is affecting the porous material from the inside. The gas production especially involves H_2O, H_2, CO_2 and CO, accompanied by very small trace amounts of CH_4 and OH. At $t = 1.0$ s (Figure 5.28(d)) even the deepest layers of the material show the presence of the pyrolysis gases, also because of convection and diffusion mechanisms. Moreover, the chemical boundary layer is clearly changing too.

Finally, a last observation can be expressed looking at Figure 5.28(c) and 5.28(d). A drop in N_2 can indeed be observed. This effect is actually related to the elemental composition of the mixture, given in Figure 5.29 at $t = 1.0$ s. Near the interface, the mixing of hot air and pyrolysis gases occurs, so that the element N drops for the injection of a gaseous mass which does not contain N. As a consequence, the chemical species are diluted within the mixture and this explains the decrease of N_2 at the interface. The gas blowing changes the total amount of gaseous mass so everything should be rescaled.

The Figure 5.30 shows the mass loss due to both oxidation and pyrolysis. A mass loss of 1.2% was registered after 1 second, corresponding to a loss of 0.28 grams. The

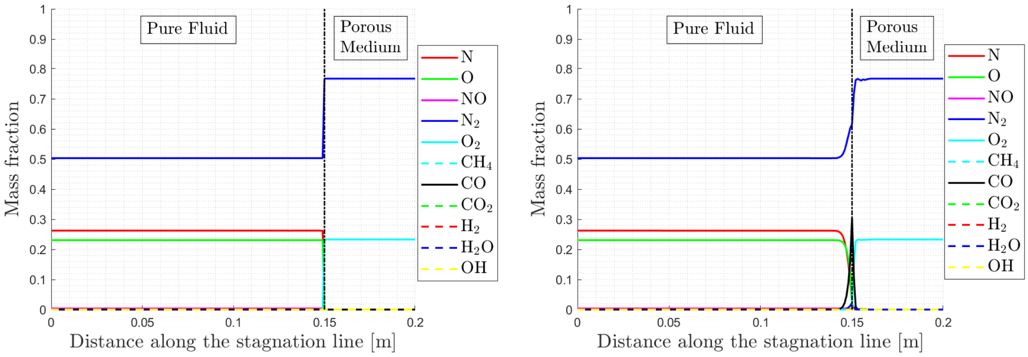

(a) $t = 0$ s (equilibrium) **(b)** $t = 0.005$ s

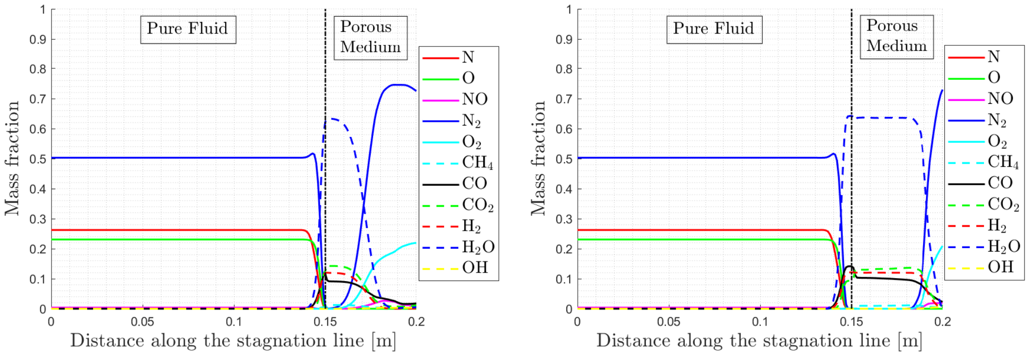

(c) $t = 0.5$ s **(d)** $t = 1.0$ s

Figure 5.28: Charring ablator: evolution of the species mass fractions along the stagnation line.

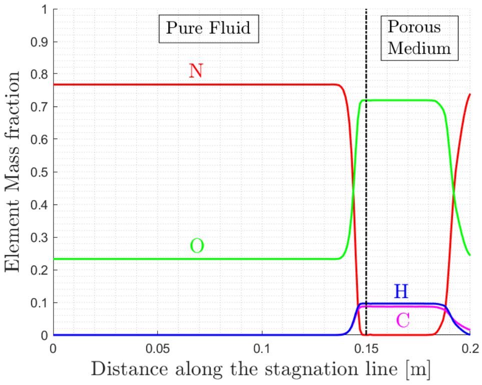

Figure 5.29: Charring ablator: elemental composition along the stagnation line, at $t = 1.0$ s.

mass loss rate of 280 mg/s is thereby certainly much higher than the case of the carbon preform, in which a mass loss rate of only 31 mg/s had been computed. This proves that ablation, in presence of pyrolysis, has stronger effects in terms of material response. The thermal degradation of the phenolic resin can be analyzed in Figure 5.31. The full profile is given by the sum of the density of each solid compound, i.e. carbon fibers (160 kg/m^3), two resins (40 kg/m^3 each) and char (40 kg/m^3). In particular, the decomposition of the resins is highlighted in Figure 5.31(b). After 1 second, the presence close to the interface of a point where the tangent line is horizontal means that the phenolic resin is almost completely decomposed there. The same observation can be clearly derived from Figure 5.32, where the density contour of the two resin compounds is compared with a picture of a P50 sample taken by Sakraker [7]. Naturally, a sufficiently long simulation would provide results closer to the experiments.

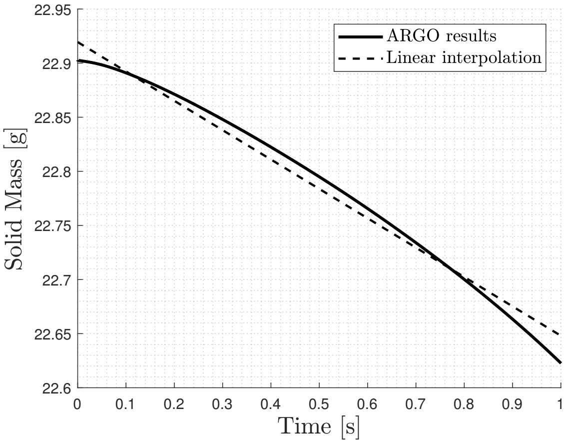

Figure 5.30: Charring ablator: mass loss due to oxidation and pyrolysis.

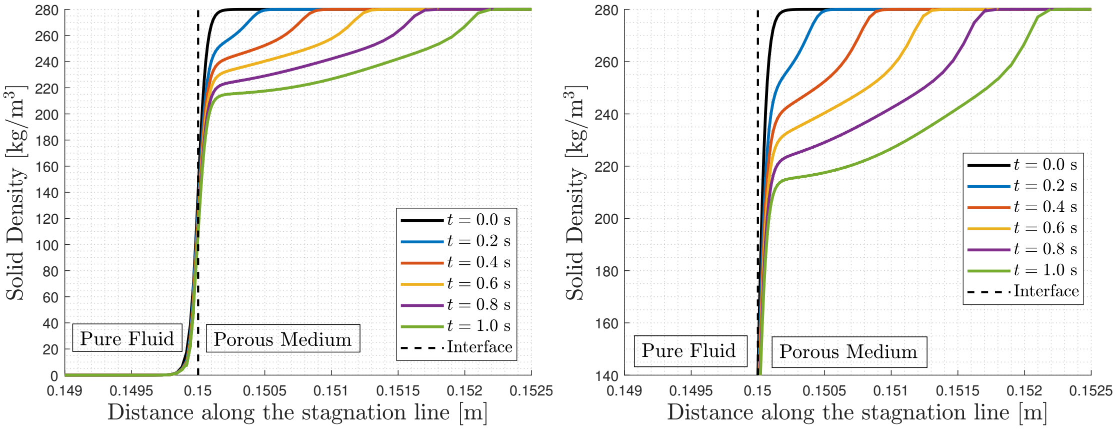

(a) Solid density profile, as sum of the contribuitions of each compound.

(b) Detailed view of the contribuition of the resin.

Figure 5.31: Charring ablator: solid density along the stagnation line.

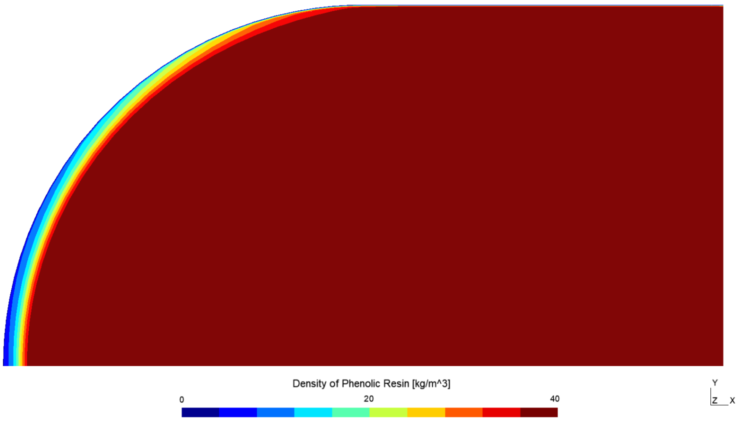

(a) R1 resin compound.

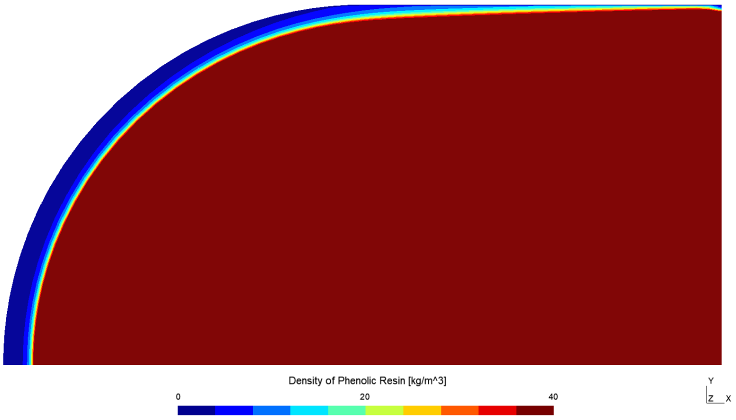

(b) R2 resin compound.

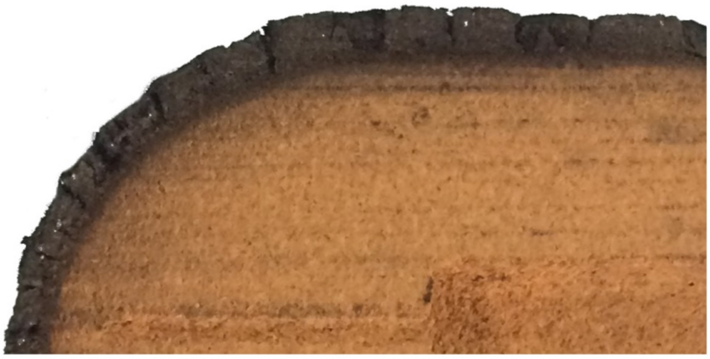

(c) Section of a P50 sample after a test in Plasmatron conducted by Sakraker [7].

Figure 5.32: Charring ablator: decomposition of the two resin compounds, compared with experimental data.

The time evolution of stagnation point temperature is shown in Figure 5.33(a). As in the case of the carbon preform simulation, the initial temperature is approximately equal to 537 K, due to the smoothing applied by ARGO before the start of the simulation, in order to gradually pass from 6088 K of the pure fluid region to 298 K inside the material. The maximum temperature is reached at the end of the simulation, when a value of about 1325 K has been registered. However, the temperature is expected to further increase for longer times. A maximum time of one second is indeed not enough to reach the steady state. This transient shows temperature values significantly lower than those of the carbon preform simulation and the reason is expected to be related to pyrolysis: the blowing gas produced during the material decomposition generates indeed a thermal barrier in front of the sample, reducing the heating effect. Moreover, an interesting but, at the same time, suspicious behaviour can be observed at the first steps: after an initial increase, the temperature profile undergoes a sudden and unexpected fall. As highlighted by Figure 5.33(b), this change in trend takes place in such a short time that it would be not possible to capture the same phenomenon during an experimental test. In fact, the time step is of the order of 10^{-4} seconds, therefore only a numerical simulation is able to detect such fast dynamics. Thus, it might be assumed this initial response could be related to a strong gas blowing due to pyrolysis but, strictly, further investigations are needed. An amount of uncertainty remains indeed concerning the elemental composition of pyrolysis gases, as well as the Schmidt diffusion model, that is less accurate than the multi-component one. Anyway, after that initial transient, the temperature profile evolves in a more classical way.

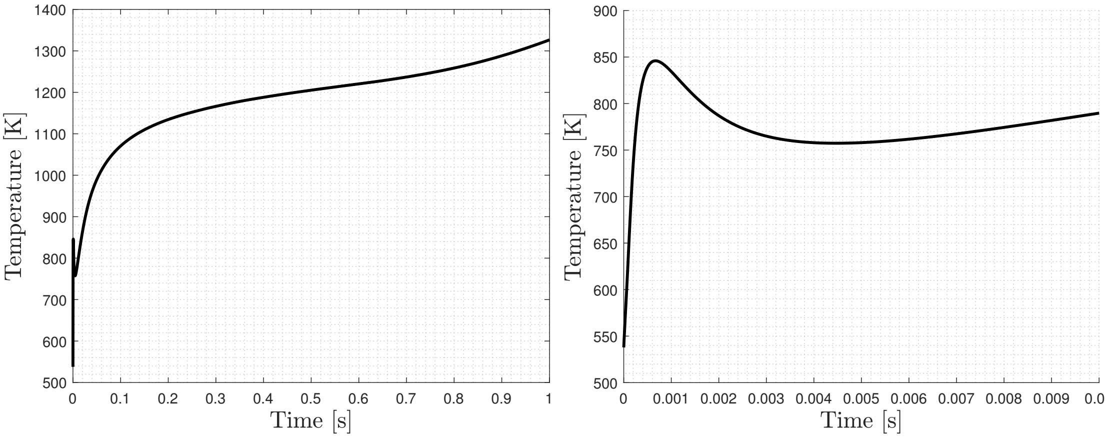

(a) Evolution after one second.

(b) Detailed view on the first steps.

Figure 5.33: Charring ablator: stagnation point temperature.

The Figure 5.35 shows the axial velocity along the stagnation line after one second. The negative velocity close to the gas-surface interface reached an absolute value of 10 m/s, that is considerably high and again attributable to the severe blowing effect, which requires longer periods before disappearing. Finally, the maximum velocity computed at $t = 1.0$ s within the porous medium is approximately equal to 0.4 m/s (Figure 5.36).

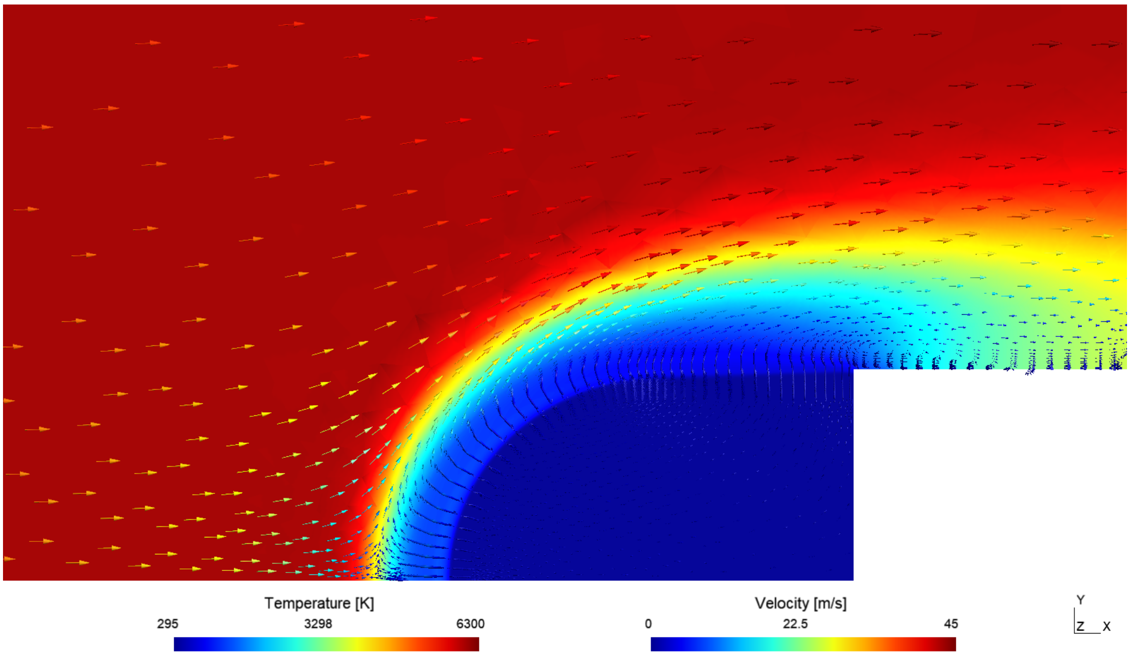

Figure 5.34: Charring ablator: temperature and velocity fields at $t = 1.0$ s.

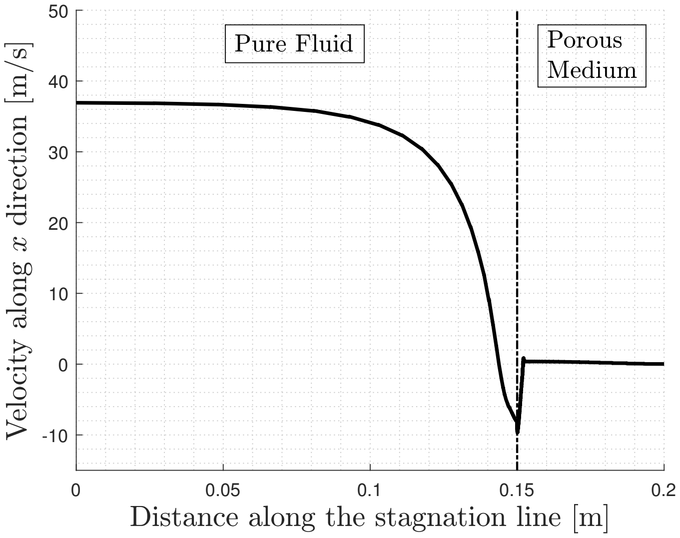

Figure 5.35: Charring ablator: axial velocity along the stagnation line, after $t = 1.0$ s

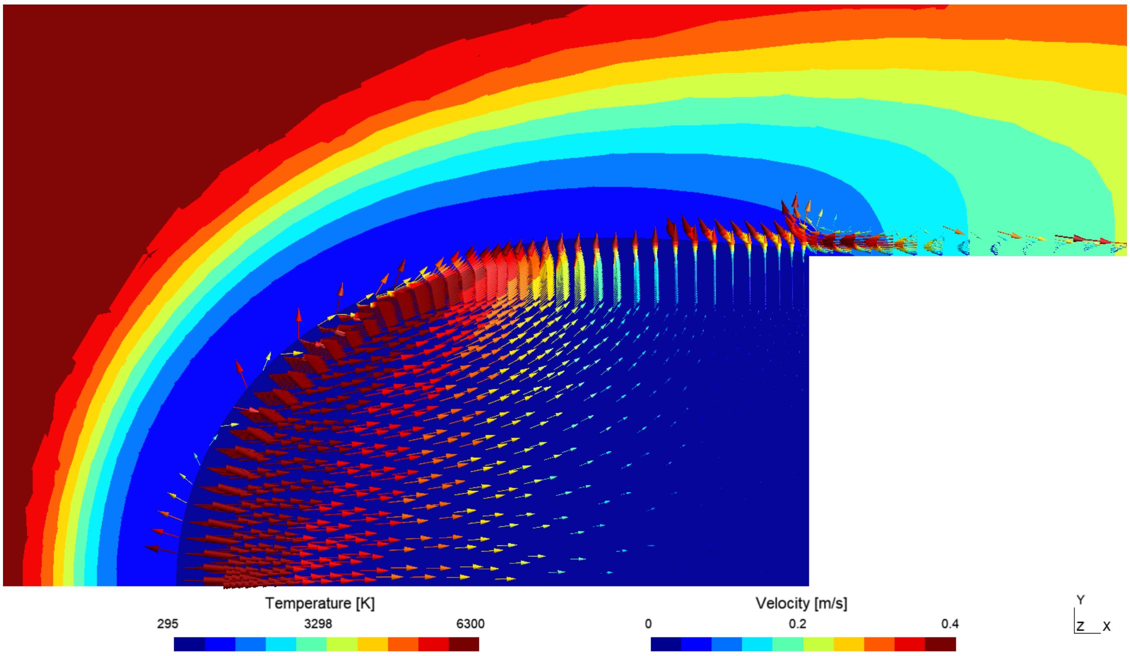

Figure 5.36: Charring ablator: temperature and velocity fields at $t = 1.0$ s, within the porous material.

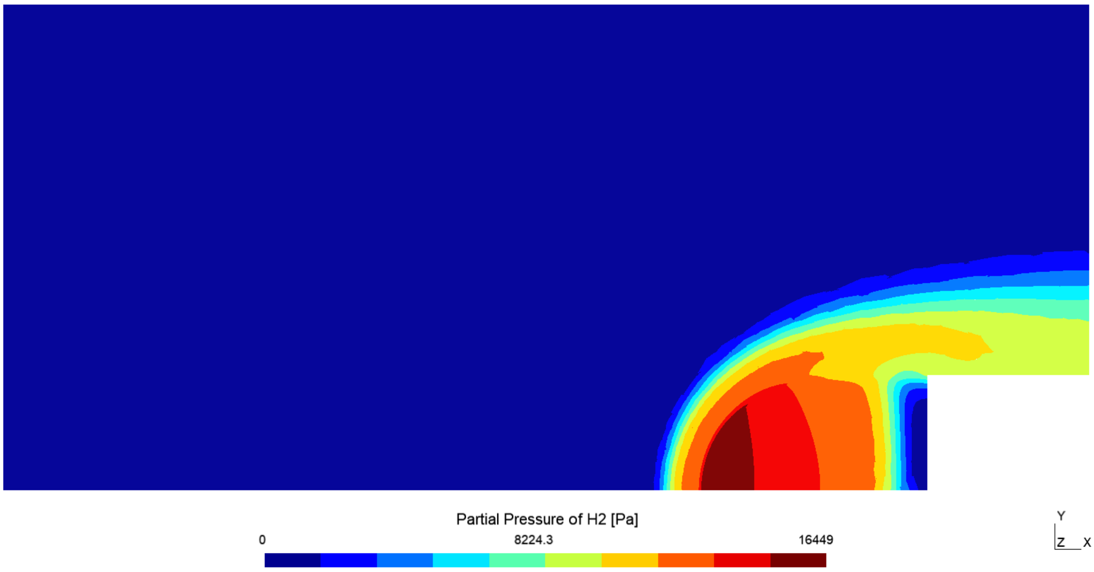

Figure 5.37: Charring ablator: partial pressure field of H_2 after $t = 1.0$ s.

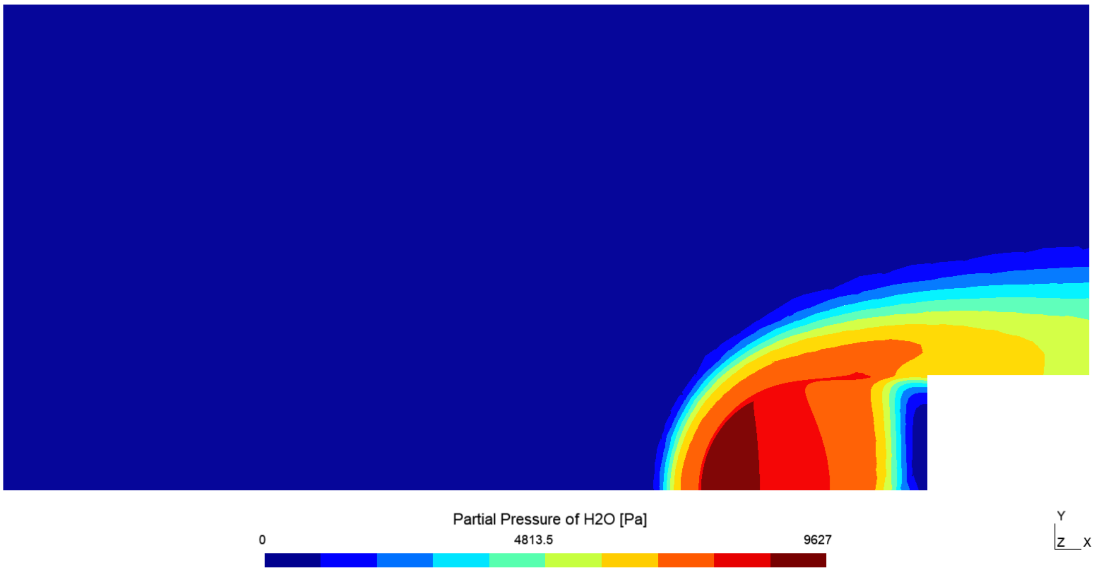

Figure 5.38: Charring ablator: partial pressure field of H_2O after $t = 1.0$ s.

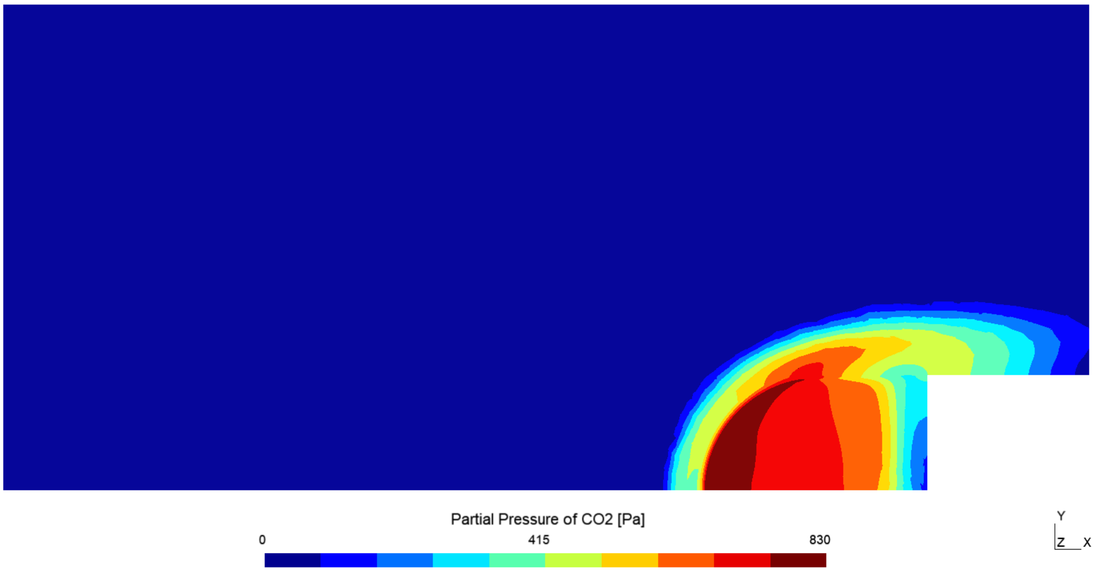

Figure 5.39: Charring ablator: partial pressure field of CO_2 after $t = 1.0$ s.

5.3.1 Trial elemental composition

The simulation of TACOT was repeated using a different elemental composition of pyrolysis gases, in order to better understand to what extent it affects the final results. While the elemental composition used for the previous simulation was computed following a statistical survey and considering that no experimental data were available, a test value has been chosen for this last analysis. It is given in Table 5.14 and a list of 10 chemical species was returned by NASA CEA and MUTATION++: N, O, NO, N_2, O_2, CH_4, CO, CO_2, H_2O, OH.

Table 5.14: Charring ablator: elemental composition of pyrolysis gases (test value).

	C	H	O
Mass fraction	0.2396	0.0362	0.7242
Mole fraction	0.1973	0.3551	0.4476

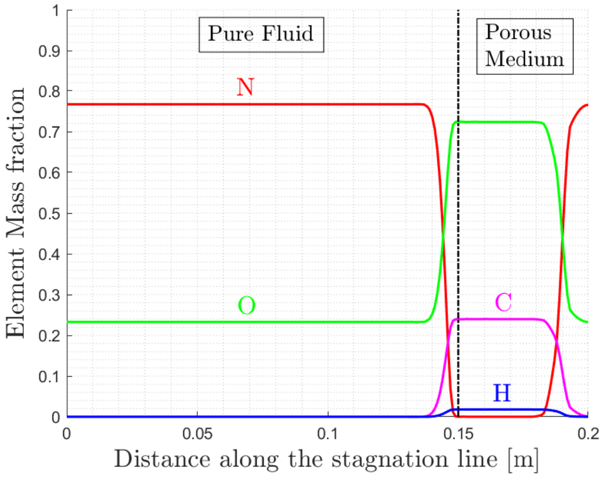

Figure 5.40: Charring ablator: elemental composition along the stagnation line, at $t = 1.0$ s.

The elemental composition along the stagnation line at $t = 1.0$ s is shown in Figure 5.40, while the result in terms of species mass fractions is given in Figure 5.41. Similar considerations are applicable and the most produced chemical species are CO, CO_2 and H_2O. As regards the mass loss due to oxidation and pyrolysis, approximately 0.35 grams were ablated (Figure 5.42), at a mean mass loss rate of 350 mg/s. The decomposition of the resin can be analyzed in Figure 5.43, showing that a plateau has been attained after one second. Therefore, the different elemental composition resulted in a faster thermal degradation, as also illustrated in Figure 5.44, where the thickness of the charred zone is slightly larger than the one of the previous simulation.

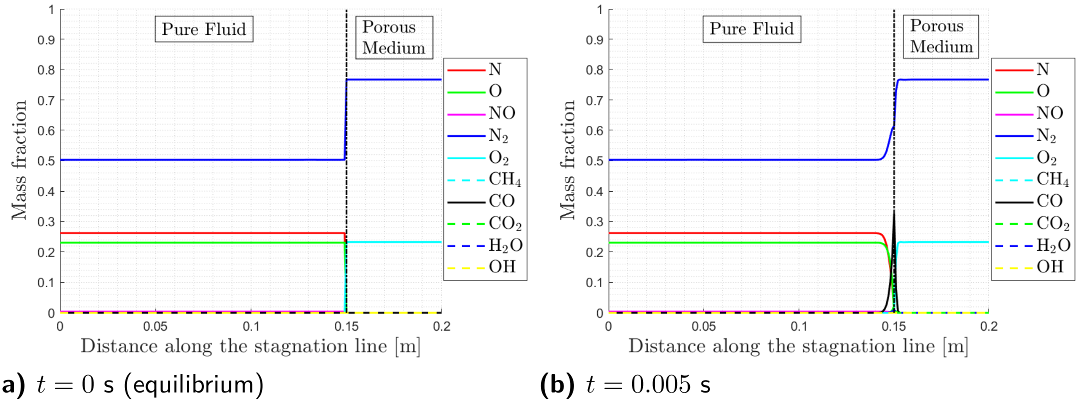

(a) $t = 0$ s (equilibrium)

(b) $t = 0.005$ s

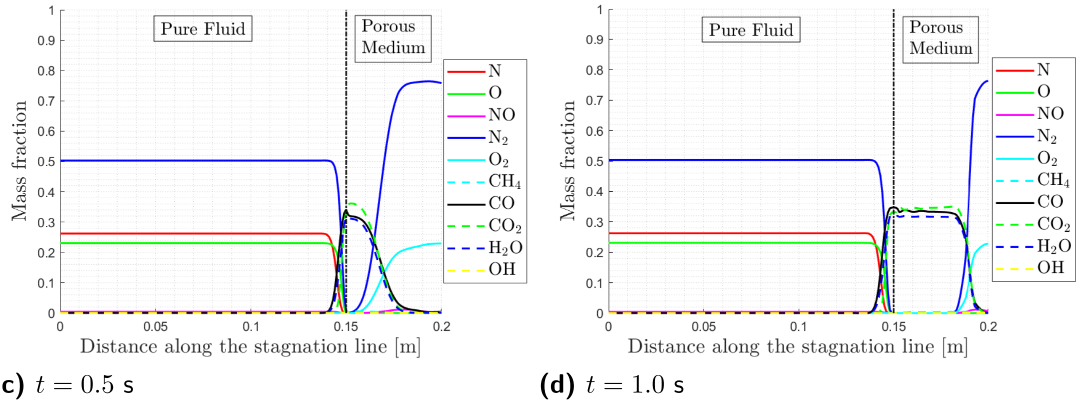

(c) $t = 0.5$ s

(d) $t = 1.0$ s

Figure 5.41: Charring ablator: evolution of the species mass fractions along the stagnation line.

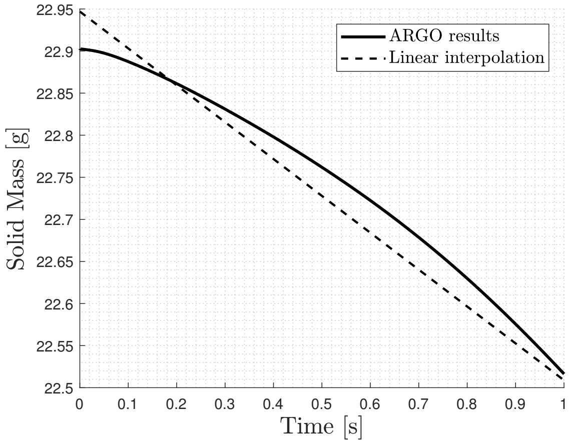

Figure 5.42: Charring ablator: mass loss due to oxidation and pyrolysis.

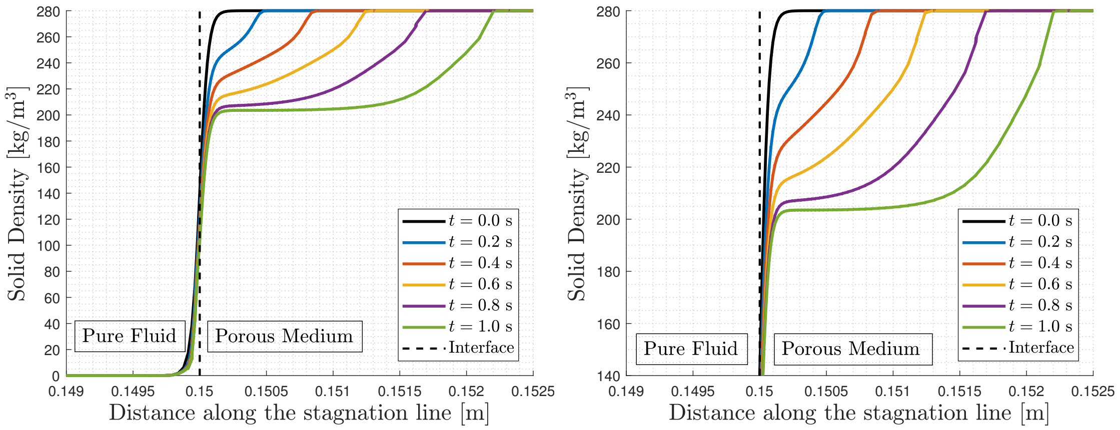

(a) Solid density profile, as sum of the contribuitions of each compound.

(b) Detailed view of the contribuition of the resin.

Figure 5.43: Charring ablator: solid density along the stagnation line.

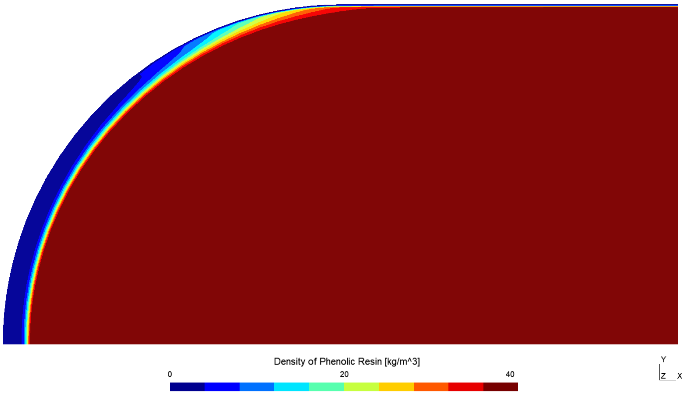

(a) R1 resin compound.

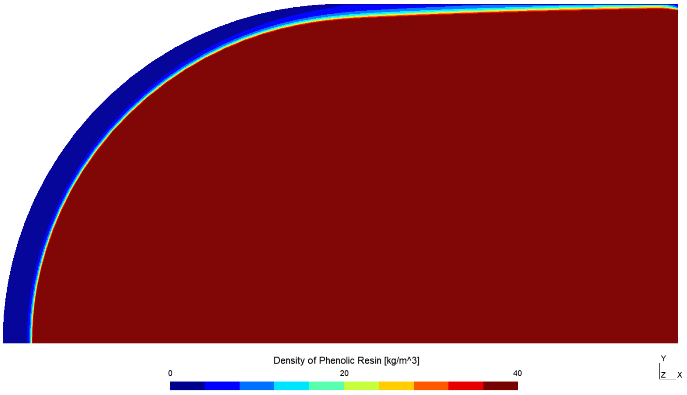

(b) R2 resin compound.

Figure 5.44: Charring ablator: decomposition of the two resin compounds.

Finally, the stagnation point temperature is given in Figure 5.45(a). The curve shows an evolution close to what the previous simulation had highlighted. A similar decrease in temperature can indeed be observed during the initial transient (Figure 5.45(b)), but the maximum temperature attained after one second is quite larger, with a value close to 1480 K. This last result will be commented in the next section, where a final comparison among the three simulations will be made.

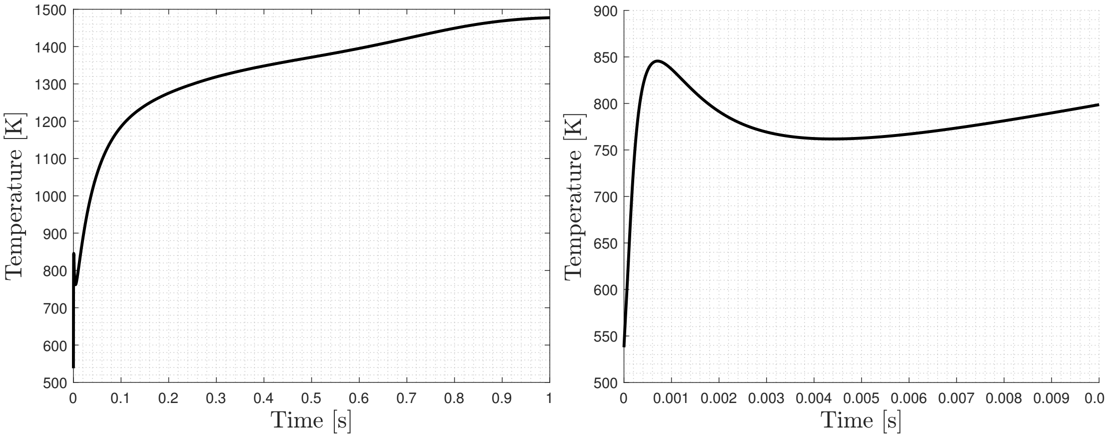

(a) Evolution after one second.

(b) Detailed view on the first steps.

Figure 5.45: Charring ablator: stagnation point temperature.

5.4 A final comparison

In light of the results provided by the simulations of the carbon preform and TACOT, a comparison in terms of stagnation point temperature is given in Figure 5.46. Naturally, it should be clear that, even if the ablation of the carbon perform was simulated for 10 seconds, the corresponding curve of Figure 5.46(a) has been restricted to the first second of time, in order to be compared to the TACOT simulations.

In summary, the carbon preform consists of a porous material made of only carbon fibers, which undergo oxidation reactions but not pyrolysis. At the contrary, the TACOT material is intended to mimic the class of low-density and carbon-phenolic ablators, such as PICA, therefore it is capable of pyrolyzing. In all three cases, the stagnation point was initialized at the same temperature, approximately equal to 537 K and related to the initial smoothing applied by Argo to gradually pass from the external field (at 6088 K) to the porous material (at 298 K). After few steps, a sudden fall can be observed in the temperature profile of TACOT (Figure 5.45(b)), evidencing a strong blowing effect due to the activation of pyrolysis. However, such a behaviour could be very hardly detectable in experimental tests, because of its rapid dynamics, and further investigations should thus be carried out. After this initial transient, temperature shows a more classical evolution and the maximum value is quite different, depending on the material. In particular, the carbon preform attained a temperature greater than 1840 K, while TACOT reached

1325 K and 1480 K, depending on the elemental composition of pyrolysis gases. A first observation is that a charring material like TACOT is indeed expected to show lower temperatures than a non-charring ablator, due to the stronger gas blowing connected to pyrolysis. However, this difference in temperature, of the order of a few hundred degrees, cannot be directly attributable only to pyrolysis, because the materials considered have also different thermal properties, i.e. thermal conductivity and heat capacity, as well as density. So, these aspects certainly result in a different heat transfer. For these reasons, it could be very interesting, as a future investigation, to try to isolate the impact of pyrolysis in order to better quantify its cooling effect. A second consideration is that, in spite of the scale of the plot that shows a misleading plateau condition, temperature is expected to further increase after one second, as highlighted by the carbon preform simulation (Figure 5.18). Hence, longer simulations are needed. Moreover, the gas blowing due to pyrolysis has a time-limited effect (until pyrolysis is completely exhausted), therefore an increase in temperature of TACOT is expected for this reason too. Finally, a last observation should be reserved to the effect of the elemental composition of pyrolysis gases. In fact, the difference of about 150 K evidenced by the TACOT simulations, are exactly attributable to the different elemental composition used as input by MUTATION++ for the computation of the pyrolysis production rate. The same material and the same physical conditions have indeed been tested. So this conclusion proves the importance of carefully assessing the elemental composition of pyrolysis gases, with a view of obtaining plausible results. For this purpose, experimental tests should be performed to get an accurate estimation of the elemental composition.

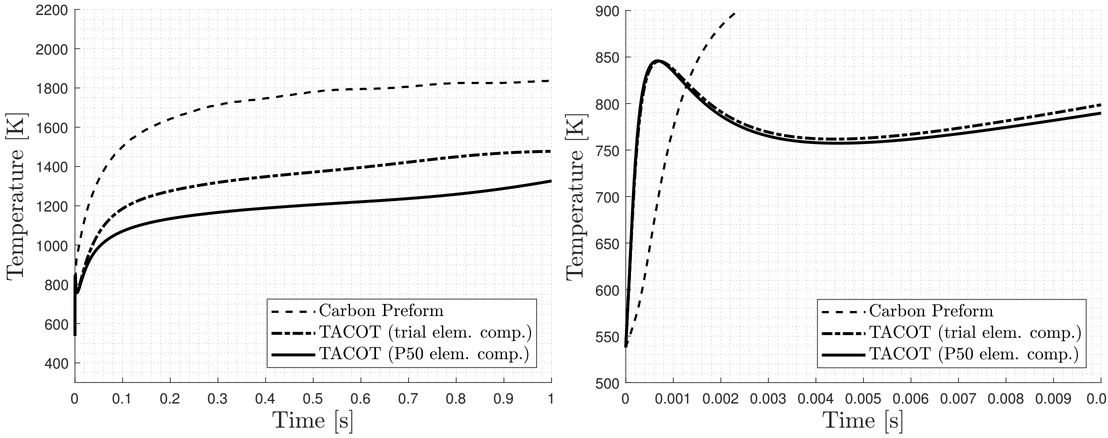

(a) Evolution after one second.

(b) Detailed view on the first steps.

Figure 5.46: Stagnation point temperature compared for different materials and elemental composition of pyrolysis gases.

5.5 Swelling

The development of a MATLAB code based on the FDM allowed to test the physical model presented in Section 3.2.2. A 1D nonlinear convection equation was solved in the variable U, representing what in ARGO is the average solid density (normalized):

$$\frac{\partial U}{\partial t} + U\frac{\partial v_s}{\partial y} + v_s\frac{\partial U}{\partial y} = 0 \tag{5.5}$$

As already mentioned, an a priori assumption on the velocity distribution was proposed, therefore the main point of the model is the choice of an appropriate definition for the velocity profile. A one-dimensional domain was first considered. It extends along the y-direction, up to twice the initial length of the sample L_i. The computational grid consists of 201 nodes and a time step equal to 5e-4 seconds has been set, in order to satisfy the CFL condition. An Euler explicit scheme is indeed used for the time discretization. The

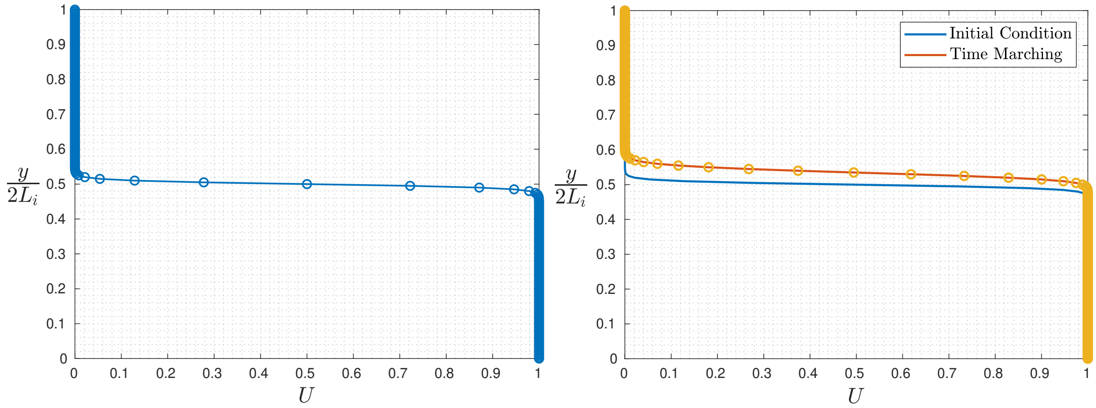

(a) Initial condition.
(b) Solution after 60 seconds.

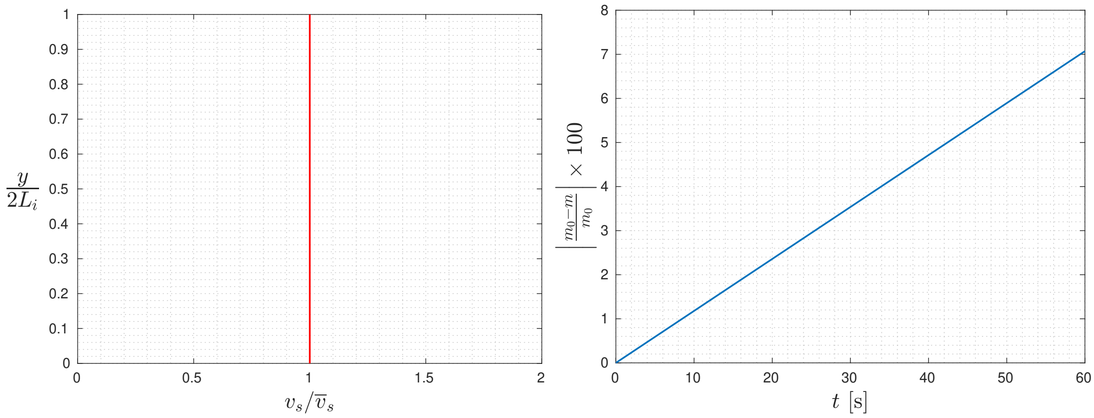

(c) Imposed velocity distribution.
(d) Checking mass conservation.

Figure 5.47: Swelling: simulation using an average velocity profile.

first trial assumption was to impose an average velocity, given by:

$$v_s = \frac{L_f - L_i}{\Delta t} = 0.0563 \text{ m/s} \tag{5.6}$$

where L_f is the final length of the sample, whilst $\Delta t = 24$ s is the swelling period, measured by Sakraker [7] during the test in the VKI Plasmatron facility. A total time of 60 seconds was simulated and the solution is shown in Figure 5.47(b). As explained in Section 3.2.2, a constant velocity profile does not ensure the mass conservation, since the area under the curve changes with time. Two different functions have been implemented to compute, for each time step, an approximation of the integral of U and evaluate the mass conservation by means of the trapezoidal rule or the Simpson's rule.

A way to ensure the mass conservation without involving the theory of elasticity is to impose a velocity gradient. Therefore, after investigating the physical meaning and the role that is expected of v_s, a sigmoid function has been used to define the velocity profile (Figure 5.48(c)). This approach allowed to conserve the solid mass, as shown in Figure 5.48(d) and to simulate, as shown in Figure 5.48(b), the behaviour that was expected: during swelling, the average solid density has indeed to increase on the side of the gas and to decrease on the side of the porous material.

So the next step was to include other physical effects, such as the one of the thermal gradients. Hence, the 1D heat equation was solved for the virgin material:

$$\frac{\partial T_v}{\partial t} = \frac{k_v}{\rho_v c_v} \frac{\partial^2 T_v}{\partial y_v^2} \tag{5.7}$$

The boundary conditions are given by:

$$\begin{cases} y = 0 & \longrightarrow \quad k_v \dfrac{\partial T_v}{\partial y_v} = 0 \\ y = L_i & \longrightarrow \quad k_v \dfrac{\partial T_v}{\partial y_v} = \dot{q}_{\text{ext}} - \varepsilon_v \sigma T_w^2 \end{cases} \tag{5.8}$$

where $\dot{q}_{\text{ext}}$ is the wall heat flux, generated by a plasma torch within the Plasmatron facility and measured during the test of Sakraker [7]. Actually, the wall heat flux is not measured directly, but a non-ablative cold-wall heat flux probe is used to measure a reference cold-wall heat flux, $\dot{q}_{\text{ref}} = \dot{q}_{\text{cw}}$ and a cooling system allows to keep the wall temperature of the probe to a constant value, $T_{cw} = 350$ K. Therefore, the heat flux measured by the copper probe is expected to be greater than the actual hot-wall heat flux:

$$\dot{q}_{\text{cw}} > \dot{q}_{\text{hw}} \tag{5.9}$$

The value of $\dot{q}_{\text{hw}}$ was thus computed using the definition of the *Stanton number*:

$$C_H = \frac{\dot{q}_{hw}}{\rho_e V_e (h_{aw} - h_w)} \tag{5.10}$$

where h_w is the wall enthalpy, while h_{aw} is the adiabatic wall enthalpy. An exact solution for h_{aw} can be determined only solving the boundary layer equations, with the boundary

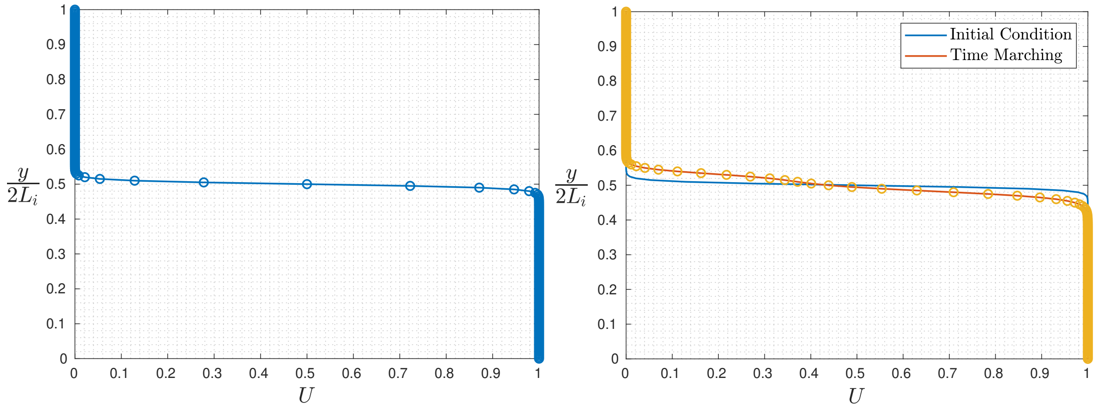

(a) Initial condition.

(b) Solution after 60 seconds.

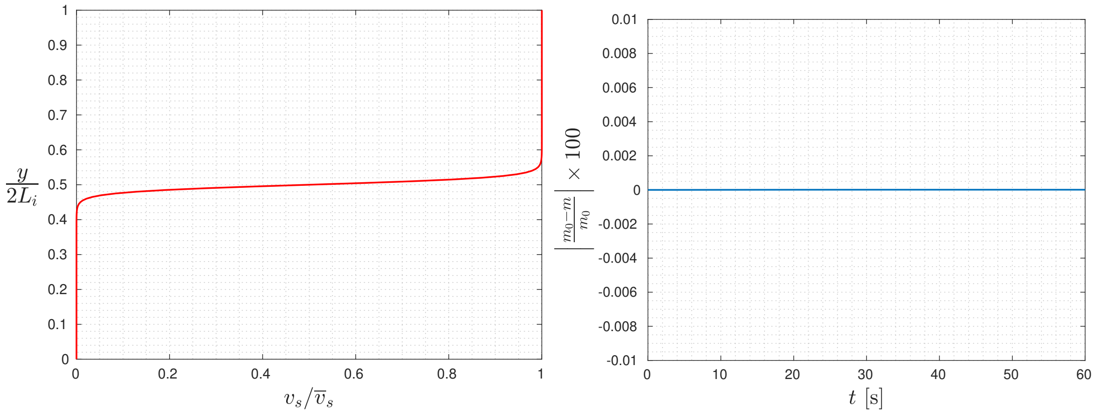

(c) Imposed velocity distribution.

(d) Checking mass conservation.

Figure 5.48: Swelling: simulation using a sigmoid function to describe the velocity distribution.

condition $(\partial T/\partial y)_w = 0$. However, another simplified method is to use the *recovery factor*, r:

$$\begin{cases} h_{aw} = h_e + r\dfrac{V_e^2}{2} \\ h_e^0 = h_e + \dfrac{V_e^2}{2} \end{cases} \implies \quad h_{aw} = h_e + r(h_e^0 - h_e), \quad r = \frac{h_{aw} - h_e}{h_e^0 - h_e} \tag{5.11}$$

For incompressible flows the recovery factor r is equal to $\sqrt{Pr}$. Assuming that the heat conduction is equal to the viscous dissipation in the boundary layer [7], thus:

$$Pr \approx 1 \quad \implies \quad r \approx \sqrt{Pr} \approx 1 \quad \implies \quad h_{aw} \approx h_e^0 \tag{5.12}$$

Since C_H is a similarity parameter for such flows, it is possible to impose the equilibrium:

$$\frac{\dot{q}_{cw}}{h_e^0 - h_{cw}} = \frac{\dot{q}_{hw}}{h_e^0 - h_{hw}} \tag{5.13}$$

where:

$$h_e^0 = h_e + \frac{u_e^2}{2} \tag{5.14}$$

Since the velocity in Plasmatron is very low, then:

$$\frac{u_e^2}{2} \to 0 \quad \Longrightarrow \quad h_e^0 \approx h_e \tag{5.15}$$

Therefore:

$$\frac{\dot{q}_{cw}}{h_e - h_{cw}} = \frac{\dot{q}_{hw}}{h_e - h_{hw}} \tag{5.16}$$

where h_e is the enthalpy at the edge of the boundary layer, provided by the VKI rebuilding code CERBOULA [7]. This allows the *enthalpy rebuilding*, solving the boundary layer equations in order to obtain $h_e = 7.2$ MJ/kg. The last unknowns, h_{cw} and h_{hw}, have been computed using MUTATION++, that computed the equilibrium mixture enthalpies at the pressure p and temperature T_{cw} and T_{hw} respectively (Table 5.15, 5.16) provided by Sakraker [7]. Hence, the hot-wall heat flux is equal to:

$$\dot{q}_{hw} = \dot{q}_{cw} \frac{h_e - h_{hw}}{h_e - h_{cw}} = 251.77 \text{ kJ/kg} \tag{5.17}$$

This value was chosen for the resolution of heat equation, computing the time evolution of temperature after $t = 132$ s, that is the duration of the test in Plasmatron performed by Sakraker [7]. Furthermore, since the computation of the wall temperature involves a nonlinear equation, the Newton-Raphson method has been implemented and a wall temperature equal to $T_{hw} = 1560.51$ K was computed, as shown in Figure 5.49(b). As explained in Section 3.2.2, these results have been used in order to define a velocity $\hat{v}(t)$ connected to the effect of thermal gradients. It is reiterated that $\hat{v}$ is actually a strain-rate and it is given by:

Table 5.15: h_{cw} provided by MUTATION++

p $[Pa]$	T_{cw} $[K]$	h_{cw} [kJ/kg]
4100	350	52.48

Table 5.16: h_{hw} provided by MUTATION++

p $[Pa]$	T_{hw} $[K]$	h_{hw} [kJ/kg]
4100	1644.94	$1.52 \cdot 10^3$

$$\hat{v}_s(t) = \frac{\partial s}{\partial t} = \alpha \int_0^L \frac{\partial T}{\partial t} \, \mathrm{d}y \tag{5.18}$$

Its evolution is given in Figure 5.50 and it allowed to describe the swelling velocity v_s as a function of both space and time:

$$v_s(y, t) = \hat{v}(t) S(y) \tag{5.19}$$

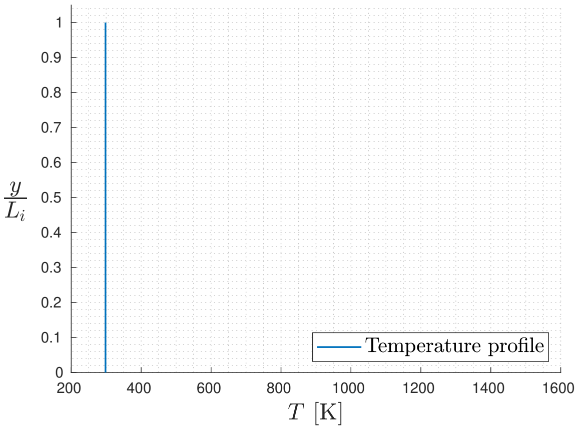

(a) Initial condition, at 298 K.

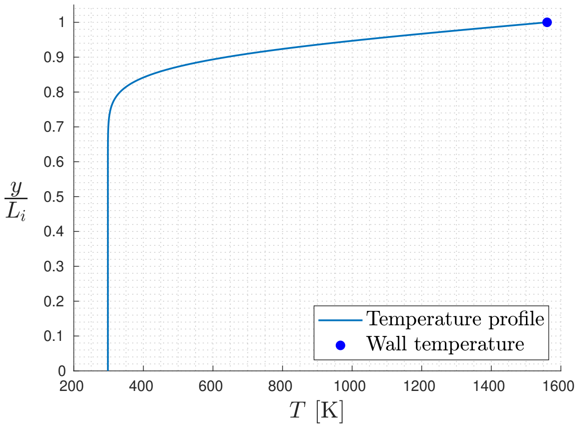

(b) Solution after 132 seconds.

Figure 5.49: Solution of the 1D heat equation in Plasmatron conditions.

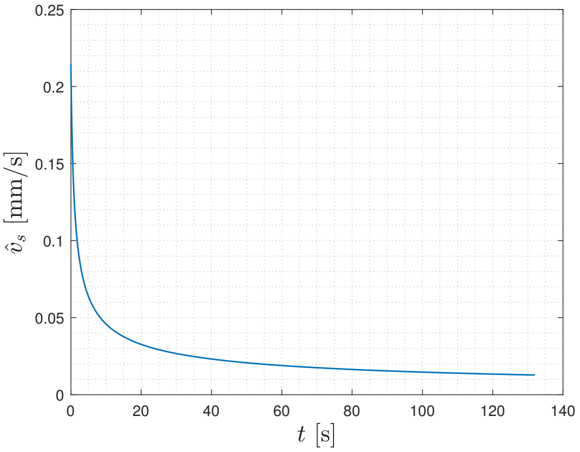

Figure 5.50: Evolution in time of the strain-rate, governed by thermal gradients.

Using this new definition, the simulation was repeated and the solution is shown in Figure 5.51(b). The swelling velocity v_s thus decreases with time, governed by the evolution of temperature gradients, until it collapses on the straight line $v_s(y,t)=0$ (Figure 5.51(c)). This approach allowed not only to guarantee the conservation of the solid mass (Figure 5.51(d)), but also to account for a relation between the swelling mechanism and the temperature field, so that the thermal expansion is free to automatically stop if the temperature gradients decrease under a certain value.

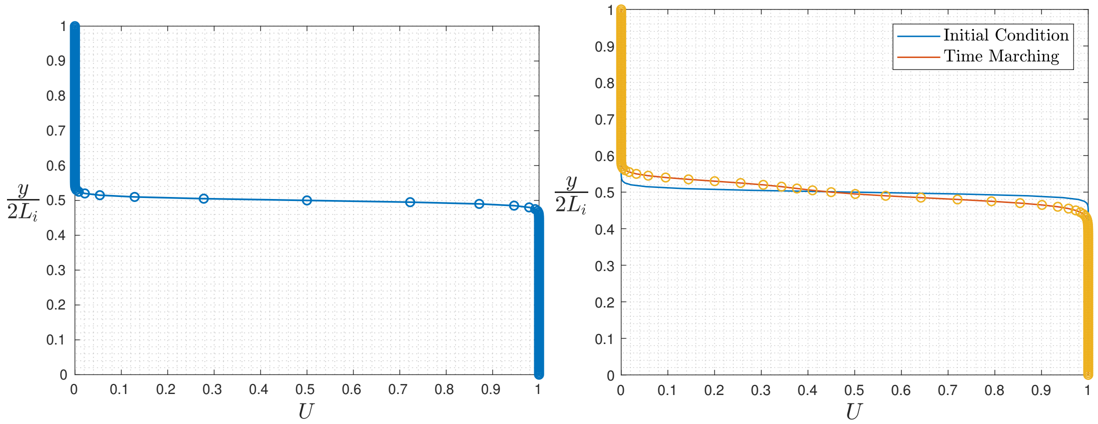

(a) Initial condition. **(b)** Solution.

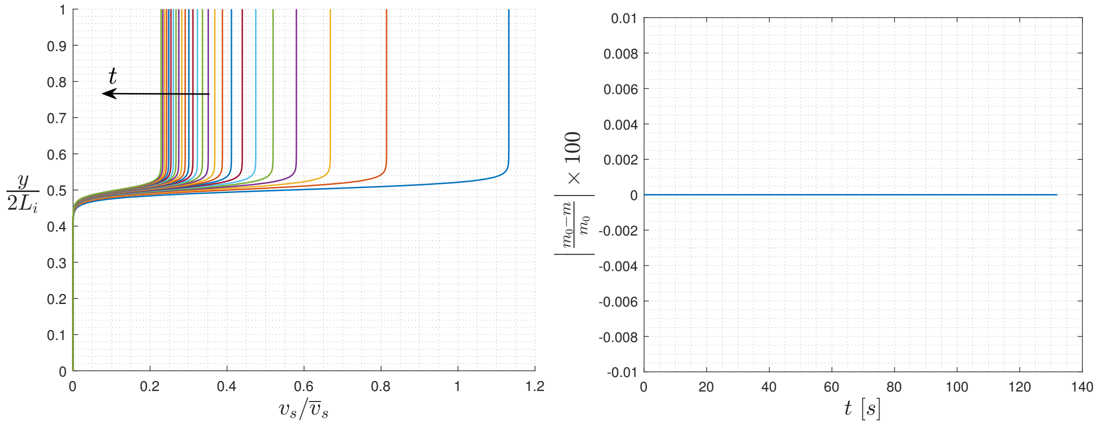

(c) Imposed velocity distribution. **(d)** Checking mass conservation.

Figure 5.51: Swelling: simulation including the effect of thermal gradients.

The effect of the decomposition state of the material has been included too: during the resolution of the 1D heat equation, both pyrolysis and char fronts are tracked by means of two characteristic temperatures, provided by Sakraker [7]. In particular, the pyrolysis front is identified by a temperature of 430 K ($\xi=0$), while the char front by 780 K ($\xi=1$), as shown in Figure 5.52. The two fronts travel along the material at different velocities, so the thickness of the pyrolysis layer is expected to increase, as can be deducted from Figure 5.53(a). These effects, presented in detail in Section 3.2.2 and

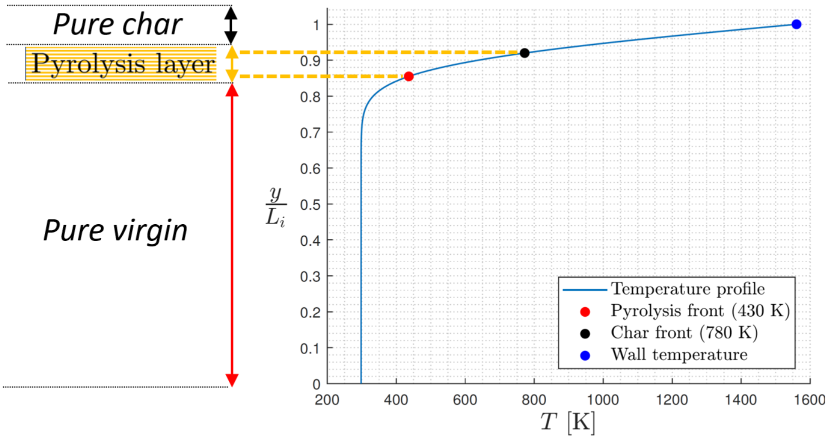

Figure 5.52: Solution of the 1D heat equation in Plasmatron conditions. Pyrolysis and char fronts are tracked by means of two characteristic values.

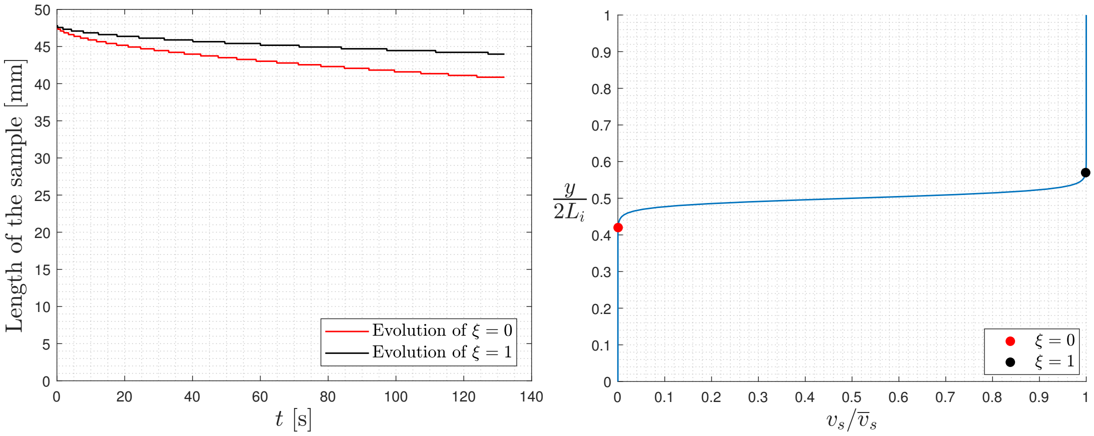

(a) Traveling at different velocities, pyrolysis and char fronts increase their distance, which results in greater thickness of pyrolysis layer.

(b) Pyrolysis and char fronts localized on the velocity profile.

Figure 5.53: Modeling of the decomposition state of the material.

included in the expression of the swelling velocity, can be better understood looking at the sketch of Figure 5.54, in which they have been isolated: the velocity profile is shifted down in each time step to simulate the pyrolysis front consuming the virgin layer. At the same time, the slope of the velocity profile is increased in each step to simulate the increase in thickness of the pyrolysis layer. Both pyrolysis and char fronts (respectively identified by $\xi = 0$ and $\xi = 1$) indeed travel deep within the material increasing their distance due to their different velocities. In particular, the pyrolysis front is faster than the char front. Finally, the various effects were thus combined together, getting the results given in Figure 5.55.

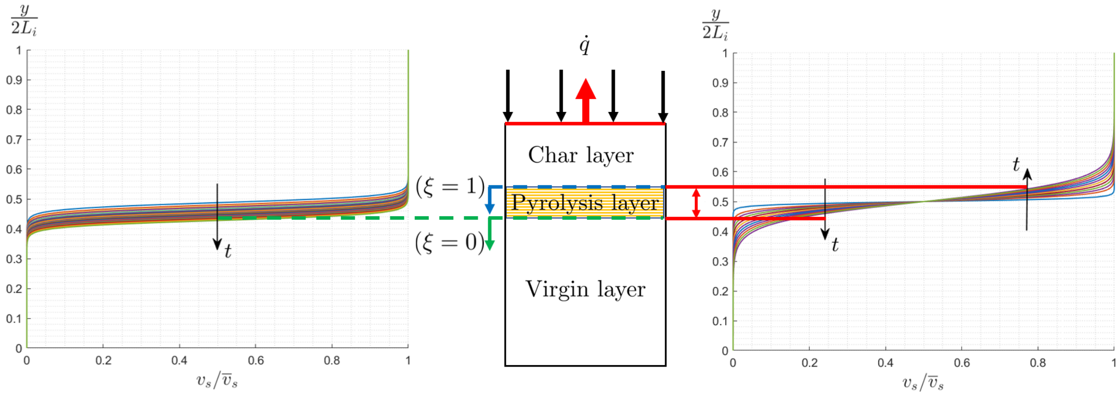

Figure 5.54: Scheme of the further physical mechanisms which have been modeled in order to increase the level of compatibility with Argo.

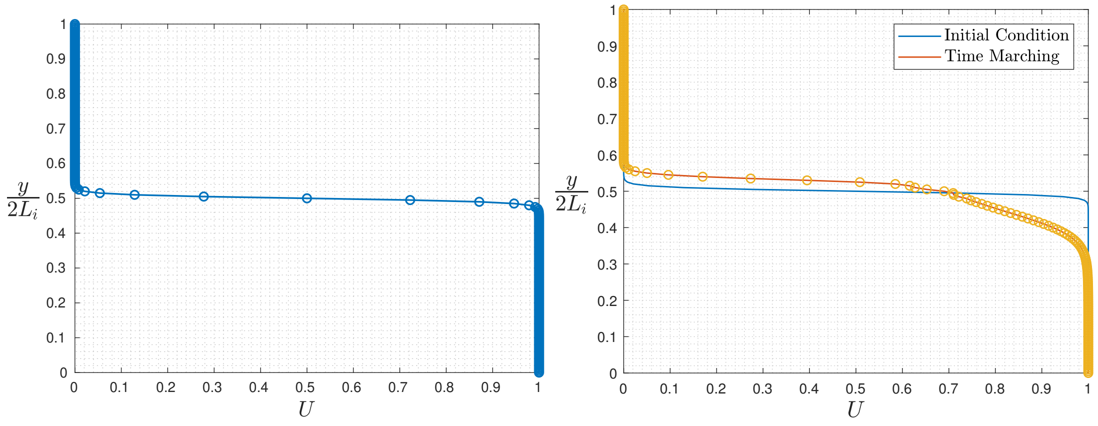

(a) Initial condition.

(b) Solution.

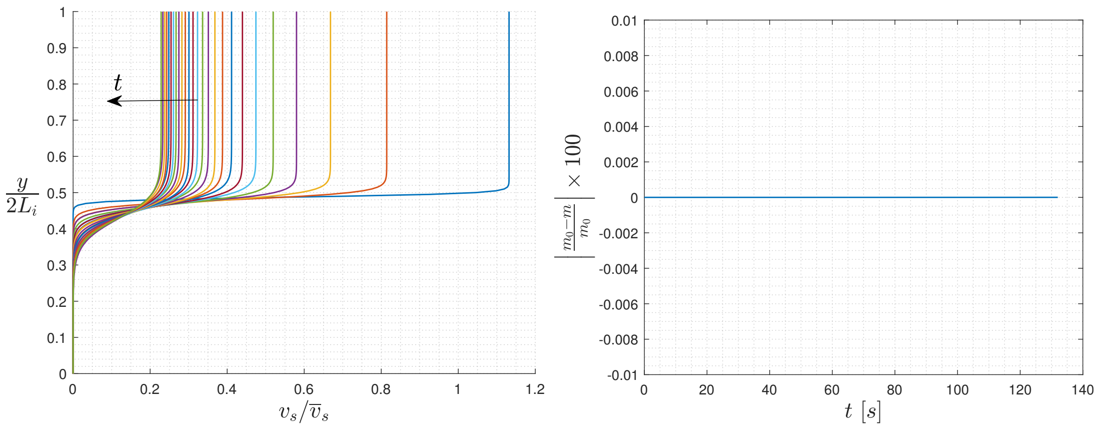

(c) Imposed velocity distribution.

(d) Checking mass conservation.

Figure 5.55: Swelling: simulation combining the various effects.

Extension to a 2D domain

The same model was extended to a two dimensional domain, although a zero velocity was imposed along the x-direction. In fact, the experimental tests of Sakraker [7] provided information about the thermal expansion of the sample only along one direction. Hence, at the moment this extension is intended to be used for a better visualization purpose and to test the capabilities of the MATLAB code.

The computational grid is shown in Figure 5.56. It consists of a square domain discretized in 201 nodes in each direction.

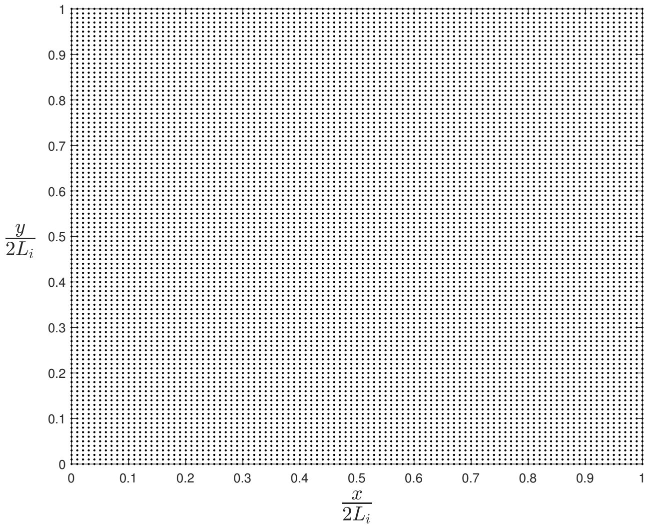

Figure 5.56: Computational grid (2D).

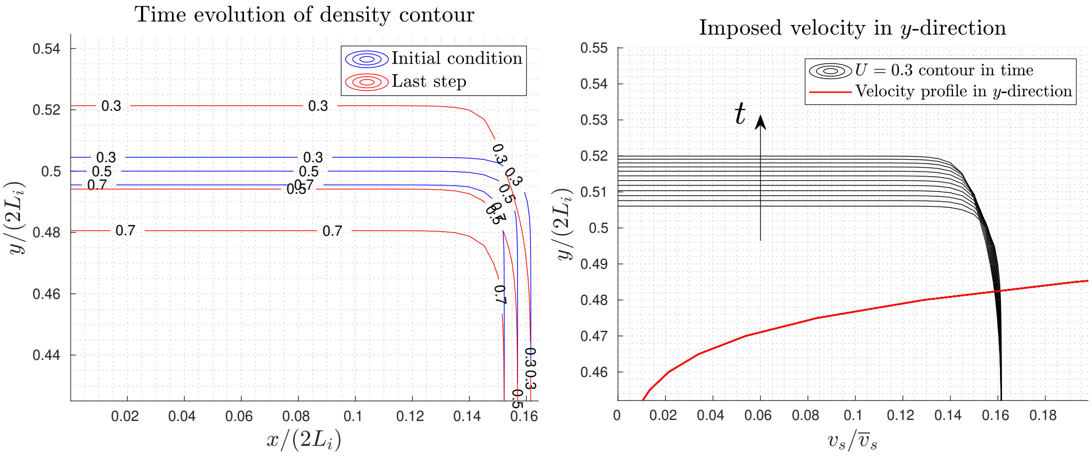

(a) Initial condition.

(b) Solution after 60 seconds.

Figure 5.57: Swelling: evolution of the U contour with time.

The results of the final simulation are given in Figure 5.58. Instead, the Figure 5.57(a) shows the evolution of some characteristic values of the U contour near the interface; in particular, the contour $U = 0.3$ evolves along the y-direction towards the external gas (Figure 5.57(b)), while the contours $U = 0.5$ and $U = 0.7$ shift down along the material, proving that the solid mass has been spread on a bigger volume, as one would expect from an expansion mechanism. For these reasons, the developed model showed the capability to predict the swelling behaviour and provide an answer to the question concerning how to model this physical phenomenon.

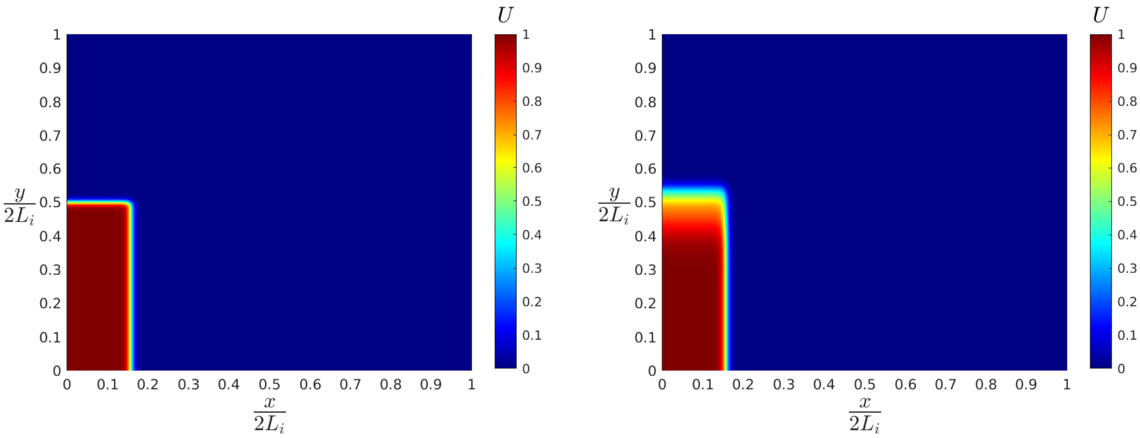

(a) Initial condition.

(b) Solution.

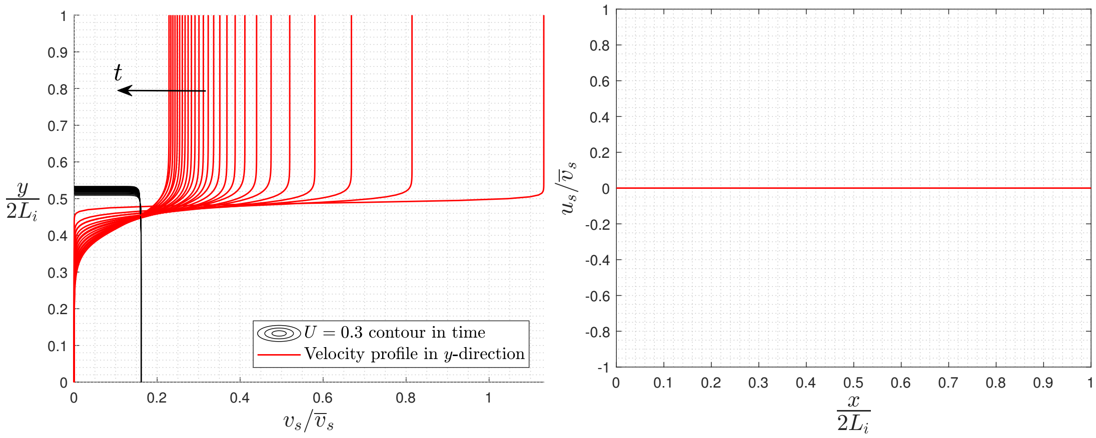

(c) Velocity distribution imposed along the y-direction.

(d) Zero velocity along the x-direction.

Figure 5.58: Swelling: simulation on a 2D domain.

Conclusions

This master thesis focused on numerical modeling of a new class of cork-based ablative materials with thermal protection purposes. Their excellent mechanical and thermal properties make them appealing in the framework of atmospheric re-entry. At the same time, the atypical response of such materials requires further modeling efforts and, for this reason, it is currently object of study by ablation community. The present work was carried out at the von Karman Institute for Fluid Dynamics and embedded in the research activities led by one of the study teams, in collaboration with Cenaero, that provided the numerical code ARGO to simulate ablative materials. Recently, cork received attention for the use of cork-phenolic P50 in the heat shield of the QARMAN Re-entry CubeSat, lifted-off to the ISS on December 2019. During previous experimental campaigns, P50 had exhibited a thermal response mainly characterized by a pyrolyzing and swelling behaviour, emphasizing that the numerical prediction of such TPMs is subject to the capability of correctly modeling these physical phenomena.

Most of modern ablation simulation tools are indeed not capable of predicting this specific behaviour, therefore the motivation behind this thesis was to explore and test some methodologies to treat both pyrolysis and thermal expansion of cork-phenolic ablators. Hence, the present work was carried out following two parallel paths, with a good degree of affinity but not ready to cross yet. In fact, the ideal goal kept in mind throughout the development of this project was to assume, for the future, its natural prosecution, for the purpose of converging the two objectives and, as a result, in order to offer an attractive numerical tool able to simulate pyrolysis and swelling of cork-based TPMs.

In a first part of this work, a literature review about the thermochemical behaviour of cork-phenolic materials was proposed. To date, modeling of pyrolysis and swelling actually have different levels of development; in fact, pyrolysis received a greater attention in the last decades, thanks to the visibility provided by NASA to PICA materials. These do not contain cork but are still able to pyrolyse because they are impregnated with a phenolic resin. At the contrary, the problem of modeling the swelling behaviour has mostly been treated in studies of wood and other intumescent systems, such as paints, propellants and fire-retardants, but nonetheless it is still at a premature stage. For these reasons, the treatment of swelling required a greater effort and it represents the main contribution of this thesis. A short exploration of the state of the art was conducted, supported by experimental evidences, with the aim to identify the key points within the physics of the problem. Physical insight can indeed make easier the devising of mathematical models. Then, the typical modeling assumptions and available solutions were briefly examined. After an overview about the specific behaviour of cork-based materials, the next step was to embark on a presentation of the physical models. This was the point where the study of pyrolysis and swelling took separate ways. In fact, while the former had already been included within ARGO, the latter needed the development of a specific model.

Concerning pyrolysis, actually only the specific behaviour of carbon-phenolic ablators had previously been modeled within ARGO, so a further modeling effort was required in order to extend the code to the treatment of cork-phenolic ablators, which indeed undergo the thermal decomposition of both cork and resin. However, the development of such a complex model was beyond the scope of this work. Hence, it focused on the improvement of the way in which the thermal decomposition was taken into account within ARGO, providing an accurate method to compute the pyrolysis production rate. A function calling the VKI MUTATION++ library was coded within the *DGAblation* module, in order to compute the composition of pyrolysis gases at thermochemical equilibrium, rather than pre-fixing it from the start of the simulation, as was done before. The equilibrium computation shifted the problem towards the evaluation of the elemental composition of pyrolysis gases. As a preliminary analysis, a statistical approach was chosen for its estimation, based on literature data about cork. Two test cases were performed by means of ARGO, using the adiabatic 0D reactor solver, in order to test the new implementation. Data of TACOT and a carbon-phenolic ablator from the VKI database were used. The simulations were performed for both a pre-fixed composition and equilibrium one and the comparison showed, as expected, that the new implementation allowed to compute the composition of pyrolysis gases according to the local temperature and pressure. Moreover, the pre-fixed composition led to an underestimation of temperature due to pyrolysis. Then, a simulation of a non-charring carbon-preform ablator in Plasmatron conditions was performed, using the Navier-Stokes solver included within ARGO. The aim was to analyze only the material recession due to oxidation reactions. A total time of 10 seconds was simulated in order to reach the quasi-steady state, getting results in agreement with those of Schrooyen et al. [43]. The material recession was correctly captured, as well as the production of CO due to oxidation of carbon fibers, observing a surface ablation regime. Finally, since a continuum approach is adopted in ARGO, the temperature evolution at the stagnation point showed sensible variations depending on the definition of the interface. This would thus require experimental tests in order to be better localized. For the future, it could be also interesting to repeat the analysis using a second order Lagrangian polynomial interpolation ($p = 2$), in order to take advantage of the high-order accuracy offered by the DG method. As a next step, the simulation of a charring ablator was performed; the task was to test the new routine for the computation of pyrolysis, using the Navier-Stokes solver. Data of TACOT were used while, for the elemental composition of pyrolysis gases, the one estimated from literature was adopted. Considering the stiffness in the numerical solution due to pyrolysis, a shorter analysis was conducted. A total time of 1 second was indeed simulated, which is enough large to study the thermal decomposition but not the material recession. A list of 11 chemical species was considered, after a preliminary analysis in NASA CEA and the evolution of their mass fraction along the stagnation line was well captured. An interesting result was obtained in terms of stagnation point temperature: an unexpected decrease in temperature related to a strong gas blowing occurred at the first steps. Considering the fast dynamics of this initial transient, it could be unlikely to detect the same phenomenon experimentally, therefore further investigations are necessary. A final comparison between the ablation of TACOT and the carbon preform was proposed. As expected, the non-charring ablator achieved higher temperatures. The larger cooling effect of TACOT is partly attributable to pyrolysis, but the different properties of the two materials make not possible to study the effect of the thermal decomposition separately. A last important result concerns the elemental composition of pyrolysis gases. The simulation of TACOT was indeed replicated using a trial value for the elemental composition of pyrolysis gases and the comparison highlighted a difference in the stagnation point temperature of about 150 K. This proved that, although the routine implemented provided a reasonable method to compute the pyrolysis production rate, the elemental composition of pyrolysis gases still represents an unknown and thus it should be carefully assessed in order to get plausible results. Moreover, as a further improvement, the Argo analysis should be conducted using the multicomponent model for mass diffusion. Instead, a constant Schmidt number was set because of convergence issues related to the fast diffusion of some chemical species. Hence, longer times should be investigated, in order to study the material recession in the presence of pyrolysis too. In the light of this, even though Argo is not ready to simulate cork-based ablators yet, the new implementation represents one more step towards better simulations of charring ablators.

The second objective concerned the development of a physical model capable of treating swelling materials. Taking as a reference the mass conservation equation for the solid phase present in Argo, a one dimensional model was devised, based on a 1D nonlinear convection equation and assuming a proper swelling velocity profile derived from physical insights. The equation was solved in a variable U, treated as an average solid density under the hypothesis of a constant intrinsic density, as assumed in Argo. Great attention was reserved to ensure the mass conservation and the governing equation was also combined with the 1D heat equation, in order to take into account the effect of thermal gradients in the swelling phenomenon. Finally, the decomposition state of the material was considered too for the purpose of changing the velocity distribution along the material depending on the temperature evolution. However, it is worth pointing out the simplified assumptions of the model. The hypothesis of one dimensional flow was necessary due to the lack of experimental evidences about swelling along the other directions, but the thermal expansion actually could imply an anisotropic response. Another simplification consisted in neglecting the convective term in the heat equation, in order to decouple it from the convection equation. Moreover, the heat equation was solved for the pure virgin material, as if its properties did not change during heating. Finally, a last digression is provided in the following about the generic variable U. The equivalent equation implemented within Argo is indeed written in terms of solid volume fraction, ϵ_s:

$$\langle \rho_s \rangle = \epsilon_s \langle \rho_s \rangle_s$$

where $\langle \rho_s \rangle$ is the average density, while $\langle \rho_s \rangle_s$ is the intrinsic density. The idea is to extend the model currently used in *DGAblation* to describe pyrolysis, in order to include the swelling phenomenon. The current approach assumes that, during pyrolysis, the intrinsic density $\langle \rho_s \rangle_s$ remains constant. Hence, the solid equation is solved in terms of ϵ_s.

$$\langle \rho_s \rangle_s \epsilon_s \big|_{t_1} \xrightarrow{\dot{\omega}^{\text{pyro}}} \langle \rho_s \rangle_s \epsilon_s \big|_{t_2} \qquad \Longrightarrow \qquad \epsilon_s \big|_{t_1} \xrightarrow{\dot{\omega}^{\text{pyro}}} \epsilon_s \big|_{t_2} \tag{5.20}$$

where t_1 and t_2 are different evaluation times. In terms of porosity:

$$\epsilon_g = 1 - \epsilon_s \tag{5.21}$$

$$\epsilon_g \big|_{t_1} \xrightarrow{\dot{\omega}^{\text{pyro}}} \epsilon_g \big|_{t_2} \tag{5.22}$$

In the current approach, porosity ϵ_g increases inside the porous medium, because of pyrolysis. Even though the physical mechanism is different, the swelling phenomenon is expected to further enhance this effect, due to the thermal expansion of the gases trapped within the material. For the purpose of simplifying the implementation of the two mechanisms, two different levels of porosity could be defined: a *macroporosity* $\epsilon_{g,M}$ describing the gaseous phase inside the macropores of the material (as currently done in ARGO), and a new *microporosity* $\epsilon_{g,m}$ accounting for the void fraction in which the gases are trapped. Therefore, equation (5.21) can be rewritten as:

$$\epsilon_{g,M} = 1 - \epsilon_s \qquad \Longrightarrow \qquad \epsilon_{g,M} = 1 - (\epsilon_{s,m} + \epsilon_{g,m}) \tag{5.23}$$

where $\epsilon_s = \epsilon_{s,m} + \epsilon_{g,m}$. For the sake of clarity, two different representations are introduced.

A first representation

Although the cork P50 has a heterogeneous solid phase made up of cork and phenolic resin, this is not so relevant for this digression, so the reader is invited to consider a homogeneous phase, as sketched in Figure 5.59. When the material is heated, the temperature of

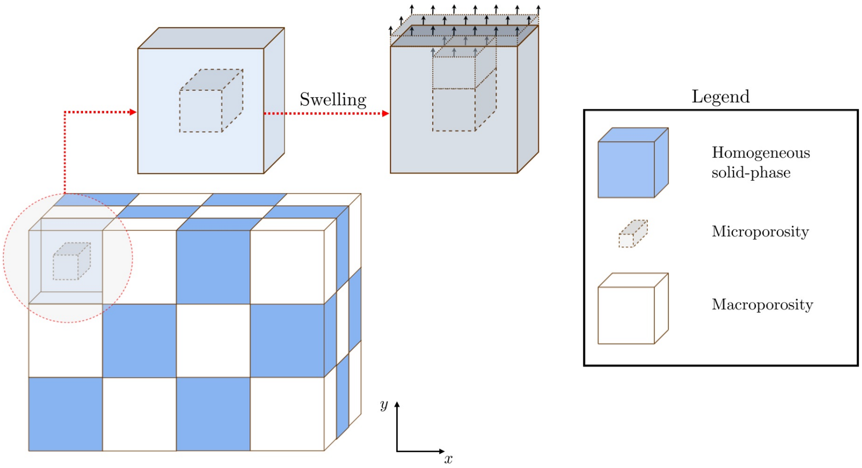

Figure 5.59: A first representation for a better understanding of the swelling phenomenon.

the gaseous phase increases, so that the material response is governed by two physical phenomena: the blowing of gases coming from the macropores, which actually are the only gases free to percolate towards the boundary layer, and the volume increase of the gases in the micropores. In fact, since the micropores are surrounded by solid material, they cannot exchange mass; as a result, the trapped gases can only increase their volume and exercise a pressure against the elastic walls of the solid phase, so that it is forced to swell. Moreover, one can assume this increase in volume to be an isobaric process; in this way, knowing in each computational element the initial micropores volume V_1, temperature T_1 and pressure P (and eventually the new gaseous mass produced by pyrolysis), after the computation of the new temperature T_2, the *ideal gas law* can be used to compute the increased micropores volume V_2 (Figure 5.60). Considering a section of the representation

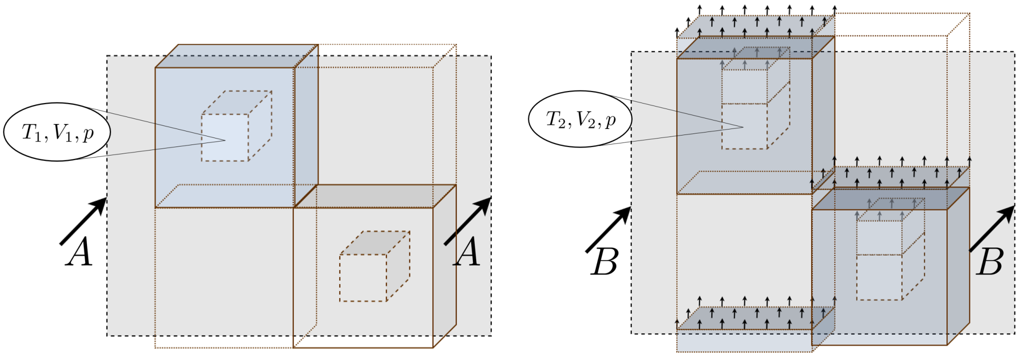

Figure 5.60: Sketch of the *local* behaviour before (left) and after (right) the thermal expansion.

given in Figure 5.60, the global material response is schematized in Figure 5.61. A simplified assumption could be to consider the volume increase of the micropores equal to the one of the solid phase, so that the intrinsic density $\langle\rho_s\rangle_s$ remains constant in time and it locally changes only in space, spreading the solid mass on a bigger volume. As a consequence, the solid mass is moved around by the swelling micropores, but it globally decreases only because of pyrolysis. The thermal expansion of the material can thus be modeled as the effect of a displacement imposed by the expansion of the gases trapped inside the micropores. Such a model requires a new way to describe the variation in average solid density:

$$\Big(\langle\rho_s\rangle_s \epsilon_s\Big)\Big|_{t_1} \xrightarrow{\dot{\omega}^{\mathrm{pyro}},\ \Delta V^{\mathrm{swell}}} \Big(\langle\rho_s\rangle_s \epsilon_s\Big)\Big|_{t_2} \tag{5.24}$$

A new average solid density should be defined:

$$\langle\rho_s\rangle = \overline{\langle\rho_s\rangle}_s \epsilon_s \tag{5.25}$$

where $\overline{\langle\rho_s\rangle}_s$ is an *averaged* intrinsic density, given by:

$$\overline{\langle\rho_s\rangle}_s = \frac{\int_{V_{s,m}} \rho_{s,m}\ \mathrm{d}V_{s,m} + \int_{V_{g,m}} \rho_{g,m}\ \mathrm{d}V_{g,m}}{\mathrm{d}V_{s,m} + \mathrm{d}V_{g,m}} \tag{5.26}$$

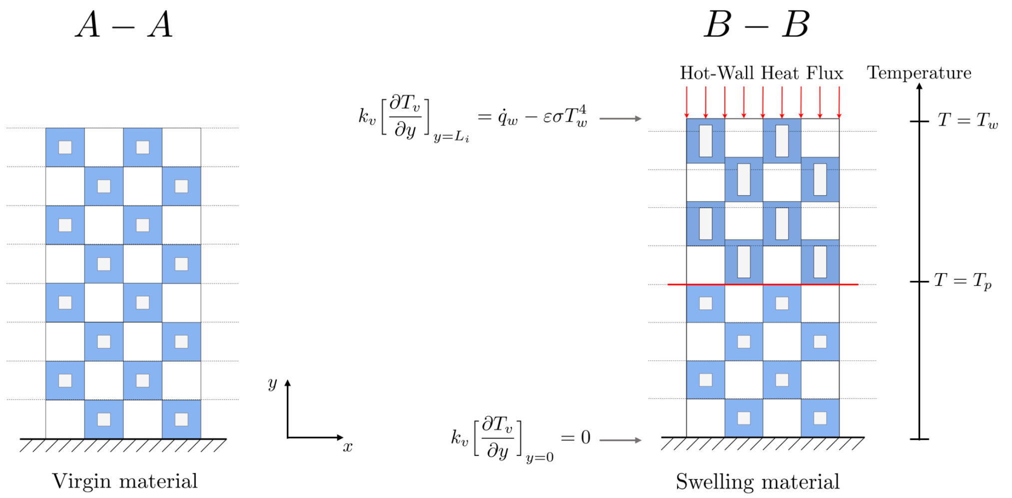

Figure 5.61: Sketch of the *global* material response before (left) and after (right) the thermal expansion. Focusing on the zone involved by swelling, the volume increase of the micropores (white region) could produce, as a simplification, an equal volume increase of the solid phase (blue region).

It is indeed obtained as the ratio between an average solid mass and an average solid volume, including a contribution related to the solid phase and another one associated to the micropores within the solid. It is also worth noting that:

$$\langle \rho_s \rangle_s = \frac{1}{\mathrm{d}V_{s,m}} \int_{V_{s,m}} \rho_{s,m} \, \mathrm{d}V_{s,m} \tag{5.27}$$

is the intrinsic density as it is currently defined in *DGAblation* and treated as a constant. Instead, the solid volume fraction could be now defined as:

$$\epsilon_s = \frac{\mathrm{d}V_{s,m} + \mathrm{d}V_{g,m}}{\mathrm{d}V_{s,m} + \mathrm{d}V_{g,m} + \mathrm{d}V_{g,M}} \tag{5.28}$$

where the denominator is the total volume, that has to include the contribution of macropores too. The expression for macroporosity comes as a result:

$$\epsilon_s = 1 - \frac{\mathrm{d}V_{s,m} + \mathrm{d}V_{g,m}}{\mathrm{d}V_{s,m} + \mathrm{d}V_{g,m} + \mathrm{d}V_{g,M}} = \frac{\mathrm{d}V_{g,M}}{\mathrm{d}V_{s,m} + \mathrm{d}V_{g,m} + \mathrm{d}V_{g,M}} \tag{5.29}$$

Finally, the new definition for the average solid density would be:

$$\langle \rho_s \rangle = \overline{\langle \rho_s \rangle}_s \epsilon_s = \frac{\int_{V_{s,m}} \rho_{s,m} \, \mathrm{d}V_{s,m} + \int_{V_{g,m}} \rho_{g,m} \, \mathrm{d}V_{g,m}}{\mathrm{d}V_{s,m} + dV_{g,m}} \cdot \frac{\mathrm{d}V_{s,m} + \mathrm{d}V_{g,m}}{\mathrm{d}V_{s,m} + \mathrm{d}V_{g,m} + \mathrm{d}V_{g,M}} \tag{5.30}$$

The mechanisms of swelling and pyrolysis thus affect $\mathrm{d}V_{g,m}$ and $\mathrm{d}V_{g,M}$ respectively. In fact, $\mathrm{d}V_{g,m}$ would change because of the isobaric expansion of the gases trapped within the micropores, whilst $\mathrm{d}V_{g,M}$ would not be directly affected by swelling, but it would change because of gas production due to pyrolysis.

This first representation was intended to better understand the connection between the physical phenomena and how to locally treat them within the model. For implementation purposes, a second representation was conceived, in order to make easier the future derivation of the final governing equation.

A second representation

For the sake of simplicity, the swelling material can be considered as a 1D bar and discretized in a certain number of elements, as sketched in Figure 5.62. The black arrows indicate that the displacement induced by the thermal expansion increases in proximity to the heat source. Considering a single element, a Lagrangian formulation could be used to compute the thermal expansion of a moving control volume. The base of each element would move under the push of the element below, so that they would be constrained if an unique direction is assumed for the displacement; in this case, the bottom of each element and the top of the element below would move at the same velocity:

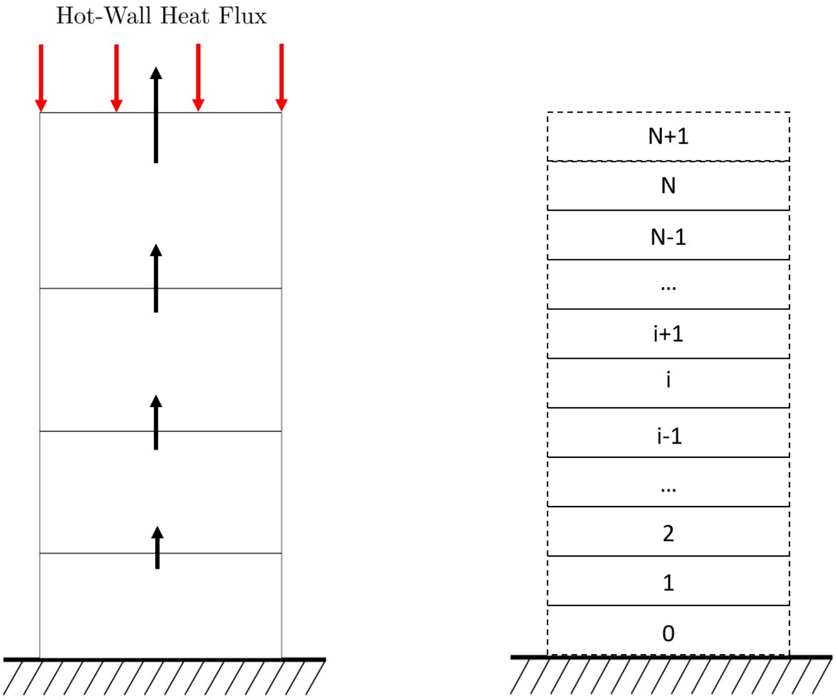

Figure 5.62: Swelling sample treated as a 1D bar and discretized in $N+1$ intervals.

$$v_{A',1} = v_{A',0} \tag{5.31}$$

Instead, the top velocity $v_{B',1}$ or, in other words, the local swelling velocity, would change governed by the thermal expansion. In particular, following the scheme in Figure 5.63, it

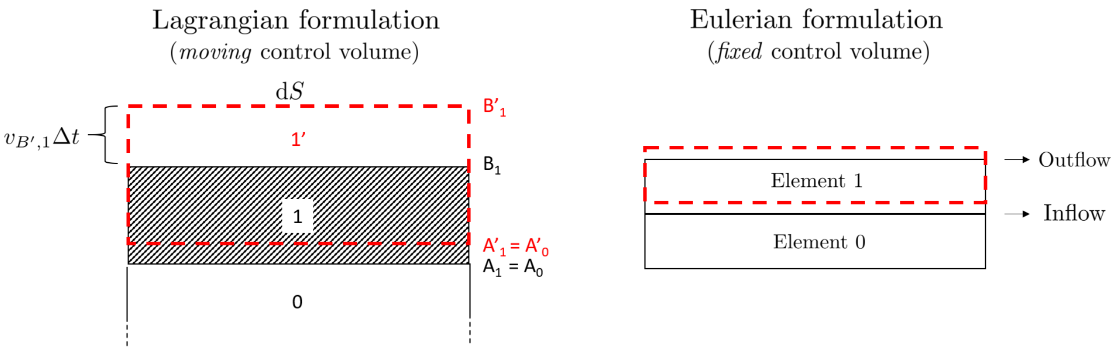

Figure 5.63: Lagrangian and Eulerian formulations for the reconstruction of the swelling velocity profile.

is given by:

$$v_{B',1} = \frac{\mathrm{d}V}{\mathrm{d}S\ \Delta t} \tag{5.32}$$

where $\mathrm{d}V$ is the change in volume computable by means of the ideal gas law, as explained above. Therefore, an Eulerian formulation could be used to compute the fluxes at the interfaces of each element and this would allow the reconstruction of the swelling velocity profile $\mathbf{u}$ directly from the distribution of the local $v_{B',i}$. Hence, the final mass conservation equation for the solid phase would be given by:

$$\frac{\partial}{\partial t}(\epsilon_s \overline{\langle \rho_s \rangle}_s) + \nabla \cdot \langle \rho_s \mathbf{u}_s \rangle = -\langle \dot{\omega}^{\mathrm{pyro}} \rangle \tag{5.33}$$

Naturally, the additional source term related to the heterogeneous reactions could be included in equation (5.33) too.

In conclusion, despite its simplifications, the physical model developed, tested in Matlab and presented in this work revealed promising results and offered a better understanding of the swelling phenomenon, opening the way towards further developments. Furthermore, the final digression represents the meeting point with Argo. However, considering that this still is a premature stage, an intermediate step could consist in its implementation within Echion. This is a one dimensional material response code developed at Cenaero to get familiar with the DG method [11] and its architecture is similar to Argo. If this approach proves to be an effective solution in Echion, confirming what was already highlighted by the Matlab code, it could be extended and implemented within Argo, for the purpose of getting a numerical tool capable of treating not only pyrolysis, but also the swelling behaviour of the new class of cork-based ablators. Finally, in the hope that the mission of Qarman will be successfully completed in August 2020, the precious data gathered during its atmospheric re-entry could be used for validation purposes, in order to ensure the accuracy of the future numerical analysis.

NASA CEA for chemical equilibrium analysis

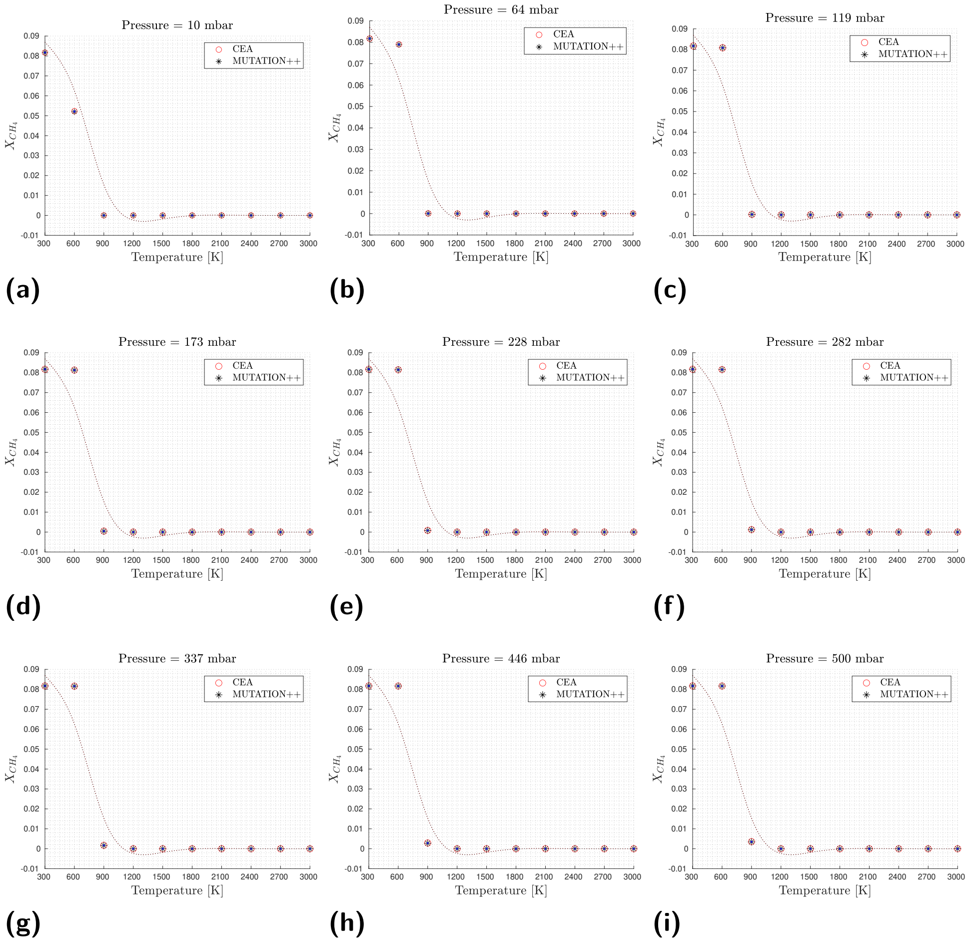

(a) **(b)** **(c)**

(d) **(e)** **(f)**

(g) **(h)** **(i)**

Figure 64: CH_4 mole fractions evolving with temperature and pressure.

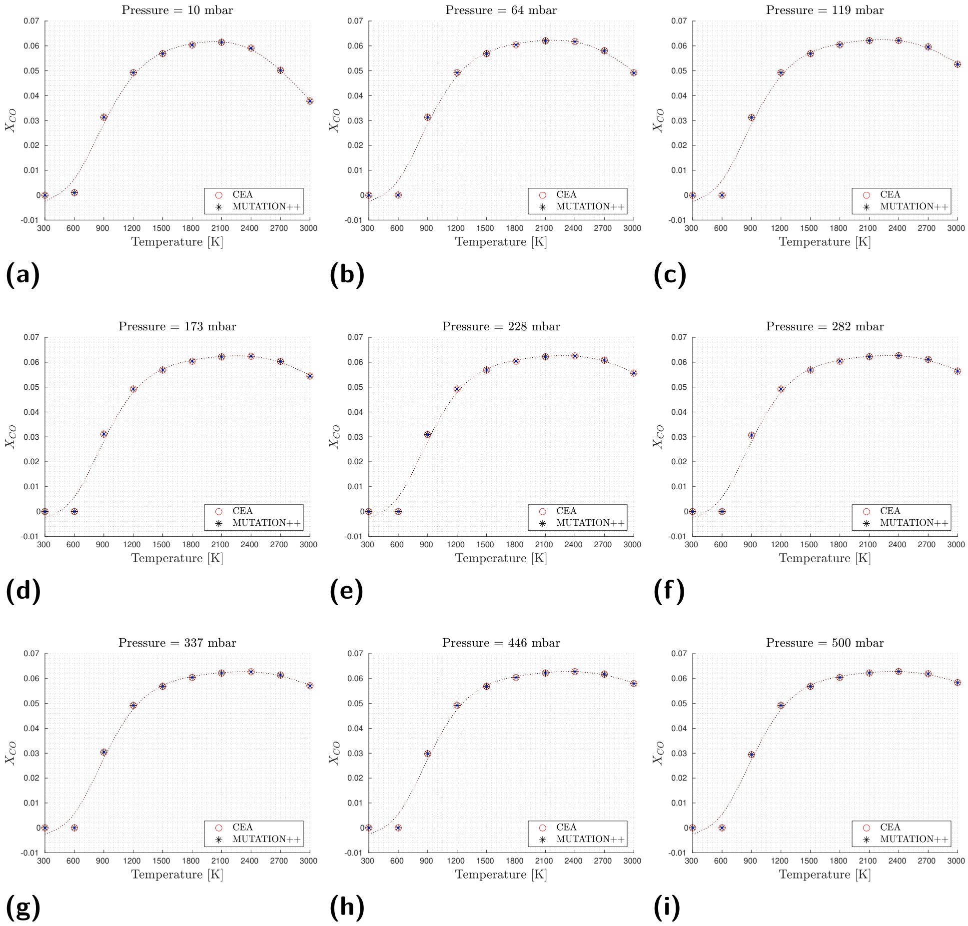

Figure 65: CO mole fractions evolving with temperature and pressure.

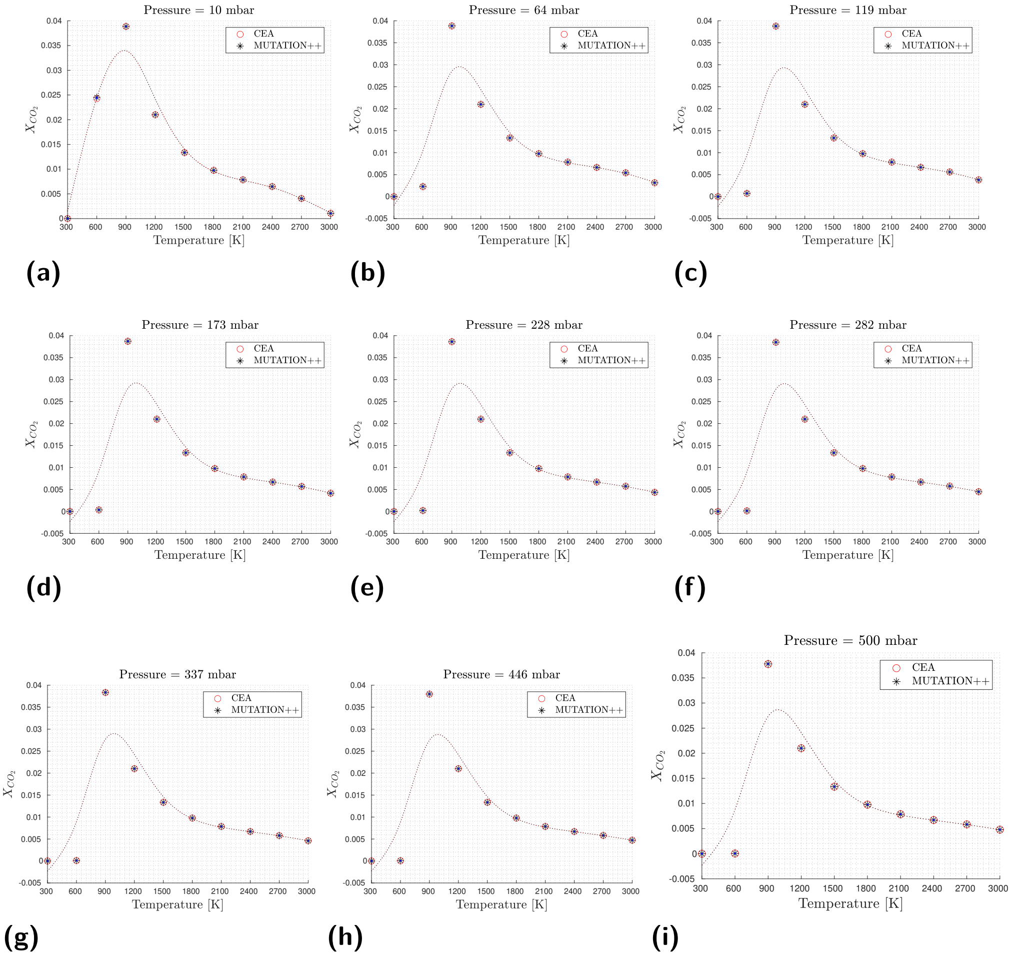

(a) **(b)** **(c)**

(d) **(e)** **(f)**

(g) **(h)** **(i)**

Figure 66: CO_2 mole fractions evolving with temperature and pressure.

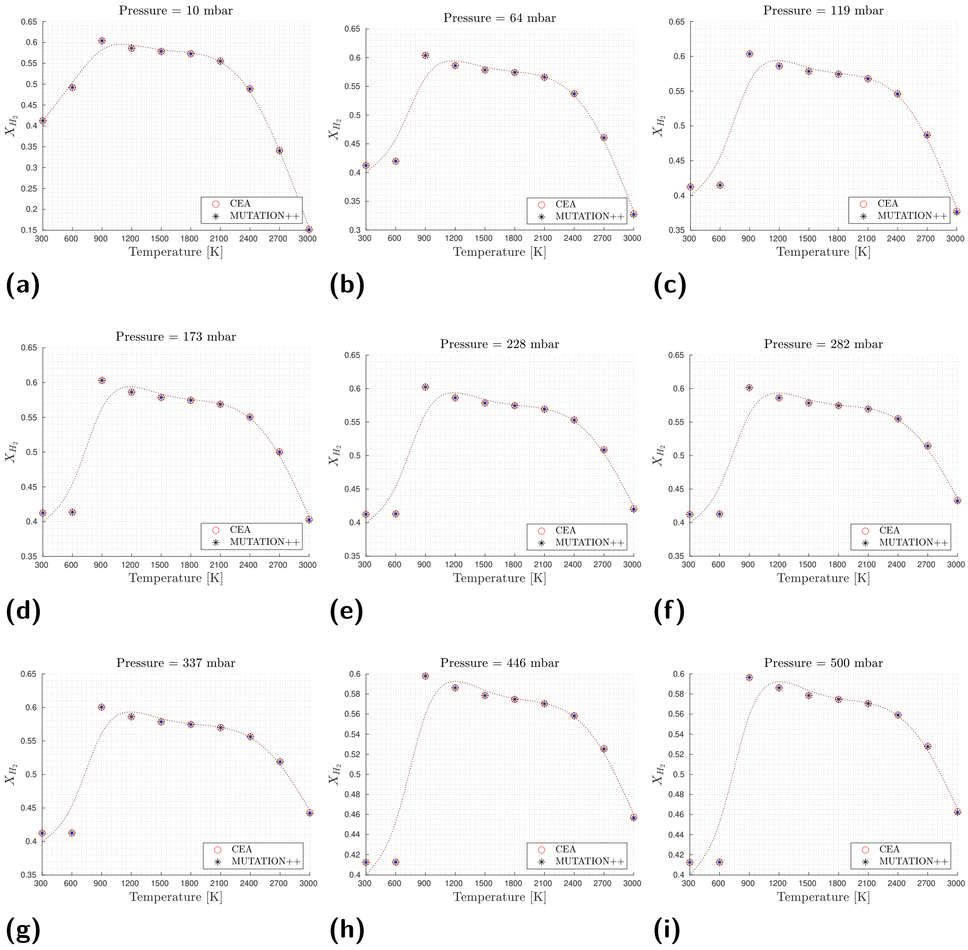

(a) **(b)** **(c)**

(d) **(e)** **(f)**

(g) **(h)** **(i)**

Figure 67: H_2 mole fractions evolving with temperature and pressure.

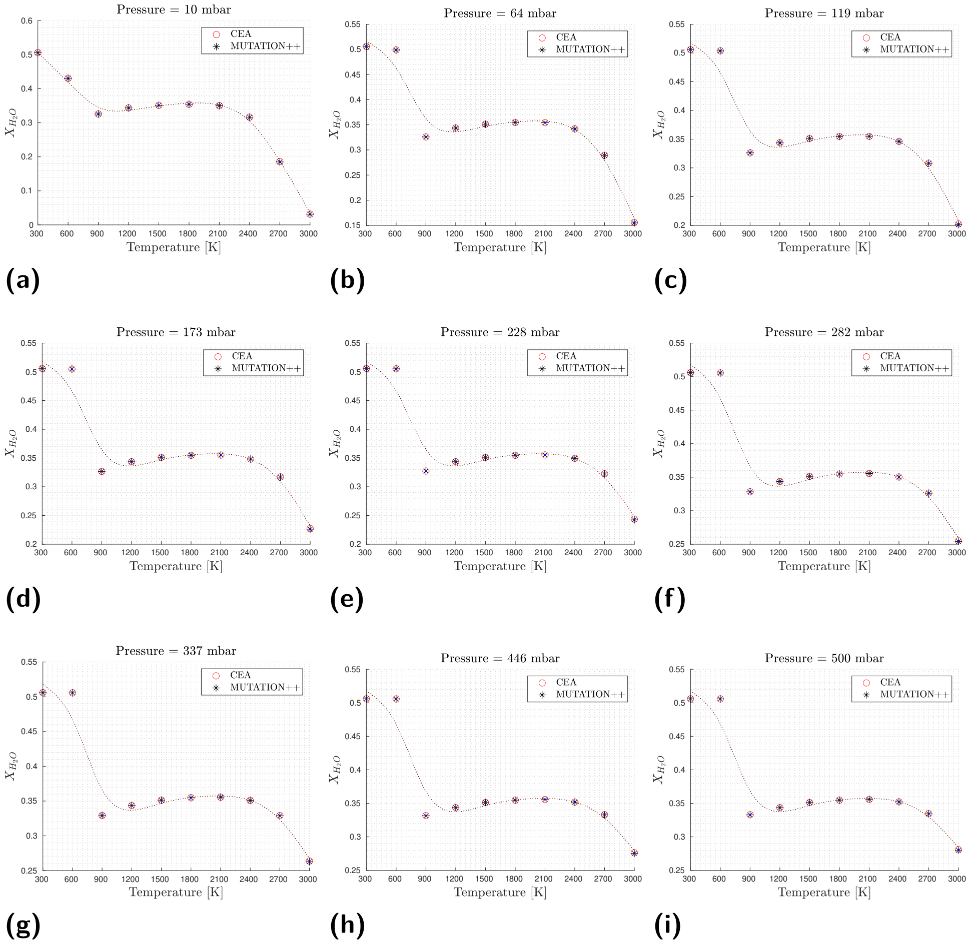

(a) **(b)** **(c)**

(d) **(e)** **(f)**

(g) **(h)** **(i)**

Figure 68: H_2O mole fractions evolving with temperature and pressure.

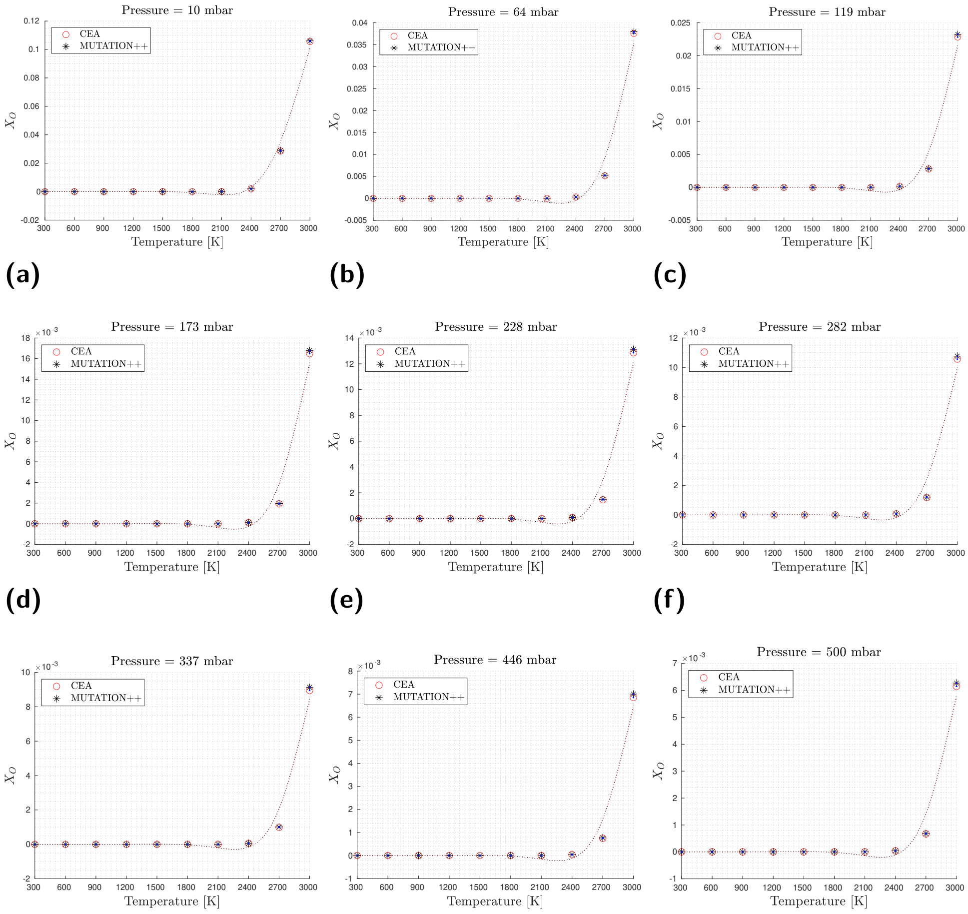

(a) **(b)** **(c)**

(d) **(e)** **(f)**

(g) **(h)** **(i)**

Figure 69: O mole fractions evolving with temperature and pressure.

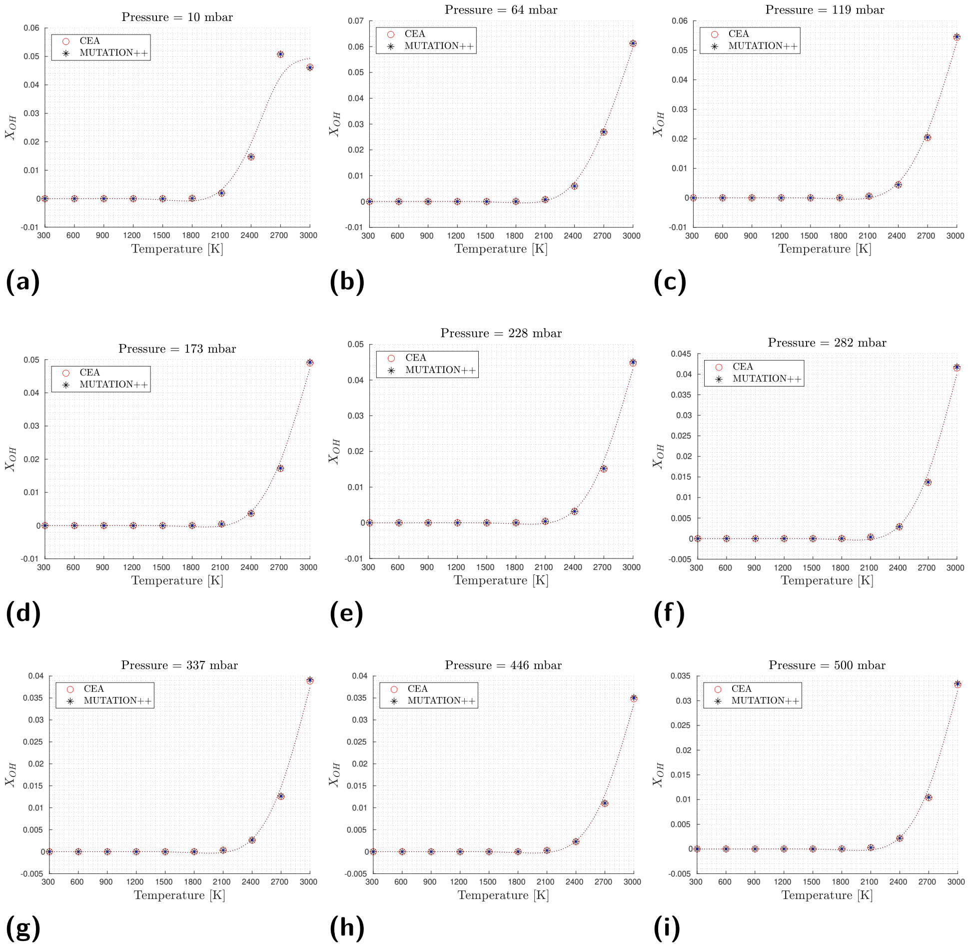

(a) **(b)** **(c)**

(d) **(e)** **(f)**

(g) **(h)** **(i)**

Figure 70: OH mole fractions evolving with temperature and pressure.

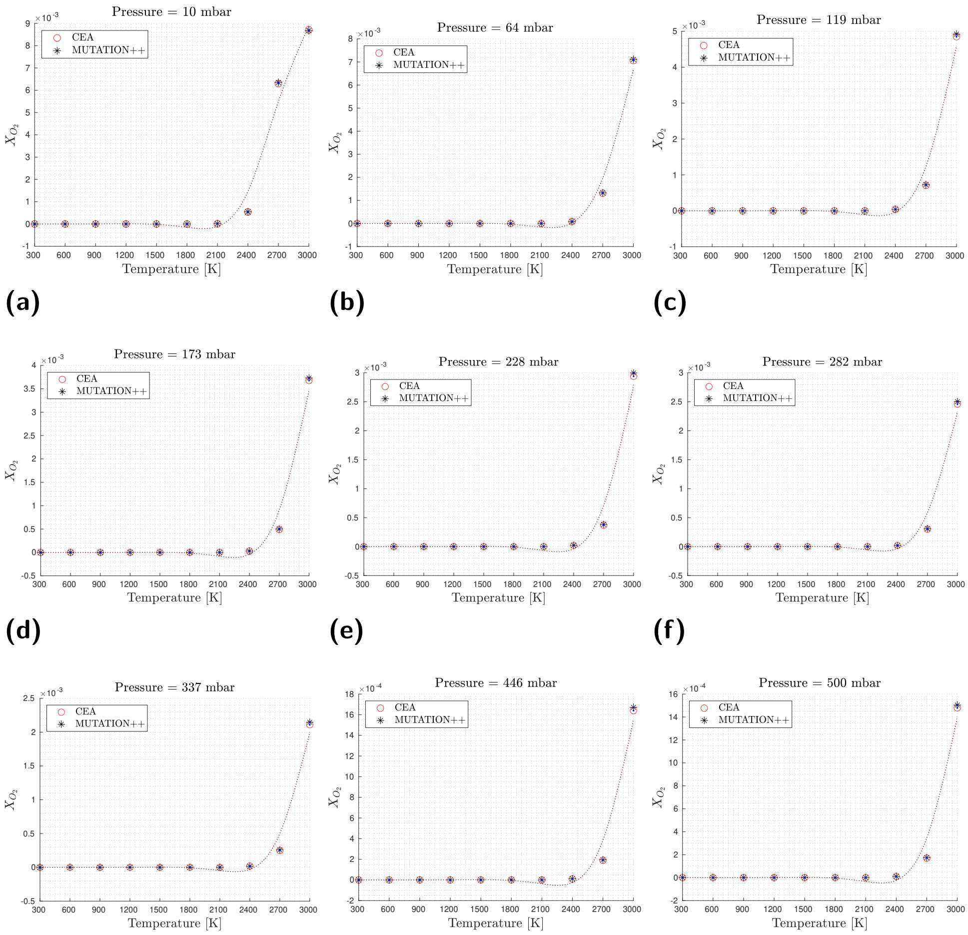

Pressure = 10 mbar

Pressure = 64 mbar

Pressure = 119 mbar

Pressure = 173 mbar

Pressure = 228 mbar

Pressure = 282 mbar

Pressure = 337 mbar

Pressure = 446 mbar

Pressure = 500 mbar

(a) **(b)** **(c)**

(d) **(e)** **(f)**

(g) **(h)** **(i)**

Figure 71: O_2 mole fractions evolving with temperature and pressure.

Bibliography

[1] Anderson, J. D., Jr, *Hypersonic and High-Temperature Gas Dynamics*, Second edition, AIAA Education Series, 2006, ISBN 1-56347-780-7.

[2] D'Ambrosio, D., Re-entry Aerothermodynamics lectures. Aerospace Engineering Master Course notes, Politecnico di Torino, Italy, 2019.

[3] Bird, G. A., *Molecular Gas Dynamics and the Direct Simulation of Gas Flows*, Second edition, Oxford Engineering Science Series, Oxford University Press, 1994.

[4] Sarma, G.S.R, Relevance of Aerothermochemistry for Hypersonic Technology, *Molecular Physics and Hypersonic Flows*, 1996, Vol. 482, ISBN 978-94-010-6604-4.

[5] Special Course on Aerothermodynamics of Hypersonic Vehicles, *AGARD Report No. 761.* Course held in Rhode-Saint-Genèse, Belgium, 30 May - 3 June 1988, sponsored by AGARD and the von Karman Institute for Fluid Dynamics.

[6] Bertin, J. , Jr, *Hypersonic Aerothermodynamics*, Third edition, AIAA Education Series, 1994, ISBN 978-1-56347-036-3.

[7] Sakraker, I., Aerothermodynamics of Pre-flight and In-flight Testing Methodologies for Atmospheric Entry Probes, Ph.D. thesis, Université De Liège & von Karman Institute for Fluid Dynamics, Belgium, Belgium, 2016.

[8] Tauper, M. E., A Review of High-speed, Convective, Heat-transfer Computation Methods, *NASA Technical Report 2914*, Ames Research Center, 1989.

[9] Gnoffo, P.A., Planetary-Entry Gas Dynamics, *Annual Review of Fluid Mechanics*, Vol. 31, pp. 459-494, 1999.

[10] Baals, D. D. and Corliss, W. R., Wind Tunnels of NASA, *NASA Technical Report SP-440*, NASA Headquarters, Washington, DC, United States, 1981.

[11] Schrooyen, P., Numerical Simulation of Aerothermal Flows Through Ablative Thermal Protection Systems, Ph.D. thesis, Université Catholique de Louvain & von Karman Institute for Fluid Dynamics, Belgium, Belgium, 2015.

[12] Wright, M. and Dec, J., Aerothermodynamic and Thermal Protection System Aspects of Entry System Design Course, *Thermal and Fluids Analysis Workshop*, NASA Short Course notes, 2012.

[13] Coheur, J., Turchi, A., Schrooyen, P. and Magin, T., Development of a unified model for flow-material interaction applied to porous charring ablators, *47th AIAA Thermophysics Conference*, June 5–9, 2017.

[14] Amorim Cork Composites, *Amorim Ablative Materials for the Space Industry*, 2008. Available: `https://www.amorimasia.com/uploads/4/8/0/0/48004771/tps_pp_04_07_2008ac.pdf`

[15] Scoggins, J.B., Bellas-Chatzigeorgis, G. and Dias, B., *MUTATION++ training presentation*, von Karman Institute for Fluid Dynamics, 2018.

[16] Swann, R. T., Pittman, C. M. and Smith, J. C., One-dimensional Numerical Analysis of the Transient Response of Thermal Protection Systems, *NASA Technical Note D-2976*, NASA Langley Research Center, Washington, DC, United States, September 1965.

[17] Rabinovitch, J., Marx, V.M. and Blanquart, G., Pyrolysis Gas Composition for a Phenolic Impregnated Carbon Ablator Heatshield, *11th AIAA/ASME Joint Thermophysics and Heat Transfer Conference*, June 16-20, 2014.

[18] Rindal, R. A., An Analysis of the Coupled Chemically Reacting Boundary Layer and Charring Ablator, Part VI: An Approach for Characterizing Charring Ablator Response With In-Depth Coking Reactions, *NASA Contractor Report 1065*, NASA, June 1968.

[19] Lachaud, J., Cozmuta, I. and Mansour, N., Multiscale Approach to Ablation Modeling of Phenolic Impregnated Carbon Ablators, *Journal of Spacecraft and Rockets*, Vol. 47, pp. 910-921, September, 2010.

[20] Başkaya, A.O., CFD Analysis of Qarman TPS in SCIROCCO conditions, Short Training Program Report, von Karman Institute for Fluid Dynamics, Belgium, 2017.

[21] Masutti, D., Trifoni, E., Umit, E., Martucci, A., Denis, A., Purpura, C., Scholz, T., Ceglia, G., Testani, P., Sakraker, I., Van der Haegen, V. and Chazot, O., QARMAN re-entry CubeSat: Preliminary Results of SCIROCCO Plasma Wind Tunnel Testing, *Small Satellites: An Emerging Paradigm for Bold Planetary Exploration*, Short Course, June 10, 2018.

[22] Kendall, R. M., Bartlett, E. P., Rindal, R. A. and Moyer, C. B., An Analysis of the Coupled Chemically Reacting Boundary Layer and Charring Ablator, Part I: Summary Report, *NASA Contractor Report 1060*, NASA, June 1968.

[23] Moyer, C. B. and Rindal, R. A., An Analysis of the Coupled Chemically Reacting Boundary Layer and Charring Ablator, Part II: Finite Difference Solution for the In-Depth Response of Charring Materials Considering Surface Chemical and Energy Balances, *NASA Contractor Report 1061*, NASA, June 1968.

[24] Bartlett, E. P. and Kendall, R. M., An Analysis of the Coupled Chemically Reacting Boundary Layer and Charring Ablator, Part III: Nonsimilar Solution of the Multicomponent Laminar Boundary Layer by an Integral Matrix Method, *NASA Contractor Report 1062*, NASA, June 1968.

[25] Bartlett, E. P., Kendall, R. M. and Rindal, R. A., An Analysis of the Coupled Chemically Reacting Boundary Layer and Charring Ablator, Part IV: A Unified Approximation for Mixture Transport Properties for Multicomponent Boundary-Layer Applications, *NASA Contractor Report 1063*, NASA, June 1968.

[26] Kendall, R. M., An Analysis of the Coupled Chemically Reacting Boundary Layer and Charring Ablator, Part V: A General Approach to the Thermochemical Solution of Mixed Equilibrium-Nonequilibrium, Homogeneous or Heterogeneous Systems, *NASA Contractor Report 1064*, NASA, June 1968.

[27] Clark, R. K., An Analysis of a Charring Ablator With Thermal Nonequilibrium, Chemical Kinetics, and Mass Transfer. *NASA Technical Note D-7180*, NASA, Hampton, VA, USA, June 1973.

[28] Chen, Y. K. and Milos, F. S., Ablation and Thermal Response Program for Spacecraft Heatshield Analysis, *Journal of Spacecraft and Rockets*, Vol. 36, No. 3, 1999, pp. 475–483.

[29] Chen, Y. K. and Milos, F. S., Multidimensional Effects on Heatshield Thermal Response for the Orion Crew Module, *39th AIAA Thermophysics Conference*, AIAA Paper 2007-4397, June 2007.

[30] Chen, Y. K. and Milos, F. S., Effect of Non-Equilibrium Chemistry and Darcy–Forchheimer Flow of Pyrolysis Gas for a Charring Ablator, *Journal of Spacecraft and Rockets*, Vol. 50, No. 2, 2013, pp. 256–269.

[31] Milos, F. S. and Chen, Y. K., Ablation, Thermal Response, and Chemistry Program for Analysis of Thermal Protection Systems, *Journal of Spacecraft and Rockets*, Vol. 50, No. 1, 2013, pp. 137–149.

[32] Chen, Y. K. and Milos, F. S., Two-Dimensional Implicit Thermal Response and Ablation Program for Charring Materials, *Journal of Spacecraft and Rockets*, Vol. 38, No. 4, 2001, pp. 473–481.

[33] Milos, F. S., and Chen, Y. K., Two-Dimensional Ablation, Thermal Response and Sizing Program for Charring Ablators, *Journal of Spacecraft and Rockets*, Vol. 46, No. 6, 2009, pp. 1089–1099.

[34] Chen, Y. K. and Milos, F. S.,Three-Dimensional Ablation and Thermal Response Simulation System, *38th AIAA Thermophysics Conference*, AIAA Paper 2005-5064, June 2005.

[35] Chen, Y. K., Milos, F. S. and Göçen, T., Validation of a Three-Dimensional Ablation and Thermal Response Simulation Code, *10th AIAA/ASME Joint Thermophysics and Heat Transfer Conference*, AIAA Paper 2010-4645, June–July 2010.

[36] Chen, Y. K. and Milos, F. S., Multidimensional Finite Volume Fully Implicit Ablation and Thermal Response Code, *Journal of Spacecraft and Rockets*, Vol. 55, No. 4, July–August 2018.

[37] Turchi, A., Helber, B., Munafò, A. and Magin, T. E., Development and Testing of an Ablation Model Based on Plasma Wind Tunnel Experiments, *11th AIAA/ASME Joint Thermophysics and Heat Transfer Conference*, June 16-20, 2014.

[38] Lachaud, J. and Mansour, N., Porous-Material Analysis Toolbox Based on OpenFOAM and Applications, *Journal of Thermophysics and Heat Transfer*, Vol. 28, No. 2, April-June, 2014.

[39] Johnston, C. O., Gnoffo, P. A. and Mazaheri, A., Study of Ablation–Flowfield Coupling Relevant to the Orion Heat Shield, *Journal of Thermophysics and Heat Transfer*, Vol. 26, No. 2, April–June, 2012.

[40] Nompelis, I. and Candler, G. V., A Parallel Implicit CFD Code for the Simulation of Ablating Re-Entry Vehicles, *47th AIAA Aerospace Sciences Meeting*, 5-8 January 2009, Orlando, Florida.

[41] Martin, A. and Boyd, I. D., Strongly Coupled Computation of Material Response and Nonequilibrium Flow for Hypersonic Ablation, *Journal of Spacecraft and Rockets*, Vol. 51, No. 1, 2015.

[42] Schrooyen, P., Hillewaert, K., Magin, T. E. and Chatelain, P., Fully implicit Discontinuous Galerkin solver to study surface and volume ablation competition in atmospheric entry flows, *International Journal of Heat and Mass Transfer*, Vol. 103, pp. 108-124, December 2016.

[43] Schrooyen, P., Coheur, J., Turchi, A., Hillewaert, K., Chatelain, P. and Magin, T., Numerical simulation of a non-charring ablator in high-enthalpy flows by means of a unified flow-material solver, *47th AIAA Thermophysics Conference*, June 5–9, 2017.

[44] Lachaud, J., Martin, A., Cozmuta, I., and Laub, B., Ablation Workshop Test Case #1, *4th AF-SNL-NASA Ablation Workshop*, March 1-3, 2011, Albuquerque, New Mexico.

[45] Lachaud, J., Martin, A., van Eekelen, T. and Cozmuta, I., Ablation Workshop Test Case #2, *5th Ablation Workshop*, April 10-11 2014, University of Illinois, Urbana-Champaign.

[46] van Eekelen, T., Lachaud, J., Martin, A. and Bianchi, D., Ablation Workshop Test Case #3, *6th Ablation Workshop*, March 1-3, 2011, Albuquerque, New Mexico.

[47] Martinez, J. H., Development of a Unified Computational Method for a Cork-Phenolic Material Applied to QARMAN's Heat Shield, Research Master Report, von Karman Institute for Fluid Dynamics, Belgium, 2018.

[48] Silva, S. P., Sabino, M. A., Fernandes, E. M., Correlo, V. M., Boesel, L. F. and Reis, R. L., Cork: properties, capabilities and applications, *International Materials Reviews*, Vol. 50, No. 6, 2005.

[49] Pereira, H., The thermochemical degradation of cork, *Wood Science Technology*, 26:259-269 (1992).

[50] Asma, C. O., Helber, B., Magin, T. E. and Chazot, O. P., Spectroscopy Measurements on Ablation Testing In High Enthalpy Plasma Flows, Final Technical Report, von Karman Institute for Fluid Dynamics, Belgium, October 27, 2010.

[51] Anderson, C. E., Jr., Dziuk, J., Jr., Mallow, W. A. and Buckmaster, J., Intumescent Reaction Mechanisms, *Journal of Fire Sciences*, Vol. 3, May-June 1985.

[52] Kuborn, X., Papalexandris, M. V. and Jeanmart, H., Modelling Transport Phenomena and Shrinkage during Wood Drying and Pyrolysis, *Third European Combustion Meeting*, 2007.

[53] Anderson, C. E., Jr. and Wauters, D. K., A Thermodynamic Heat Transfer Model for Intumescent Systems, *International Journal of Engineering Science*, Vol. 22, No. 7, pp. 881-889, 1984.

[54] Buckmaster, J., Anderson, C. and Nachman, A., A model for intumescent paint, *International Journal of Engineering Science*, Vol. 24, No. 3, pp. 263-276, 1986.

[55] Zhang, F., Zhang, J. and Wang, Y., Modeling study on the combustion of intumescent fire-retardant polypropylene, *eXPRESS Polymer Letters*, Vol.1, No.3, pp. 157–165, 2007.

[56] Poinsot, T. and D. Veynante. *Theoretical and numerical combustion*, Third Edition, R.T. Edwards Inc., 2011.

[57] Scoggins, J. B. and Magin, T. E., Development of Mutation++: MUlticomponent Thermodynamics And Transport properties for IONized gases library in C++, *11th AIAA/ASME Joint Thermophysics and Heat Transfer Conference*, American Institute of Aeronautics and Astronautics, June 16-20, 2014.

[58] S. Whitaker. *The method of volume averaging.* Kluwer Academic Publishers, Dordrecht, The Netherlands, 1999.

[59] Wang, L., Wang L., Guo, Z. and Mi, J., Volume-averaged macroscopic equation for fluid flow in moving porous media, *International Journal of Heat and Mass Transfer*, 82 (2015) 357–368.

[60] White, J. A., Borja, R. I. and Fredrich, J. T., Calculating the effective permeability of sandstone with multiscale lattice Boltzmann/finite element simulations, *Acta Geotechnica*, Vol. 1, pp. 195-209, 2006.

[61] Lachaud, J., van Eekelen, T., Scoggins, J.B., Magin, T.E. and Mansour, N.N., Detailed chemical equilibrium model for porous ablative materials, *International Journal of Heat and Mass Transfer* , Vol. 90, pp. 1034–1045, 2015.

[62] Li, T., Lyu, G., Saeed, H., Liu, Y., Wu, Y., Yang, G., and Lucia, L., Analytical pyrolysis characteristics of enzymatic/mild acidolysis lignin (EMAL), *BioResources*, 13(2), 4484-4496, 2018.

[63] Hillewaert, K., *Development of the discontinuous Galerkin method for large scale/high-resolution CFD and acoustics in industrial geometries.* PhD thesis, Université catholique de Louvain, 2013.

[64] Bhatia, A., Roy, S. and Gosse, R., Pyrolysis gas flow in thermally ablating media using time implicit discontinuous Galerkin methods, *49th AIAA Aerospace Sciences Meeting*, 4-7 January 2011, Orlando, Florida.

[65] Shima, E. and Kitamura, K., On New Simple Low-Dissipation Scheme of AUSM-Family for All Speeds, *47th AIAA Aerospace Sciences Meeting*, 5-8 January 2009, Orlando, Florida.

[66] Quarteroni, A., *Numerical Models for Differential Problems*, Third edition, Springer, 2017, ISBN 978-3-319-49315-2.

[67] D'Ambrosio, D., Computational Fluid Dynamics lectures. Aerospace Engineering Master Course notes, Politecnico di Torino, Italy, 2018-2019.

[68] Ferziger, J.H. and Peric, M., *Computational Methods for Fluid Dynamics*, Third edition, Springer, 2002, ISBN 3-540-42074-6.

[69] Anderson, J.D., Jr, *Computational Fluid Dynamics: The Basics with Applications.* McGraw-Hill Series, ISBN-0-07-113210-4, 1995.

[70] Park, C., Jaffe, R.L. and Partridge, H., Chemical-Kinetic Parameters of Hyperbolic Earth Entry, *Journal of Thermophysics and Heat Transfer*, Vol. 15, No. 1, January - March, 2001.

[71] Duffa, G., *Ablative Thermal Protection Systems Modeling*, AIAA Education Series, 2013, ISBN 978-1-62410-171-7.

[72] Dal Bianco, A., D'Ambrosio, D. and Mareschi, V., A Fully Implicit Material Response Code With Ablation and Pyrolysis For Simulation of Thermal Protection Systems, *8th European Symposium on Aerothermodynamics for Space Vehicles*, 2-5 March 2015.